Fall 12-16-2023

VOLUMETRIC IMAGING USING THE PUPIL-MATCHED REMOTE FOCUSING TECHNIQUE IN LIGHT-SHEET MICROSCOPY

Sayed Hassan Dibaji Foroushani

Sayed Hassan Dibaji Foroushani

Candidate

Physics and Astronomy

Department

This dissertation is approved, and it is acceptable in quality and form for publication:

Approved by the Dissertation Committee:

Tonmoy Chakraborty , Chairperson

Keith Lidke

Diane S Lidke

Sheng Liu

VOLUMETRIC IMAGING USING THE PUPIL-MATCHED REMOTE FOCUSING TECHNIQUE IN LIGHT-SHEET MICROSCOPY

BY

SAYED HASSAN DIBAJI FOROUSHANI

M.Sc., Optical Science and Engineering,

University of New Mexico, 2021

DISSERTATION

Submitted in Partial Fulfillment of the
Requirements for the Degree of

Doctor of Philosophy

Optical Science and Engineering

The University of New Mexico
Albuquerque, New Mexico

December, 2023

DEDICATION

To my beloved father, Shahab Dibaji, whose memory, and legacy inspire every step I take;

to my mother, Marzieh Dibaji, for her endless love and resilience;

and to my siblings, Babak, Ali, and Shima (Iran Alsadat) Dibaji, for being my pillars of strength and encouragement.

ACKNOWLEDGMENTS

First and foremost, I would like to express my deepest gratitude to my advisor, Dr.Tonmoy Chakraborty, for their unwavering support, guidance, and mentorship throughout this journey. Your expertise and insights have been invaluable, and your encouragement has driven my perseverance.

I am also immensely thankful to my dissertation committee members, Prof.Keith Lidke, Prof.Diane S Lidke, Dr.Sheng Liu, and Prof.Mansoor Sheik Bahae for their invaluable feedback, constructive criticisms, and continuous encouragement. Your collective wisdom has shaped this work in countless ways.

I also would like to thank the Cancer Research Facility Center (CRF) at the University of New Mexico for providing biological samples. I am also grateful to Rachel Grattan and Shayna Lucero for preparing samples and providing feedback to us.

Special thanks to my colleagues and friends in the Department of Physics and Astronomy for the stimulating discussions, and late-night brainstorming sessions, and for always being there academically and personally.

I would like to acknowledge the financial support from the Department of Physics and Astronomy, without which this research would not have been possible.

To my family, especially my mom and siblings, thank you for your unwavering love, patience, and belief in me. Your sacrifices and support have been my anchor, and this achievement is as much yours as it is mine.

Lastly, to all those who have been a part of this journey, directly or indirectly, I am eternally grateful. This dissertation stands as a testament to the collective effort and belief of many.

VOLUMETRIC IMAGING USING THE PUPIL-MATCHED REMOTE FOCUSING TECHNIQUE IN LIGHT-SHEET MICROSCOPY

By

Sayed Hassan Dibaji Foroushani

M.Sc., Optical Science and Engineering, University of New Mexico, 2021
Ph.D., Optical Science and Engineering, University of New Mexico, 2023

ABSTRACT

The dissertation explores innovative techniques in light sheet microscopy, a pivotal tool in biomedical imaging, to enhance its speed, resolution, and efficiency in capturing dynamic biological processes. Light sheet microscopy allows for quick 3D imaging of biological specimens ranging from cells to organs with high spatiotemporal resolution, large field-of-view, and minimal damage, making it vital for in vivo imaging.

The first project introduces a novel optical concept designed to optimize Axially Swept Light Sheet Microscopy (ASLM). This technique is crucial for imaging specimens ranging from live cells to chemically cleared organs due to its versatility across different immersion media. The project presents an innovative approach that enhances the performance of ASLM-based microscopes by scanning two staggered light sheets while synchronizing the rolling shutter of a scientific camera. This method allows ASLMs to image twice as fast without compromising the detection signal, providing a gentler illumination scheme and improving the imaging speed and detection signal of ASLM-based microscopes. The demonstrated technique is validated through imaging experiments on fluorescent beads and a chemically cleared mouse brain, showcasing its potential in advancing the field of light sheet microscopy.

The second project focuses on axial de-scanning using remote focusing in the detection arm of light-sheet microscopy. This technique is essential for high-speed, high-resolution volumetric imaging without disturbing the biological sample. The project introduces a unique optical design that can descan the axial focus movement in the detection arm of a microscope by overcoming the challenges associated with the polarization of emitted fluorescence. This technique allows for aberration-free, multi-color, volumetric imaging without compromising the fluorescent signal. It is demonstrated by acquiring fast dual-color 4D image stacks, highlighting its potential applications in various microscopy techniques that require adjustable Z-stages for volumetric imaging, such as confocal, 2-photon, and other light sheet variants.

TABLE OF CONTENTS

LIST OF FIGURES

detection arm of the light sheet microscope. In this configuration, objective lenses 1 and 2 are pupil-matched through two lenses to form a perfect imaging system. Combined with mirror M3 and a polarizing beam splitter (PBS), the whole system works as a remote focusing system. The novel design of this remote-focusing system is implementation in the detection arm for unpolarized fluorescent light emitted from the sample. To do this, two tilted mirrors M1 and M2 are utilized to direct both S and P-polarized beams toward Objective lens 2 and then combine the reflected beams from mirror M3 to create an image by S and P-polarized beams onto the camera by focusing through the tube lens. The mirror M3 is attached to the linear focus actuator (LFA), moving back and forth to scan the sample in the *Z*-direction to acquire a 3D image. In the illumination arm, the generated light sheet by a cylindrical lens is translated by a galvanometric scan mirror (GSM) along the detection arm. To focus the detection path on the plane of the light sheet, the synchronization of GSM and LFA is carried out by sawtooth signals. Simultaneous dual-channel imaging of the cell is achieved in 40 µm×150 µm FOV over 70 µm in the *Z*-direction. c) The polarization state of the incoming beams changes after reflection from mirror M3 (S to P, and P to S). d) The reflected beams from mirror M3 have a different polarization state compared to the incoming beams; therefore, they exist from a different side of the PBS than the incoming beams. e) The point spread function (PSF) of 200 nm beads formed by S, P, and S+P polarized beams. The microscope performs at the diffraction limit, 394 nm resolution, for S, P, and S+P in the lateral directions (*X*-*Y*), while it maintains a resolution of 654 nm in the axial direction (*Z*). ……107

CHAPTER 1: Principles, Techniques, and Challenges of Optical and Fluorescence Microscopy

1.1 Introduction

A light microscope is an optical system that creates a magnified image of an object through a combination of lenses. These lenses primarily include an objective lens that collects the sample's light and an eyepiece that focuses the light on the camera or human retina. These two lenses function as a 4f system where their different focal lengths create a magnified image of the object. The sample is illuminated by a condenser lens by focusing light on it. Then this light passes through the sample and is collected by the objective lens.

However, it’s crucial to acknowledge that not all light microscopes operate based on the principle of focusing light. For instance, some microscopes deploy widefield illumination techniques, casting a broad, unfocused light onto the sample to capture images.

Furthermore, while the description primarily refers to microscopes using transmitted light (light passing through the sample), some microscopes employ reflective or incident light techniques. In reflective light microscopy, the light does not pass through the sample; instead, it reflects off the sample's surface, providing valuable information about the sample’s exterior characteristics.

Samples are typically placed on a movable stage, allowing for detailed examination and navigation across different sections of the sample in the X-Y plane [1].

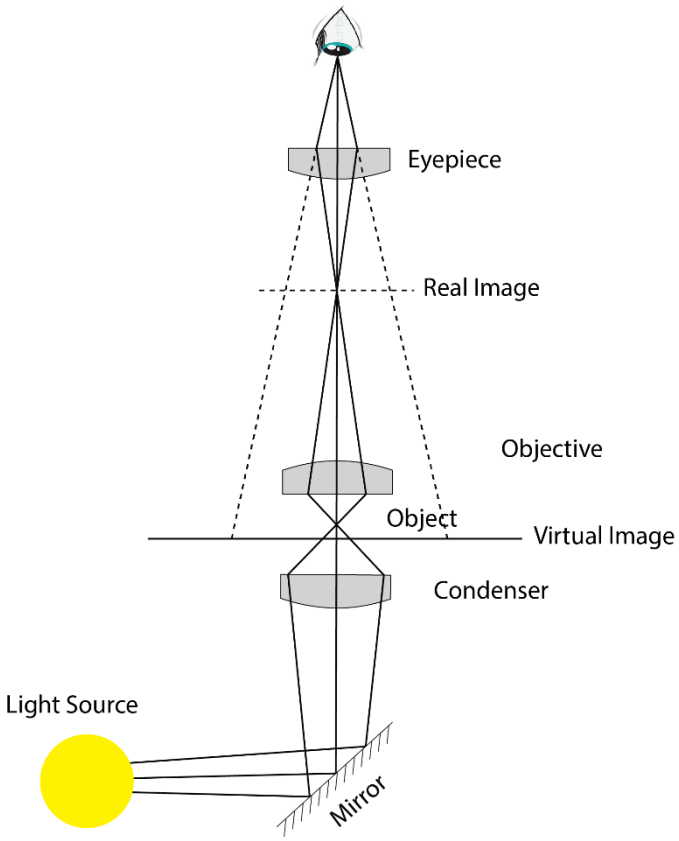

Figure 1.1. Light Microscope. The light from the source is directed onto the sample through the condenser lens, then reaches the lens system (objective and eyepiece) where it undergoes magnification. Redrawn from [1].

There are different types of light microscopes, such as phase contrast microscopes [2], fluorescence microscopes [3], brightfield microscopes [4], and polarized light microscopes [5], where each provide specific demands in fields like biology, medicine, material science, and physics.

1.2 Key Parameters in Microscopy Imaging

1.2.1 Field of View (FOV)

Field of view (FOV) is the area of the sample which is seen through the eyepiece or camera for a specific magnification. It is limited by the aperture stop of the system known as the field number (FN) and the magnification of the objective lens [6].

$$FOV = Field\ number / Objective\ Magnification \tag{1.1}$$

FOV is inversely proportional to the overall magnification of the system. A larger field of view allows for more data collection and thus a reduction of imaging time. The FN is usually shown on the eyepiece or objective lens and measured as the diameter in mm.

1.2.2 Numerical Aperture (NA)

The numerical aperture (NA) is defined as the light cone that the lens can capture from a light source[6].

$$NA = nsin(\alpha) \tag{1.2}$$

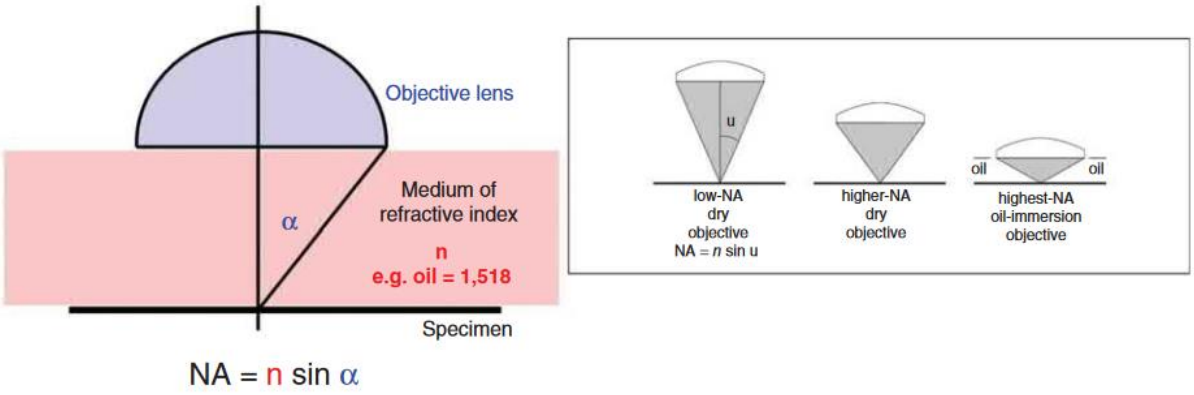

Figure 1.2. Understanding Numerical Aperture. The NA represents the ability of a lens to gather light and resolve fine specimen detail. By utilizing mediums with higher refractive indices, such as oil, one can effectively enhance the numerical aperture (NA), thereby improving the resolving power of the microscope [7].

where α is the semi-angle of the maximum light cone that can enter or leave the lens. The Numerical Aperture (NA) can be enhanced by the refractive index of the medium which in turn affects the resolution of a microscope. Therefore, certain objective lenses are designed to work in an oil medium that has a higher refractive index compared to air or water.

1.2.3 Microscopy Resolution

The resolution of the microscope is defined as the smallest distance between two-point sources which is discernible on the camera and largely depends on the diffraction limit of the objective lens [6]. When the light passes through the lens with a circular aperture it undergoes Fraunhofer diffraction, which is the Fourier transform of the aperture. This generates a pattern called an airy pattern which is a circular bright region in the center, an airy disk, surrounded by dark and bright fringes[6]. The intensity of the airy pattern can be mathematically expressed using the first order of the Bessel (J_1) function [6]

$$I(\theta) = I_0[2J_1(kasin\theta)/kasin\theta]^2 \quad (1.3)$$

Where zero determines the location of the dark fringes in the diffraction pattern. In this formula, I_0 is the peak intensity at the center of the Airy disc, θ is the angle from the optical axis, a is the radius of the aperture, and k is the wave number ($2\pi/\lambda$).

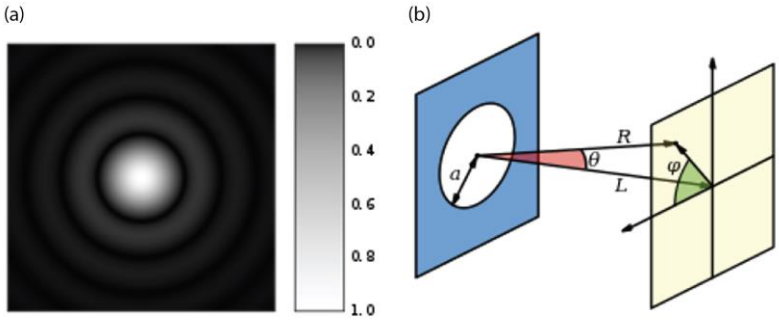

Figure 1.3. Airy disk. a) Airy disk pattern generated by the computer. b) In a far field limit the airy disk pattern is created by a circular aperture [8].

The size of the airy disk can determine the resolution of the microscope. The radius of the airy disc is calculated by the first zero of the Bessel function J_1 which is given by [6]

$$R = 0.61\,\lambda/\,NA \quad (1.4)$$

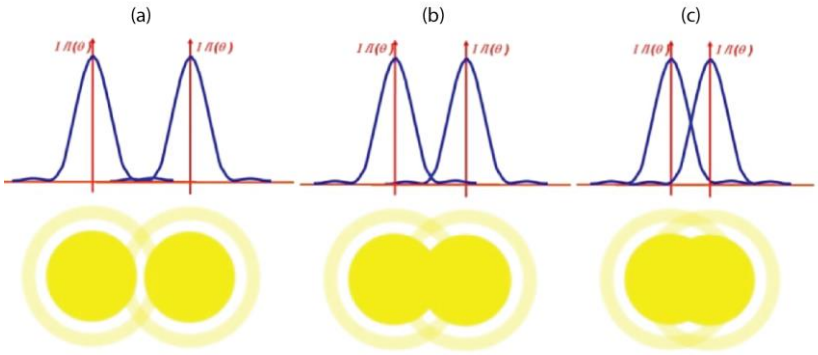

Figure 1.4. Rayleigh criterion. a) Two-point sources are clearly resolvable. b) Two-point sources are just resolvable c) Two-point sources are not resolvable [9].

The lateral resolution of the microscope is defined by the Rayleigh criterion. According to this criteria, two-point sources are discernible whenever the maximum airy pattern of one point source falls on the minimum of the other one [6]. It means that two-point sources are resolvable when they are one radius of an airy disk away. Thus, the lateral resolution of the microscope is given by

$$0.61\ \lambda / NA \tag{1.5}$$

The axial resolution of the lens is defined as the Rayleigh criterion along the confocal axial [10]

$$R_{ax} = 2\ n\lambda\ /\ NA^2 \tag{1.6}$$

In essence, by knowing the numerical aperture of the objective lens, the spatial resolution of the microscope can be calculated which is a fundamental concept to optimize and control the microscope.

To measure the resolution of a microscope, one typically uses fluorescent microspheres, or "beads," which are significantly smaller than the expected resolution limit of the microscope. A bead sample is usually prepared by embedding the beads into 2% agarose gel. The microscope then captures a series of images at different focal planes, forming a z-stack. Beads appearing as diffraction-limited spots (bright spots surrounded by dark rings) are isolated. Using image analysis software, the Full Width at Half Maximum (FWHM) of the intensity profile of beads is determined by the Gaussian profile curve fitting for each spot. This FWHM corresponds to the microscope's resolution. This method effectively measures the point spread function (PSF) of the microscope, quantifying both lateral (*X*-*Y* plane) and axial (*Z*-plane) resolution.

1.2.4 Depth of Field (DOF) and Depth of Focus

Depth of Field (DoF) and Depth of Focus are two important concepts in optics and microscopy that deal with the region in the sample and image space respectively in which the image looks sharp [6,11].

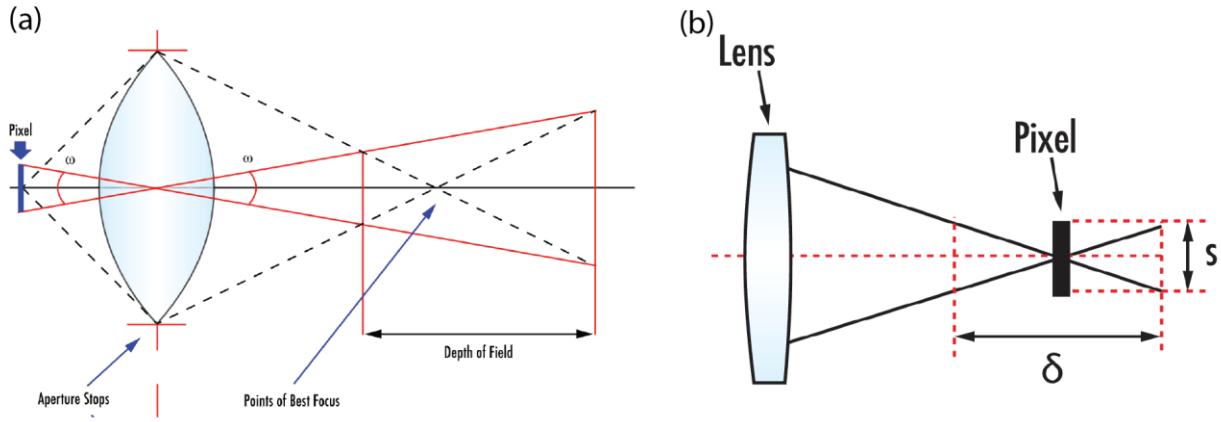

Figure 1.5. Depth of field and Depth of focus. a) Depth of field refers to the area within the object space where the image appears in focus and sharp. b) Depth of focus indicates the range within the image space where the image maintains its sharpness [11].

Depth of Field refers to the distance over which the specimen can be moved while still appearing in sharp focus. In other words, it's the thickness of the specimen that can be seen in focus at once [6,11]. The DoF is determined by several factors, including the lens aperture, the magnification, and the wavelength of light. Generally, a larger aperture (and thus a higher numerical aperture) will have a shallower depth of field [11]. This means that while one can see more detail due to the higher resolution, only a smaller section of the specimen in focus at a time can be seen.

Conversely, a smaller aperture has a larger DoF, allowing the observation of a larger thickness of the specimen in focus, but with less detail.

Depth of Focus, on the other hand, is a related concept that refers to the range over which the image plane (camera sensor) can be moved while maintaining acceptable sharpness in the image [6,11]. It is essentially the tolerance that the microscope's imaging sensor or the camera's film plane has for being out of perfect alignment with the plane of focus. The Depth of Focus is important for ensuring that the image is captured as clearly and sharply as possible. The depth of focus is generally much larger than the depth of field.

It's always a trade-off between the level of detail and the volume of the specimen that can be observed in focus at the same time. Understanding and manipulating these concepts are crucial in fields ranging from research to medical diagnostics to photography.

1.3 Optical Imaging Systems: Analysis and Improvement Techniques

1.3.1 The Compound Microscope

A compound microscope combines two lens systems, the objective and the eyepiece, to magnify objects. This configuration offers a significant advantage over simple, single-lens microscopes, allowing for magnifications up to 1400x as opposed to the maximum 275x achieved by simple microscopes. The primary function of the objective lens is to produce a primary image of the specimen, which is then further magnified by the eyepiece. The eyepiece essentially operates like

a magnifying glass, and in some instances, it can be inverted and used to inspect surfaces directly[12].

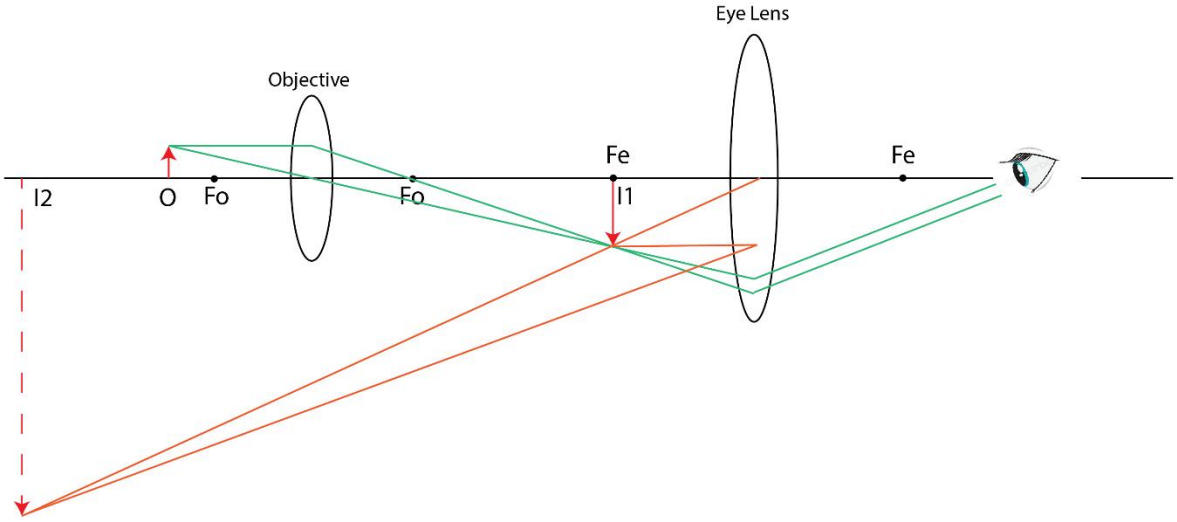

Figure 1.6. The compound microscope. In the compound microscope, the coordination of the objective, eyepiece, and human eye results in a combined image magnification superior to what can be achieved with a simple single-lens system. To elucidate the ray trajectory, let's represent the objective and eyepiece as individual thin lenses for the sake of streamlined ray tracing. The eyepiece's front focal plane aligns with the primary image plane (PIP) at the point where I1 appears. As rays emanate from the eyepiece in parallel, it's essential to utilize construction rays to pinpoint the location of the resultant virtual image, denoted as I2.Redrawn from [12].

Total magnification in a compound microscope is derived by multiplying the magnifications of the objective and the eyepiece[12].

$$M_{Total} = M_{obj}M_{eye} \tag{1.7}$$

In some advanced microscopes, there is an "infinity-corrected system". Here, the object is precisely positioned at the front focal plane of the objective. These systems project a primary image that is theoretically at infinity. The objective magnification in this system is determined by dividing the reference focal length by the focal length of the objective. Objectives in these systems

must be parfocal, ensuring they share a common focus point. The result is a powerful tool that efficiently illuminates specimens, provides improved resolution, and offers high magnifications that far exceed the capabilities of simple microscopes[12].

1.3.2 Linear Systems and Convolution in Optical Systems

The Point Spread Function (PSF) is an important concept in imaging systems, as it characterizes how a system responds to a point source of light. Essentially, the PSF describes how a single point of light is spread out in the image produced by the system.

A linear system adheres to the principle of superposition, meaning the response of the system to a sum of inputs is equal to the sum of the responses to each input considered separately. In the context of imaging, if the object being imaged can be thought of as a collection of point light sources, the image produced is simply the superposition of the PSFs corresponding to each of these point sources. It can be described mathematically as follows.

A system is 'linear' if it satisfies two fundamental properties: superposition and homogeneity.

1. Superposition: If input A produces output X and input B produces output Y, then input $A + B$ will produce output $X + Y$.
2. Homogeneity (or Scalability): If an input A produces an output X, then cA will produce cX, where c is any constant.

Mathematically, if $T(f1(t)) = g1(t)\ and\ T(f2(t)) = g2(t)$, a linear system will satisfy:

$$T(\alpha f1(t) + \beta f2(t)) = \alpha g1(t) + \beta g2(t) \quad (1.8)$$

where T is the system operator, and α and β are constants[13].

In an imaging system, let f represent a sample which is the summation of δ-function, each corresponding to a point source.

$$f(x_1, y_1) = \iint_{-\infty}^{+\infty} f(u,v)\delta(u - x_1, v - y_1)dudv \quad (1.9)$$

If g represent the image of the sample f and T is the operator of optical the system, then it is written as[14]:

$$g(x_2, y_2) = T\big(f(x_1, y_1)\big) \quad (1.10)$$

Where g is the output function of the operator T. Therefore,

$$g(x_2, y_2) = T\big(f(x_1, y_1)\big) = T\Big(\iint_{-\infty}^{+\infty} f(u,v)\delta(u - x_1, v - y_1)dudv\Big) \quad (1.11)$$

If the operator T is linear, the equation (1-11) can be written as[14]:

$$g(x_2, y_2) = \iint_{-\infty}^{+\infty} f(u,v)T(\delta(u - x_1, v - y_1))dudv \quad (1.12)$$

we define h function as:

$$h(u - x_2, y_2 - v) = T(\delta(\xi - x_1, \eta - y_1)) \quad (1.13)$$

where h is the output response at point (x_2, y_2) to the input function δ at point (x_1, y_1) . The h is called impulse response of system T.

$$g(x_2, y_2) = \iint_{-\infty}^{+\infty} f(u,v)h(u - x_2, y_2 - v)dudv \quad (1.14)$$

Here, $f(u, v)$ is the input field distribution and $h(u - x_2, y_2 - v)$ represents the system's impulse response[13]. Here, $h(u - x_2, y_2 - v)$ is the PSF of the optical system. Equation (1-14) clearly represent that the generated image is the superposition of the PSFs corresponding to each of these point sources. The convolution operation essentially expresses how every point in the input interacts with every point in the impulse response to produce the output.

1.3.3 Point Spread Function (PSF)

For a sensing system, such as microscopes, the impulse response function is also called a point spread function (PSF) which describes how the system responds to a point source of light. It essentially provides information about the spatial distribution of light from a point source as perceived by the microscope and recorded by the detector [15].

Due to the nature of light and the physics of imaging systems, a point source of light would not be imaged as another point. In real systems, a point source is spread out and forms a diffraction pattern - typically an Airy pattern in a system limited by diffraction. The specific pattern that is formed, known as the point spread function, is determined by the properties of the imaging system including its aperture, aberrations, and other factors[1] [15].

The PSF has significant implications in microscopy. It limits the resolution of the microscope because any two points closer together than the width of the PSF will be seen as blurred together,

[1] Wavelength of Light, Defocus, Depth of Field, Camera Pixel Size, Alignment, Optical Coatings, Motion Blur, Quality of the Lenses, and Mirrors

making it impossible to distinguish them as separate entities. This is the basis for the resolution limit defined by the Abbe diffraction criterion.

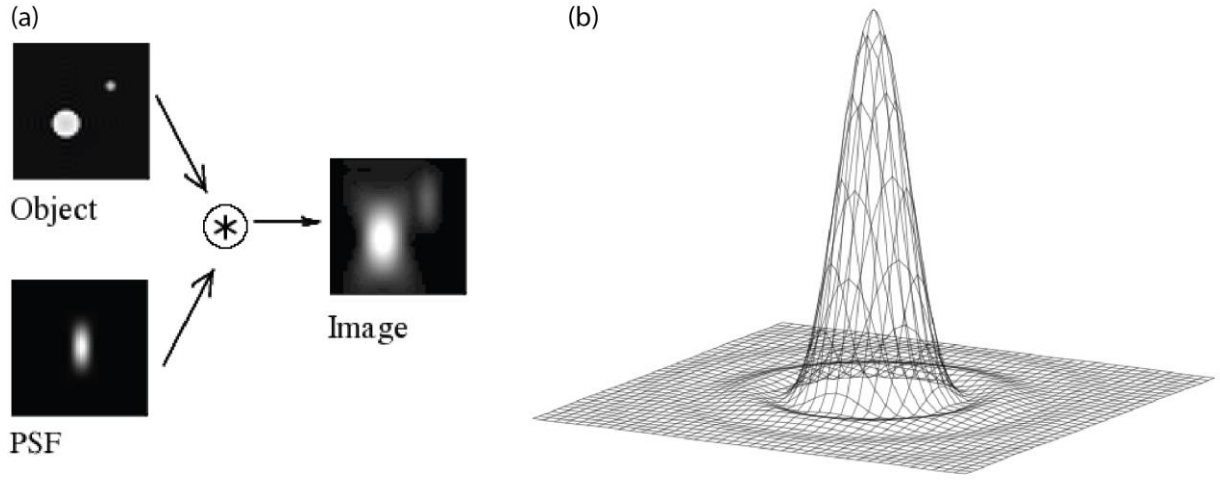

Figure 1.7. Image formation and PSF. a) Generated Image is the convolution of the real light source with the PSF. b) Airy disk formed by a circular aperture [16].

The PSF is often mathematically defined in terms of the impulse response of an imaging system. Let's consider an ideal imaging system in the context of linear systems theory. The image, $i(x, y)$, produced by such a system can be described as a convolution of the object being imaged, $o(x, y)$, and the system's point spread function, $h(x, y)$ [13,17]. This relationship is written as

$$i(x, y) = o(x, y) * h(x, y) \tag{1.15}$$

The asterisk ($*$) here represents the convolution operation, which, in two dimensions, is defined as

$$f(x, y) * g(x, y) = \int\int f(u, v)\, g(x - u, y - v)\, du\, dv \tag{1.16}$$

Applying this to our image formation equation

$$i(x, y) = \int\int o(u, v)\, h(x - u, y - v)\, du\, dv \tag{1.17}$$

Here, $h(x - u, y - v)$ describes how a point object at location (u, v) contributes to the pixel values at location (x, y) [13,17].

For an ideal imaging system limited only by diffraction (an "Airy disk"), the PSF is often modeled using the squared magnitude of the Fourier transform of the aperture function. In the case of a circular aperture, like the microscope, this takes the form of a Bessel function[13].

In real-world systems, the PSF can be more complex, potentially including distortions introduced by lens aberrations. In this case, the PSF can sometimes be measured empirically by imagining a point source and observing the resulting spread.

1.3.4 Image Restoration: Deconvolution Technique for Deblurring

Deconvolution is a computational process used in microscopy to improve the quality of images. It is used to reverse the optical distortion that takes place in a microscope or other imaging devices, due to the system's point spread function (PSF)[18].

When an image is captured with a microscope, the true object is convolved with the system's PSF. Convolution is a mathematical operation that essentially mixes the object and the PSF, leading to a blurred image. This blurred image is what one typically sees when looking through the microscope or capturing an image with a microscope camera[18].

In theory, by knowing the exact PSF of the microscope, one could "deconvolve" the captured image to recover the true object. Deconvolution is the process of "unmixing" the object and the

PSF. In practice, it is a complex process that requires robust algorithms and often quite a bit of computing power[18].

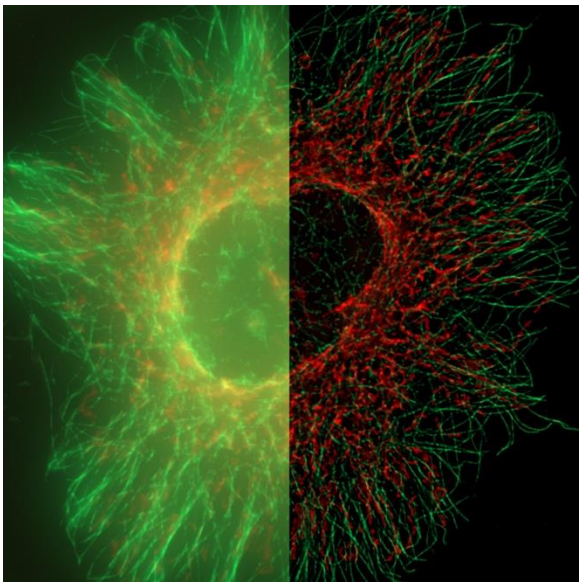

Figure 1.8. Deconvolution. U2OS cells were labeled for both mitochondria and microtubule structures using TOM20-mCherry and Tubulin-GFP, respectively, prior to and following the application of a Constrained Iterative Deconvolution [19].

Deconvolution works by using the PSF to make a mathematical model of how the microscope blurs the image. With this model, the deconvolution algorithm can then work backward to estimate what the object must have been to produce the observed image.

Mathematically, in the spatial domain, convolution is described by

$$i(x,y) = o(x,y) * h(x,y) \tag{1.18}$$

where: $i(x,y)$ is the observed image, $o(x,y)$ is the object (or true image), $h(x,y)$ is the point spread function (PSF), and $*$ represents the convolution operation[18].

Deconvolution aims to solve for $o(x, y)$, given $i(x, y)$ and $h(x, y)$. However, because the convolution operation loses information, the deconvolution problem is often ill-posed. In other words, there are multiple possible solutions.

In the frequency domain, convolution becomes multiplication[18].

$$I(u, v) = O(u, v) \times H(u, v) \tag{1.19}$$

Where $I(u, v)$ is the Fourier transform of the observed image, $O(u, v)$ is the Fourier transform of the object (or true image), and $H(u, v)$ is the Fourier transform of the point spread function (PSF).

In the frequency domain, simple deconvolution would theoretically be as simple as the division[18].

$$O(u, v) = I(u, v) \,/\, H(u, v) \tag{1.20}$$

However, due to the potential presence of noise in the observed image, along with the possibility of having zeros or near-zero values in the PSF and inaccuracies in the estimated PSF, simple division in the frequency domain often leads not only to noise amplification but also to significant artifacts, and instability in the reconstructed image.

To address these challenges, various regularized deconvolution methods, including Wiener filtering and Tikhonov regularization, have been proposed. These techniques introduce additional constraints to render the deconvolution problem more well-posed. In doing so, they mitigate the impact of noise, division by zero or near-zero values in the PSF, inaccuracies due to mismatched or estimated PSF, artifacts, and instability in the reconstruction process.

1.3.5 Signal-to-Noise Ratio

The signal-to-noise ratio (SNR) is an important aspect of fluorescence microscopy that directly impacts the quality of the generated images. SNR is a measure that compares the level of the desired signal to the level of background noise. The signal is the fluorescence emitted by the fluorophore while the noise refers to the unwanted signal, like the electronic noise of the detector.

Noise in microscopy images is a critical factor that can affect the interpretation and analysis of those images. Several types of noise can be present in microscopy, such as:

1. Shot Noise: Shot noise in microscopy images is also known as Poisson noise because the arrival of photons at a detector follows a Poisson distribution. It arises due to the quantized nature of light and the inherent randomness in the number of photons hitting each pixel of the detector. The level of shot noise is proportional to the square root of the number of photons detected[20].

2. Thermal Noise: Thermal noise, also known as dark current noise, results from the thermal excitation of electrons within the imaging sensor, which generates a small current even in the absence of light. This noise has a Gaussian distribution and increases with temperature. The variance (σ^2) of thermal noise for a given pixel is proportional to the exposure time and the sensor's temperature[21].

SNR can be calculated using the following formula

$$SNR = \frac{\mu}{\sigma} \tag{1.16}$$

Where μ is signal and σ is the noise. The SNR determines the ability of the microscope to distinguish the fluorescence signal from the background noise. A high SNR value indicates that

the signal is significantly higher than the noise, allowing the detection and visual representation of subtle changes and details in the specimen.

Several factors can influence the SNR in fluorescence microscopy. These include the brightness of the fluorophores, the illumination intensity, the exposure time, the optical alignment, and the sensitivity and specificity of the detectors. Proper optimization of these parameters can significantly improve the SNR, leading to clearer and more precise microscopic images. Moreover, the use of image processing techniques and advanced algorithms can also aid in improving the SNR post-acquisition, thereby enhancing the interpretability and reliability of microscopic data.

1.4 Understanding Light Dynamics and Challenges in Fluorescence Microscopy

1.4.1 Various Modes of light interaction in Microscopy and their applications

In microscopy, light can interact with the specimen in several ways, each providing different information about the sample under study. Here are six primary modes of interaction [22].

1. Absorption: This is the most basic interaction. Different materials in the specimen absorb different wavelengths of light, causing some light to be "lost". The contrasting absorption rates across the specimen enable detailed observations.
2. Reflection: Light can bounce off the surface of the specimen. This is common in metallurgical microscopy, where the light reflected off the surface of the metal sample provides details about its structure.

3. Refraction: When light passes from one medium to another (for instance, from glass to the sample), it changes speed, causing it to bend. This bending of light, or refraction, contributes to the formation of an image in the microscope.
4. Diffraction: When light encounters an obstacle or aperture near the size of its wavelength, it bends and interferes with itself, creating a diffraction pattern. Understanding this can be critical for revealing the details of the specimen's structure.
5. Fluorescence: Some specimens can absorb light at one wavelength and re-emit it at a longer wavelength. This is known as fluorescence and is used in fluorescence microscopy to observe biological specimens that are stained with fluorescent dyes.
6. Polarization: Certain materials can change the polarization state of light, which can provide information about the sample. Polarized light microscopy is used to study materials like crystals, minerals, and biological specimens that exhibit birefringence (double refraction).

Each of these interactions forms the basis of different types of microscopy techniques, and choosing the appropriate one depends on the nature of the specimen and the information required.

1.4.2 Fluorescence Principles

The principle of fluorescence involves the absorption of light at a specific wavelength by an atom or molecule (termed as a fluorophore), exciting it to a higher energy state. After a brief period,

the excited fluorophore then returns to its ground state by releasing the absorbed energy in the form of light at a longer wavelength. This emitted light as detected is a fluorescence [23,24].

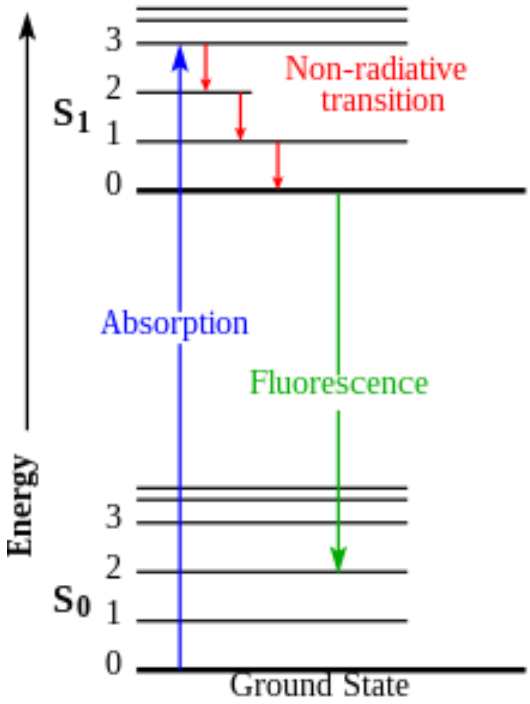

Figure 1.9. An illustration of the Jablonski Diagram. Visualizing the journey of an electron through excitation, relaxation, and various energy state transitions in a molecule upon interaction with a light [23].

This absorption of light energy prompts an electron within the fluorophore to jump from its ground state to an excited state, leaving a hole in the ground state. The electron in the excited state, however, is unstable and looks for ways to return to the ground state. This return usually happens through non-radiative processes where the energy is dissipated as heat. But in fluorescent materials, a portion of this energy is released as light, a process known as fluorescence [23,24].

The emitted light always has a longer wavelength (lower energy) than the absorbed light. This is due to a phenomenon known as the Stokes shift. The Stokes shift occurs because some energy is lost through non-radiative processes before fluorescence emission. The energy difference between the absorbed and emitted light is what makes fluorescence microscopy possible, as it allows the emitted light to be separated from the excitation light, ensuring that only fluorescence from the sample is detected [23,24].

The duration between the absorption and emission process is typically very short, on the order of nanoseconds [23,24]. However, manipulating with the properties of the fluorophores and the surrounding environment enables the creation of fluorophores with delayed fluorescence or even phosphorescence (where the emission can last for much longer times). This allows for more measurements and the investigation of different processes within the samples under study. Understanding the physics of fluorescence is therefore vital to harnessing its potential in microscopy and other applications.

1.4.3 Fluorescent Labeling

Fluorescent labels, also known as fluorophores, play an integral role in fluorescence microscopy. They are molecules that can absorb light at specific wavelengths and subsequently emit light at longer wavelengths due to the phenomenon of Stokes shift mentioned above. These labels allow the illumination of specific components of a sample to visualize them under a fluorescence microscope.

A vast array of fluorescent labels exists, each with its unique properties. These include organic dyes such as fluorescein and rhodamine, fluorescent proteins like green fluorescent protein (GFP), and quantum dots [25]. The choice of fluorophore is dictated by several factors, including its excitation and emission wavelengths, brightness, photostability, and the nature of the specimen to be labeled [25].

One of the critical aspects of fluorescent labels is their specificity. Many labels can be conjugated with antibodies or other molecules that bind to specific targets within a cell or tissue [25]. For instance, a fluorescent label can be attached to an antibody that binds to a specific protein of interest. When introduced into a sample, the antibody seeks out and binds to its target, bringing the fluorescent label along with it. Under the microscope, the sample is illuminated at the excitation wavelength of the label, and then the emitted fluorescence is observed, thereby revealing the location of the protein of interest. This ability to "light up" specific molecules or structures within complex samples is what makes fluorescence microscopy such a powerful tool in biology and medicine [25].

1.4.4 Photobleaching and phototoxicity

Photobleaching and phototoxicity are two important considerations when using fluorescence microscopy, particularly in live cell imaging.

Photobleaching refers to the phenomenon where fluorescent molecules lose their ability to fluoresce over time due to prolonged exposure to the excitation light source. This results in the gradual fading of the fluorescent signal, making long-term observations and measurements challenging [24]. Photobleaching is a result of irreversible photophysical damage to the fluorescent molecules, which essentially alters their structure and prevents them from undergoing the necessary transitions for the fluorescence [24]. Techniques such as reduced light exposure, the use of anti-fade reagents, and the development of more photostable fluorophores are implemented to combat photobleaching. Fluorescence photobleaching can be quantified as normalized mean intensity in N frames of stack images as follow

$$\bar{I}_{norm}^{(i)} = \frac{\bar{I}_{img}^{(i)} - \bar{I}_{bg}^{(i)}}{MAX\,(\bar{I}_{img}^{(i)} - \bar{I}_{bg}^{(i)})}, i \in [1, N] \quad (1.22)$$

Where i is the frame index, $\bar{I}_{img}^{(i)}$ and $\bar{I}_{bg}^{(i)}$ represent the mean intensity of the background of the selected region and entire field of view at the frame i respectively [26].

Phototoxicity, on the other hand, is a harmful effect that can occur in live cell imaging. The high-intensity light used to excite the fluorescent molecules can cause damage to the cells being observed, altering their behavior and viability [27]. This is particularly true when using short-wavelength light, such as ultraviolet, which can induce direct DNA damage and generate reactive oxygen species leading to oxidative stress [28]. Phototoxicity can severely compromise the physiological relevance of observations made during live-cell imaging.

Thus, managing these effects is critical to fluorescence microscopy, particularly when dealing with delicate samples like live cells. Careful selection of fluorophores, optimization of imaging

conditions, and mindful handling of illumination settings can mitigate these concerns and enhance the data quality obtained from fluorescence microscopy studies.

1.5 Summary

This chapter provided an expansive insight into the principles, techniques, and challenges inherent in optical and fluorescence microscopy. The intricate interplay between the key parameters, including Field of View (FOV), Numerical Aperture (NA), microscopy resolution, and depth of focus, is pivotal in acquiring accurate and detailed images of microscopic entities. Understanding these parameters allows for optimized data collection and imaging, thus reducing the time spent on microscopy while enhancing the quality of the generated images.

Fluorescence microscopy, with its reliance on the unique properties of fluorophores, illuminates the detailed internal structures of samples and offers invaluable insights into their composition and behavior. The careful selection and application of fluorescent labels, considering their excitation and emission wavelengths, brightness, and photostability, are crucial for successful imaging. Concurrently, researchers must navigate challenges such as photobleaching and phototoxicity, which can compromise the integrity and viability of live cell samples, necessitating the development and employment of advanced techniques and methodologies to mitigate these effects.

Furthermore, the concept of deconvolution unveils the path toward rectifying optical distortions in the acquired images, although it presents its set of challenges, including the requirement for

robust algorithms and substantial computational power. This alleviates some of these challenges, serving as testament to the ongoing advancements in the field aiming to enhance the quality and reliability of microscopic imaging.

In summation, the realm of optical and fluorescence microscopy is intricate and dynamic, demanding a deep understanding of its fundamental principles and an awareness of its inherent challenges. As technology advances, so does the field of microscopy, offering ever-improving tools and methodologies to explore and understand the microscopic world in unparalleled detail. The knowledge and concepts encapsulated in this chapter lay the groundwork for engaging with microscopy in a thoughtful and effective manner.

CHAPTER 2: Volumetric Imaging in Fluorescence Microscopy: Background and Challenges

2.1 Introduction

Fluorescence, the phenomenon of certain materials emitting light upon absorbing photons, was first documented in the early 19th century. Sir George Gabriel Stokes, a British scientist, was among the pioneers in studying fluorescence. He identified the blue glow from quinine as fluorescence in the 1850s and coined the term "fluorescence" inspired by the mineral fluorite, which glows with a similar blue light[29]. However, it wasn’t until the 20th century that this phenomenon was harnessed for microscopy. The idea of using fluorescence in microscopy was revolutionary. By the latter half of the 20th century, with the invention of the first epifluorescence microscope, scientists could now observe biological samples with unprecedented detail by harnessing the power of these glowing molecules[30]. As technology progressed, fluorescence microscopy evolved, incorporating digital imaging and advanced optics, becoming an indispensable tool in modern research labs.

At its core, a fluorescence microscope isn't drastically different from a light microscope; however, its specialized components make it unique. Lenses play a pivotal role in magnifying and focusing the emitted light from the sample. High-quality objective lenses, coupled with ocular or eyepiece lenses, facilitate observation of samples with clarity and precision[30].

Filters also serve to isolate the specific wavelength of light needed to excite the fluorescent molecules and, in turn, filter out unwanted wavelengths from the emitted light. This ensures that

only the desired fluorescent light is viewed or captured by imaging systems. Dichroic mirrors, a type of beam splitter, are used to reflect the excitation light onto the sample while allowing the longer-wavelength emitted light to pass through to the detector[30].

The light source, meanwhile, is the engine of the fluorescence microscope. Historically, xenon or mercury arc lamps were employed as the principal light sources. However, with technological advancement, LEDs and lasers have become popular due to their longevity, stability, and ability to produce intense, specific wavelengths of light. Lasers, especially, are crucial for advanced techniques like confocal microscopy, where pinpoint accuracy of light is required[30].

Together, these components – lenses, filters, and light sources – form the backbone of a fluorescence microscope, enable the visualization of the intricate dance of molecules within biological specimens.

Fluorescence microscopy enables 3D imaging of biological samples, providing unparalleled insights into cellular structures and processes. Traditional imaging largely presented two-dimensional snapshots of specimens, offering invaluable yet limited insights into their complexities. Think of these as flat photographs compared to volumetric imaging's detailed sculptures. Volumetric imaging goes beyond mere surfaces, diving deep into the 'volume' of specimens, capturing their essence in three dimensions—length, width, and depth. Such a comprehensive view, especially in biology, unveils the meticulous organization of cells within tissues, the sophisticated design of vascular networks, and the intricate dance of interconnected neurons.

2.2 Understanding Fluorescence Microscopy

Fluorescence microscopy capitalizes on a simple yet fascinating phenomenon where certain molecules absorb light (photons) of one wavelength (color) and then almost instantaneously re-emit light at a longer wavelength. The journey begins with 'excitation,' where these molecules are exposed to a specific wavelength of light. When this light is absorbed, the molecules are raised to a higher energy state. However, these excited states aren't stable, and the molecules are eager to return to their original, more comfortable state. As they 'relax' back to this ground state, they release the energy they absorbed in the form of emitted light. Importantly, the emitted light is of a longer wavelength than the excitation light, and it's this change or shift in light that is harnessed in fluorescence microscopy[24].

For instance, a molecule might absorb blue light and emit green light. The microscope's optical system is equipped by filters to separate these two types of light, ensuring that the observer or detector only sees the emitted green light and not the original blue excitation light. This offers a sharp contrast between the specimen and the background, allowing for detailed visualization of structures[24].

However, not all biological structures are naturally fluorescent. To make the invisible visible, molecules called fluorophores or fluorescent probes should be employed. Fluorophores are special because they can absorb and emit light, making them the stars of the fluorescence microscopy show. They can be thought of as tiny lightbulbs that turn on when hit with the right kind of light[24].

There are naturally fluorescent proteins, like the famous Green Fluorescent Protein (GFP) from jellyfish, which can be genetically introduced into organisms to make certain cells or structures glow. On the other hand, there are synthetic dyes developed specifically for their fluorescent properties, each with its unique excitation and emission profiles. Tagging biological specimens with these probes, whether by staining or genetic manipulation, will enable to target specific structures, organelles, or even molecular processes[25].

The art and science of fluorescence microscopy, therefore, lie in selecting the right fluorophore, illuminating it with the correct wavelength, and then capturing the glow it emits. The combination of these steps provides a vibrant, high-contrast, and often multi-colored view of the microscopic world, illuminating details that would otherwise remain hidden[24].

Fluorescence microscopy, like all scientific disciplines, stands on the shoulders of both its historical foundations and the relentless drive for innovation. Over the years, it has seen significant technological advances that have expanded its capabilities and applications. The primary challenges in fluorescence microscopy have been resolution, sensitivity, and speed, and technological advancements have been directed at improving these parameters.

One of the early major leaps was the development of confocal microscopy. By using pinhole optics to exclude out-of-focus light, confocal microscopes provide clearer images with improved z-resolution. This enabled the imaging of thicker samples and 3D reconstructions of biological structures[31].

Two-photon microscopy was another groundbreaking advancement. By utilizing two photons to excite a fluorophore simultaneously, this technique allows for deeper penetration into tissue

samples with reduced photodamage, proving invaluable benefits in neurobiology and other fields requiring in-depth imaging[32].

Further pushing the boundaries of resolution, super-resolution microscopy techniques emerged, like STORM (Stochastic Optical Reconstruction Microscopy) and PALM (Photo-Activated Localization Microscopy). These techniques surpassed the diffraction limit of light, which was once thought to be an insurmountable barrier in optical microscopy, offering resolutions even at the nanoscale[33].

Integrating digital technology has been another crucial advance. High-sensitivity cameras, computational techniques for image analysis, and powerful software platforms have turned the once purely observational tool into a quantitative one.

Fluorescence microscopy, with its vivid imagery, has revolutionized traditional microscopy by offering more than just color. Its true power lies in specificity: researchers can tailor fluorescent probes to target and illuminate specific biological structures. This technique allows dynamic processes, like cellular movements or neural activities, to be observed in real-time. Furthermore, multicolor imaging, made possible by using varied fluorophores, enables simultaneous visualization of multiple structures, revealing complex biological interactions. Enhanced by digital technology, fluorescence microscopy isn't just for observation; it can quantify intensities, track velocities, and measure concentrations. Beyond its visual allure, fluorescence microscopy's precision, adaptability, and analytical prowess make it indispensable for uncovering microscopic biological wonders[34].

2.3 Understanding Volumetric Imaging

In traditional two-dimensional imaging, the depth or third dimension is typically neglected, providing a "flat" view of the world. However, understanding structures in three dimensions is crucial in many fields, particularly biology and medicine. Volumetric imaging addresses this by capturing data across three axes: length, width, and depth. Rather than just obtaining a surface view, volumetric imaging delves deeper, providing a more comprehensive and spatially accurate depiction of samples.

One of the primary ways to capture the depth or z-dimension is by taking a series of "slices" or "sections" through the sample. Here's how various techniques achieve this:

1. **Optical Sectioning:** In methods like confocal and two-photon microscopy, a focused plane or slice of the specimen is illuminated and imaged, while out-of-focus light from other planes is largely excluded. By moving the focus through the sample, a series of 2D slices is obtained, which can then be reconstructed to provide a 3D representation[31].
2. **Physical Sectioning:** In electron microscopy and some forms of light microscopy, samples are physically sliced into ultra-thin sections using devices like microtomes. These sections are imaged sequentially, and the collected data is used to reconstruct the sample in 3D[35].
3. **Tomography:** Techniques like CT (Computed Tomography) or Optical Projection Tomography work by capturing a series of 2D projections as the sample is rotated about

an axis. Sophisticated algorithms then reconstruct these projections to produce a 3D dataset[36].

4. **Light-sheet microscopy:** Here, a thin sheet of light is used to illuminate a slice of the specimen. As the light sheet moves through the sample, different planes are illuminated sequentially, and the emitted fluorescence from each plane is captured by a camera oriented perpendicular to the light sheet[36].

Each of these techniques, depending on the method used, can provide varying levels of resolution, depth penetration, and contrast. However, the shared goal remains: to understand structures and phenomena not just on the surface, but in their full three-dimensional context. This added depth, quite literally, provides a richer, more informative view of the world at the microscopic scale.

Volumetric imaging has reshaped our understanding of medicine and biology by providing detailed 3D views. Clinically, it enhances tumor detection and treatment planning[37]. It maps complex neural networks[38], elucidates embryonic growth[39], offers clarity on cellular functions[40], and elevates drug testing on 3D cultures[41], bridging the gap between lab studies and clinical trials.

Riding the crest of technological advancement, volumetric imaging has witnessed remarkable evolutions. Breakthroughs like adaptive optics offer unprecedented resolution depths, capturing the tiniest 3D structures[42], while high-speed cameras[43] enable rapid data capture essential for dynamic processes. Concurrently, advances in molecular biology have produced superior fluorescent probes, brightening and refining volumetric fluorescence imaging. The enormous

data this imaging yields has driven the need for robust computational tools, streamlining storage, reconstruction, and analysis. Artificial Intelligence and Machine Learning further enhance image segmentation and predictive modeling[42]. Moreover, the fusion of imaging techniques, like combining fluorescence with electron microscopy[44], provides a holistic view of samples. In essence, these technological strides position volumetric imaging at the vanguard of biological and medical exploration.

2.4 Volumetric Imaging in Fluorescence Microscopy

2.4.1 Importance and Necessity

The convergence of volumetric imaging and fluorescence microscopy has unlocked powerful capabilities. Fluorescence microscopy excels in specificity, using fluorescent probes to highlight specific structures or processes amidst often contrast-less biological backgrounds. Volumetric imaging, conversely, excels in-depth, capturing the specimen in layers to render a 3D spatial context for the fluorescent signals. This combination facilitates specifically labeling structures and seeing them within a 3D framework. Thereby, it allows dynamic processes, interactions, and functions to be observed in real-time.

The synthesis of these two techniques has had profound impacts across numerous research areas. In neuroscience, tools like light-sheet fluorescence microscopy have enabled

comprehensive neural circuit mapping in organisms, revealing insights into neural behaviors and anomalies. In oncology, researchers can now closely study the 3D morphology of tumors, understanding their structure, blood supply, and interactions with the surrounding milieu, thereby informing more precise treatments. The capabilities extend to stem cell research, where scientists track the differentiation and integration of stem cells within 3D cultures, and to environmental studies where microbial communities in samples like water or soil are visualized in their true spatial configurations, illuminating complex ecological relationships.

Moreover, the pharmaceutical industry is reaping the benefits. Drug interactions within 3D cell cultures or organ-like structures can be observed, granting valuable data on a drug's effectiveness, delivery, and potential side effects. These success stories emphasize the immense potential of merging volumetric imaging with fluorescence microscopy. As advancements in both realms continue, the horizon looks promising for even more revolutionary insights into the microscopic universe.

2.4.2 Techniques Used in Volumetric Imaging in Fluorescence Microscopy

2.4.2.1 Widefield microscopy

Wide-field microscopy, also referred to as epi-fluorescence microscopy, is a common form of light microscopy that offers several significant advantages for the observation of biological

specimens. This technique illuminates the entire field of view uniformly, allowing for simultaneous observation of all points within a specimen [45]. Because of this, wide-field microscopy is especially useful for rapid imaging applications and for observing dynamic processes within living cells.

The basic operating principle of wide-field microscopy involves illuminating the sample with a broad, unfocused beam of light that covers the entire field of view. In fluorescence applications, the light excites fluorescent molecules within the sample, causing them to emit light at a longer wavelength. This emitted light is then captured through the microscope objective, separated from the excitation light using a dichroic mirror and emission filter, and imaged onto a camera [24,30,45]. By capturing all the light from a specimen simultaneously, wide-field microscopy can rapidly generate an image.

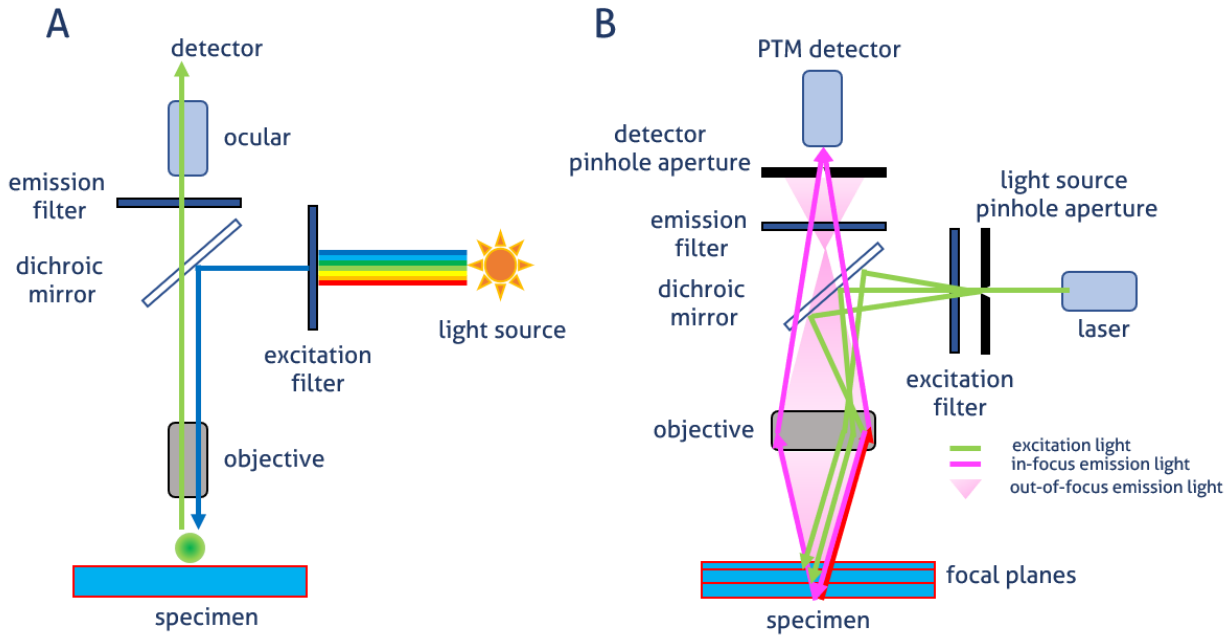

Figure 2.1. Widefield and confocal microscope. A) Schematic of the widefield microscope. B) The structure of the confocal microscope [46].

Despite its speed and simplicity, wide-field microscopy does have certain limitations. One is that it is less able to discriminate out-of-focus information. When imaging thicker specimens, the microscope collects light from all planes of the specimen simultaneously, leading to potentially blurred images due to an out-of-focus light [31]. This is especially true when dealing with three-dimensional biological samples, such as tissues or multicellular organisms. Techniques such as deconvolution and optical sectioning can help to overcome these limitations and improve image clarity [31].

Nevertheless, with advancements in imaging technologies and data processing techniques, wide-field microscopy continues to play a crucial role in biological research. For instance, it has been widely used for applications such as the calcium imaging [47], where rapid imaging is needed to capture transient changes in intracellular calcium levels. Additionally, wide-field microscopy is generally more accessible and affordable compared to more advanced microscopy techniques like confocal or two-photon microscopy, making it a vital tool for many researchers and laboratories worldwide.

2.4.2.2 Confocal Microscopy

Confocal microscopy is a specialized optical imaging technique used primarily in biological research and industrial inspection, known for its ability to generate high-resolution, three-dimensional images of specimens. This powerful tool operates by employing the principle of point illumination and detection. In a confocal microscope, the sample is illuminated with a

focused point of light, and the light returning from the sample is filtered through a small aperture (the confocal pinhole) before reaching the detector. By only allowing in-focus light to reach the detector, the confocal microscope eliminates out-of-focus light, resulting in a sharp, clear image with a high degree of contrast and resolution [31].

The confocal microscope uses a laser as its light source, which provides the high-intensity and monochromatic light necessary for the system to work effectively. The laser light is focused onto a single point in the sample and then raster-scanned across the sample in a grid pattern to generate an image. The light returning from the sample is then passed through the confocal pinhole, and only the light that is precisely in focus is able to pass through the pinhole and reach the detector [31]. This mechanism, known as optical sectioning, enables the collection of images from different depths in the sample, which can then be compiled to form a detailed three-dimensional representation [31].

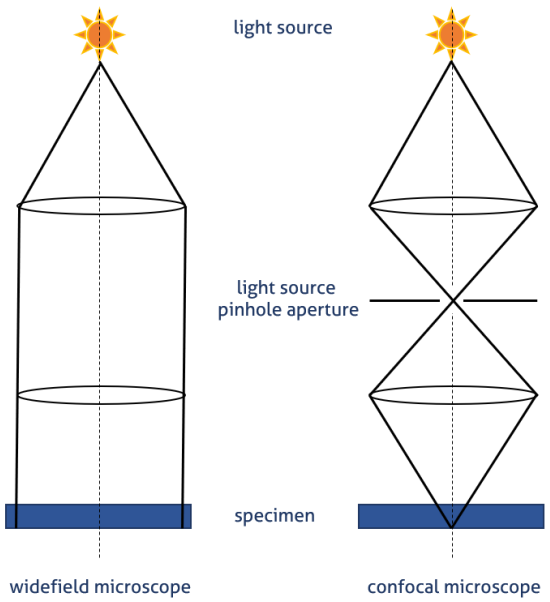

Figure 2.2. Path of light in the widefield and confocal microscope. a) the whole of the specimen is illuminated by the light source in the widefield microscope. b) In a confocal microscope, the light passes through the pinhole and focuses on only a small volume of the specimen [46].

One major advantage of confocal microscopy is its ability to provide high-resolution, three-dimensional images of specimens. Because it effectively eliminates out-of-focus light, the resultant images have a high contrast and clear detail [31]. Additionally, confocal microscopy allows for precise control over the depth of field, isolation of image planes within thick specimens, and the ability to collect serial optical sections from thick specimens [31]. These features make it an invaluable tool in fields such as cell biology, neuroscience, and developmental biology.

Despite its many benefits, confocal microscopy also has limitations. The technique may cause damage to live cells due to the high-intensity laser light, potentially limiting its utility in live-cell imaging [31]. Moreover, the need for a pinhole can restrict the amount of light that reaches the detector, resulting in longer acquisition times and potentially dimmer images [31]. Recent advancements in confocal microscopy, including spinning disk and two-photon confocal microscopy, are aimed at addressing some of these limitations, offering faster image acquisition and reduced phototoxicity, respectively [31].

2.4.2.3 Light sheet Microscopy

Light sheet microscopy, also known as selective plane illumination microscopy (SPIM), is a fluorescence microscopy technique that allows for the imaging of large biological specimens with

less photodamage and photobleaching [48,49] than traditional methods, like confocal or two-photon microscopy.

In light sheet microscopy, the sample is illuminated with a thin sheet of laser light (rather than a point, as in confocal microscopy) which is oriented perpendicular to the detection objective. This allows the illumination of only a single plane of the sample at a time, which can greatly reduce photodamage and photobleaching to the rest of the specimen [48,49].

Images are then taken by a camera (not a point detector), which records an entire plane of fluorescence at once. This technique enables three-dimensional imaging by translating the light sheet through the specimen or moving the specimen through the stationary light sheet and capturing a stack of images, each representing a different focal plane [49].

Because of these features, light sheet microscopy is particularly advantageous for imaging larger, living specimens over extended periods, making it a valuable tool for developmental biology and other disciplines where three-dimensional, time-lapse recordings of living organisms are needed[40]. However, the requirement for optical access from multiple directions require special sample preparation techniques, such as mounting the specimen in a transparent gel.

The primary components of a light sheet microscope setup include a light source, cylindrical lenses, or other beam-shaping optics to generate a thin sheet of light, a scanning system, a detection objective, and a camera[40,49].

In the setup, the light source, which is often a laser, is passed through beam-shaping optics that manipulate the light into a thin sheet. The most common method to generate a light sheet is to use a cylindrical lens, which focuses light in one dimension, thereby creating a light sheet.

However, more advanced setups might use spatial light modulators to get better control of the shape and thickness of the light sheet[50].

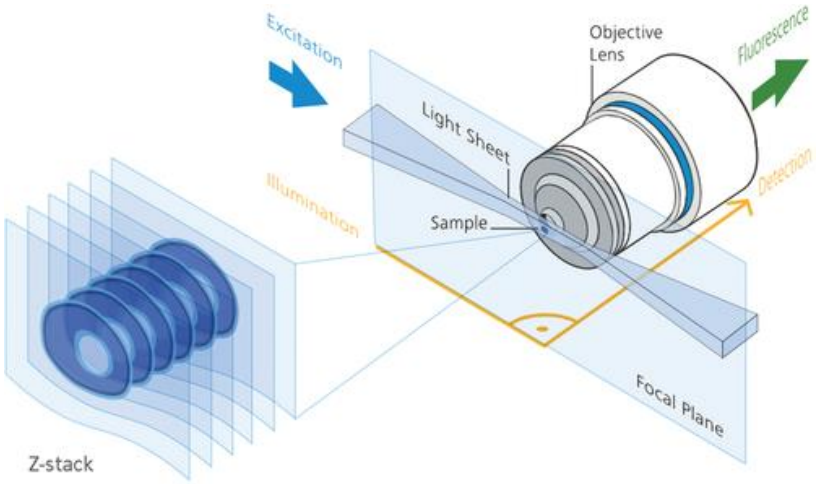

Figure 2.3. Schematic of a light sheet microscope. A cylindrical lens generates a sheet of light that illuminates a specific plane within the sample. Fluorescence generated from this plane of the sample is subsequently detected by an objective lens, which is set in an orthogonal arrangement. By moving the sample through the light sheet, a 3D image stack of the sample is generated. “Copyright: ZEISS” [51].

The scanning system is a galvo mirror responsible for translating the light sheet through the sample[40] or a motorized stage to physically move the specimen through the stationary light sheet [48,49].

The detection objective and camera are positioned orthogonal to the illumination path. When the thin sheet of light interacts with the fluorescently labeled specimen, it excites the fluorescent molecules which then emit light. This emitted light is collected by the detection objective and then imaged by the camera. The images are collected as the specimen is moved through the light sheet, building a stack of 2D images that can be reconstructed into a 3D representation of the specimen [48,49].

This is the basic setup for a single-sided light sheet microscope, which illuminates the sample from one side. There are also dual-sided setups, where two light sheets are created and projected onto the sample from opposite sides [52,53]. This can increase the uniformity of the illumination and reduce shadowing effects, especially in larger samples.

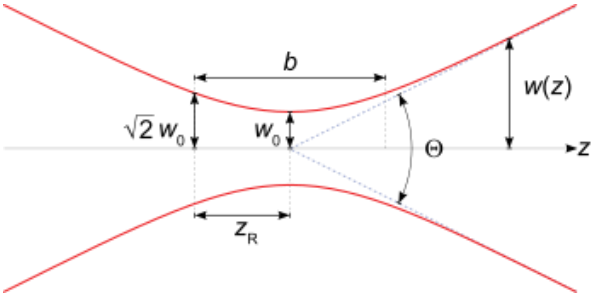

Figure 2.4. Confocal parameter of a light sheet microscope. Rayleigh length (Z_R) and width of the light sheet ($W(Z)$) [54].

In light sheet microscopy, the light sheet is characterized by two main parameters: its waist (i.e., its minimum width, also known as "thickness") and the Rayleigh range or confocal parameter, which essentially gives the length over which the light sheet remains approximately focused through the detection objective lens [49].

The width (w) of the light sheet at its waist (the narrowest point) can be calculated by the formula

$$w = \lambda / (\pi\, NA) \tag{2.1}$$

Here, λ is the wavelength of the emitted light, and NA is the numerical aperture of the illumination objective [49].

The confocal parameter or Rayleigh range (Z_R) represents the distance along the beam from the beam waist (the location where the beam has its smallest diameter) to the place where the area of the beam's cross-section doubles [49]. In simpler terms, it's the distance over which the beam's intensity decreases by half. It can be calculated using the formula [49]

$$Z_R = n\pi\, w^2 / \lambda \quad (2.2)$$

In this equation, w is the width of the beam at its waist. These formulas reveal some important properties of light sheet microscopy. To get a thinner light sheet, one can use a larger NA. It is important to note that the axial resolution is controlled by the waist of the light sheet and lateral resolution is determined by the NA of the detection objective lens [48]. Here, the confocal parameter (Rayleigh range) represents the FOV. Hence, increasing the NA of the illumination objective lens will decrease the confocal parameter, meaning that having better axial resolution will cause a lower FOV [48]. Therefore, there's a trade-off between the thickness of the light sheet and the length over which it stays focused. This can be an important consideration when imaging large samples where it may be necessary to maintain the focus of the light sheet over a long distance.

2.5 Challenges in Volumetric Imaging in Fluorescence Microscopy

2.5.1 Technical Challenges: Image Quality, Speed of Imaging, Sample Preparation

While volumetric imaging in fluorescence microscopy has revolutionized research capabilities, it's not without its challenges. One of the primary concerns is maintaining optimal image clarity, especially when imaging deep into specimens. Factors like light scattering, aberrations, and reduced photon collection efficiency at greater depths can compromise image quality.

Overcoming these demands the continuous refinement of optical components, adaptive optics systems, and the use of longer-wavelength excitation sources.

Fast imaging is crucial for capturing dynamic processes but often comes at the cost of reduced image quality or increased phototoxicity. Achieving a balance requires advanced scanning techniques, high-speed cameras, and efficient illumination systems that minimize light exposure while maximizing data collection.

The nature of the sample can significantly impact imaging quality. Preparing specimens for volumetric fluorescence microscopy demands considerations like optimal sectioning (if needed), appropriate fluorescent labeling, and minimizing light scattering components. Some samples may also require clearing techniques to reduce opacity and enhance imaging depth.

2.5.2 Biological Challenges: Photobleaching and Phototoxicity

Continuous exposure to excitation light can degrade fluorophores, causing them to lose their ability to fluoresce—a phenomenon known as photobleaching. This not only dims the sample's fluorescence but can also compromise the accuracy of quantitative studies. Researchers often counter this by using photostable fluorophores or minimizing light exposure with techniques like pulsed illumination.

Light exposure, especially from high-intensity sources, can harm biological samples. Phototoxicity can lead to cellular damage, functional disruptions, or even cell death. For live imaging, this

presents a major hurdle. Solutions include using lower light intensities, longer wavelength light sources that are less damaging, and antioxidants to mitigate reactive oxygen species produced during fluorescence.

2.5.3. Computational Challenges

Volumetric imaging generates vast amounts of data, especially when capturing high-resolution, multicolor images over extended periods. Efficient data storage solutions, data compression techniques, and scalable storage architectures are needed to manage this influx of information.

Processing and analyzing volumetric fluorescence microscopy data demand sophisticated software tools. Challenges include 3D image reconstruction, noise reduction, and segmentation of intricate structures. Additionally, when studying dynamic processes, temporal data analysis adds another layer of complexity.

Machine learning and artificial intelligence offer potential solutions to many computational challenges in volumetric imaging. They can assist in image segmentation, pattern recognition, and data classification, especially in complex or noisy datasets. However, integrating these tools requires expertise, computational resources, and curated training datasets to ensure accurate and meaningful results.

Despite these challenges, the field of volumetric imaging in fluorescence microscopy continues to advance, driven by a combination of technological innovations, computational breakthroughs, and ever-present scientific curiosity.

2.6 Adaptive Elements in Volumetric Imaging

Remote focusing techniques in microscopy are vital tools that allow for fast, dynamic adjustment of the imaging plane without moving the microscope objective or the specimen. They provide an invaluable advantage in modern microscopy, particularly in applications that require rapid scanning across different focal planes, such as in three-dimensional imaging, and time-lapse studies of biological phenomena. Remote focusing can be achieved using a variety of methods including optical, mechanical, and electronic means. Some optical methods include the use of adaptive optics (deformable mirrors and spatial light modulators) and tunable lenses, both of which can alter the focus without the need for any mechanical movement. Alternatively, another method is using high NA remote focusing, employing pupil-matched objective lenses.

Adaptive optics, initially developed for astronomy to correct atmospheric distortions when viewing celestial bodies, has found significant use in microscopy. It works by introducing a deformable mirror or spatial light modulator into the light path that can change shape under the control of a computer, correcting for aberrations in the light path and enabling rapid changes in focus. Tunable lenses, on the other hand, can alter their optical power to change the focal plane. They work by applying an electrical current, which changes the shape of the lens and hence its focusing properties. Moreover, the high NA remote focusing technique involves two objective

lenses that are pupil matched through the construction of a 4f system in between. This system generates a perfect imaging system, capable of creating a replica of a sample at the focus of the remote objective. By placing a mirror at the focus of the remote objective and enabling it's moving back and forth, one can effectively perform a scan of the sample. These techniques, along with others, make remote focusing a flexible and powerful approach for achieving high-resolution, dynamic imaging in modern microscopy. In the following section, we will delve deeper into the understanding of remote-focusing techniques employed in microscopy.

2.6.1 Tunable lenses

Tunable lenses, also known as adaptive or adjustable lenses, offer the ability to change their focal length in real time. This adaptability lends itself to a wide range of applications, including but not limited to, industrial inspection, microscopy, medical imaging, communications, and robotics. The main advantage of tunable lenses is that they can focus on different distances without needing to physically move the lens. This is particularly useful in settings where quick, precise adjustments are required or where space is limited.

The different types of tunable lenses can be categorized based on the principle they operate on.

1.Electrowetting Lenses: These lenses are built upon the concept of electrowetting. They utilize a conductive liquid and an insulating liquid, both of which are unmixable. The shape of the interface between these two liquids can be controlled by applying a voltage, thereby changing

the focal length. These lenses are often used in compact applications due to their low power consumption and small size [55,56].

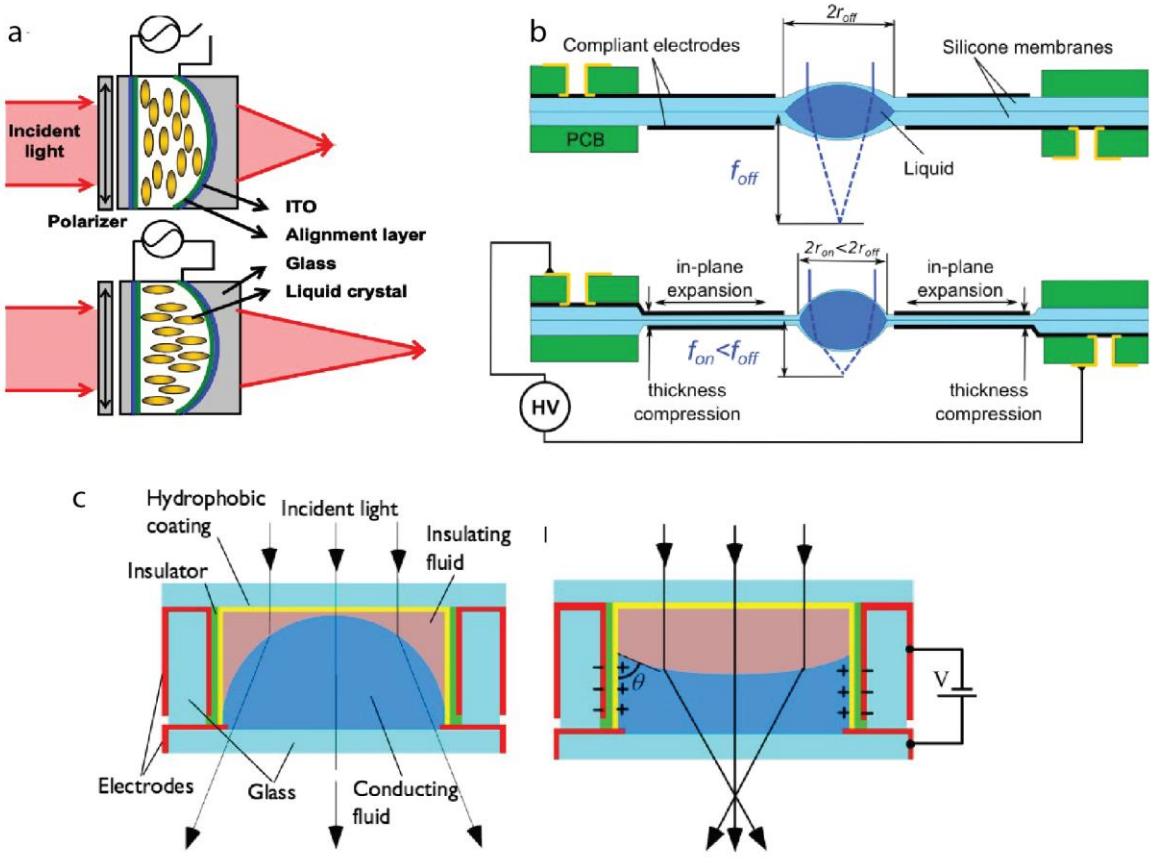

Figure 2.5. Tunable lenses. a) operation of liquid crystal lens when the applied voltage is off and on. The orientation of liquid crystal changes by voltage thereby changing the effective refractive index of the lens [57]. b) An ultra-fast, plastic-based tunable lens that can alter its focal length by 20% in under 200 microseconds, using electrostatic pressure to change lens shape when voltage is applied [58]. c) Electrowetting lens comprises conducting and insulating fluids. The curvature of the lens changes by voltage [59].

2.Liquid Crystal Lenses: In these types of lenses, the orientation of liquid crystal molecules is altered by an electric field, thereby changing the effective refractive index of the lens. This in turn changes the focal length. These lenses are particularly useful for applications that require a large aperture and low power consumption [57].

3.Elastic Lenses: These are usually made from elastic materials such as elastomers or gels. By mechanically deforming the lens, either by applying pressure or by stretching it, the focal length can be changed. These lenses have the advantage of being relatively simple and inexpensive to produce. However, their response time tends to be slower than other types of tunable lenses [60].

4.Tunable Acoustic Gradient (TAG) Lenses: These lenses operate by sending an ultrasonic wave through a medium (usually a fluid), which creates a gradient in the refractive index of the fluid. The wave frequency can be adjusted to change the lens's focal length. TAG lenses have a very fast response time, on the order of microseconds [61].

5.Dielectric Elastomer Lenses: In these lenses, a voltage is applied across a dielectric elastomer, which causes it to deform. The deformation changes the curvature of the lens and hence its focal length [62].

The choice of the tunable lens type is largely dependent on the application. The considerations include the desired range of focal lengths, the speed at which the focal length needs to be changed, the optical quality required, the power consumption, and the physical size of the lens.

2.6.2 Spatial Light Modulator (SLM)

A Spatial Light Modulator (SLM) is an optical device that imposes some form of spatially varying modulation on a beam of light. The modulation might change the light's phase, amplitude, or

polarization. Essentially, SLMs can be seen as dynamic holograms that can manipulate light to form complex optical fields. There are two primary types of spatial light modulators.

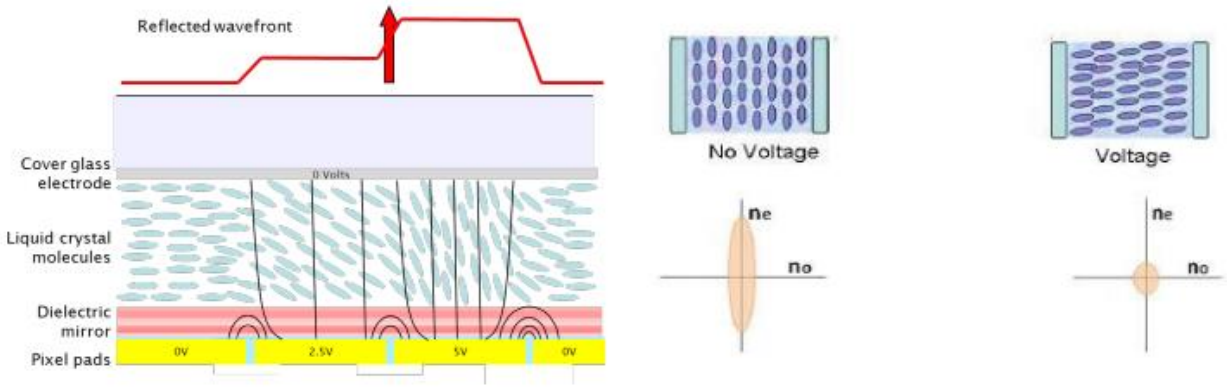

Figure 2.6. Spatial light modulator (SLM). The Liquid Crystal on Silicon Spatial Light Modulator (LCOS SLM) is a technology in which liquid crystals are positioned between a pixelated silicon backplane and a cover glass. Each pixel works as a capacitor whose charge can be adjusted to rotate liquid crystal molecules above it. This rotation alters the refractive index, thereby changing the phase, amplitude, and polarization of the incoming light. The polarization state is altered when the light is linearly polarized at 45° to the long axis, and amplitude modulation happens when the light from the SLM passes through a linear polarizer. These principles are used to manipulate light in numerous experimental layouts [63].

1.Amplitude Spatial Light Modulators

Amplitude Spatial Light Modulators (ASLMs) are devices that can modify the intensity, or amplitude, of the light that passes through or is reflected by it. The modulation of the light's amplitude is typically achieved by utilizing different types of liquid crystal technology, similar to that found in displays, such as Liquid Crystal on Silicon (LCOS). The liquid crystal elements in these devices can be electrically controlled to change their orientation and hence their optical properties, which then results in a modulation of the light's intensity [64].

2.Phase Spatial Light Modulators

Phase Spatial Light Modulators (PSLMs) are devices that manipulate the phase of light independently at different points across the beam's profile. This is accomplished by using a layer of liquid crystals, like the ASLMs. The orientation of the liquid crystals changes under the influence of an applied electric field, causing a corresponding change in the refractive index experienced by light passing through or reflecting off the device. This, in turn, causes a phase shift in the light [64].

SLMs can be made using various technologies, including Liquid Crystal (LC) technology [64] and Micro-Electro-Mechanical Systems (MEMS) [65]. For instance, in a Liquid Crystal SLM, each pixel in SLM corresponds to a liquid crystal cell, which can be manipulated to vary the phase or amplitude of the incident light [64]. MEMS-based SLMs often function using an array of tiny mirrors, each of which can be tilted to alter the phase of the reflected light [65].

The ability to control light on a per-pixel basis gives SLMs a very high level of precision and makes them very useful in fields like microscopy, laser imaging, optical data storage, optical computing, and telecommunications, among others.

2.6.3 Deformable Mirror (DM)

A Deformable Mirror (DM) is an adaptive optical element that is capable of dynamically altering its shape or surface profile. These mirrors are designed to compensate for aberrations or distortions in an incoming light wavefront, which can be caused by atmospheric turbulence,

imperfections in optical components, or heat and mechanical vibrations in a system, among other things.

Deformable mirrors contain several actuators positioned across the back of the mirror's surface. When these actuators move, they cause the reflective surface of the mirror to deform, allowing the mirror to take on a wide range of shapes. By adjusting the shape of the mirror, it's possible to correct distortions in the light wavefront, resulting in a clearer and sharper image [66].

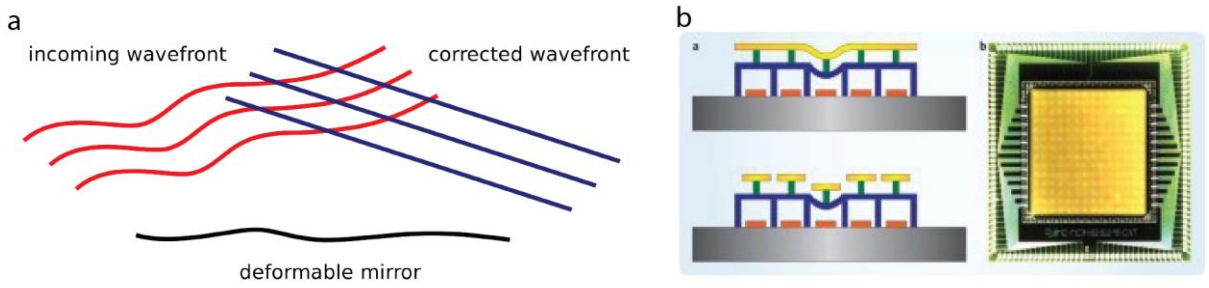

Figure 2.7. Deformable mirror (DM). a) Upon encountering the deformable mirror, the light's wavefront can be corrected [67]. b) Schematic cross-section of continuous and segmented MEMS DM [66].

Here are two common types of deformable mirrors:

1.Micro-Electro-Mechanical Systems (MEMS) Deformable Mirrors: These are made using MEMS technology, where tiny mirrors are etched onto a silicon substrate. Each micro-mirror corresponds to one or more actuators that can tilt it, changing the reflected light's phase and amplitude [66]. MEMS DMs are small, relatively inexpensive, and can have a high number of actuators.

2.Piezoelectric Deformable Mirrors: These mirrors use piezoelectric actuators to deform the mirror surface. Piezoelectric materials change shape when an electric voltage is applied, providing precise control over the mirror's shape [38]. These types of DMs are often used in high-power laser systems and astronomy.

Deformable mirrors are key components in adaptive optics systems, which are used in a variety of fields. In astronomy, they're used to correct for the distortions caused by atmospheric turbulence, allowing telescopes to capture clearer images of distant celestial bodies [66]. They are also used in vision science to improve the imaging of the retina [69], in microscopy to adjust focus spot and enhance image quality [70,71], and in laser systems to correct for various aberrations and achieve a desired beam shape or intensity distribution [72].

2.6.4 Pupil-Matched Remote Focusing (pmRF)

Perfect Imaging

In optical systems, with rotationally symmetric around the optic axis, it's important to consider the concept of perfect imaging systems. These are systems that can create a stigmatic image from any point within a three-dimensional space, meaning all rays from a single point in the object space converge at a single point in the image space [73].

These systems require specific constraints in their design. According to Maxwell, the magnification (M) must be constant in all directions and its magnitude should be the ratio of refractive indices of the object and image spaces [73]:

$$M = n_1/n_2 \tag{2.3}$$

Additionally, all conjugate rays should propagate at the same angle relative to the optic axis [73], i.e.,

$$\gamma_1 = \gamma_2 \tag{2.4}$$

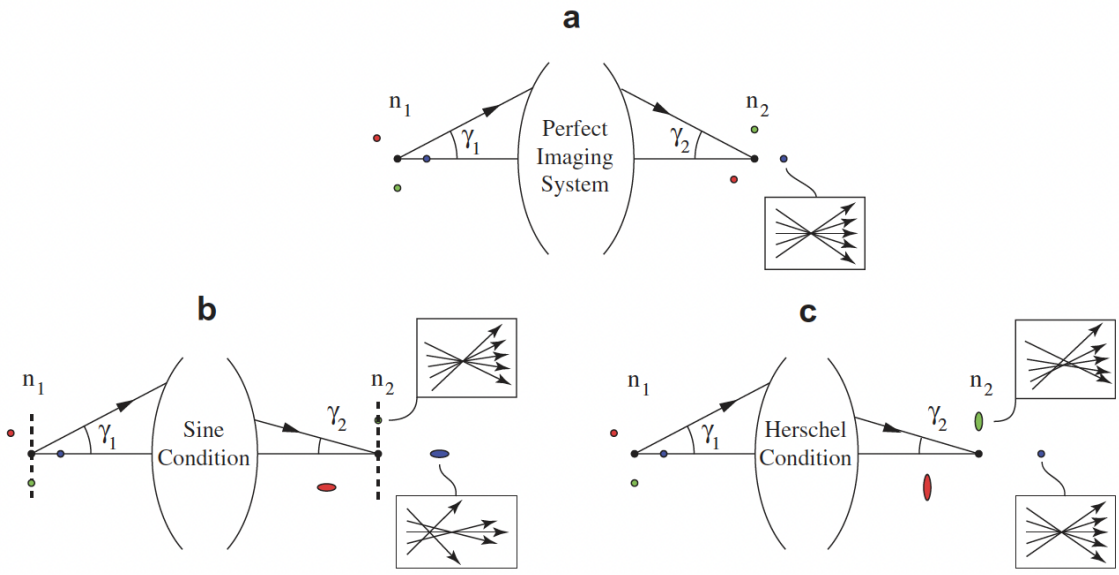

Figure 2.8. The creation of images of four distinct points of a sample in various imaging systems. a) Perfect imaging system. b) Sine condition. c) Herschel condition [73].

However, any system that doesn't satisfy these parameters cannot be considered a perfect imaging system. This is often seen in microscopy where devices are designed to magnify subjects, which inevitably compromises perfect three-dimensional imaging. Yet, perfect imaging can still be maintained for some points within the object space. This is possible through two design

conditions: the sine condition (supporting perfect imaging of points in a plane perpendicular to the optic axis) and the Herschel condition (allowing perfect imaging of points along the axis) [73]. The choice between these two conditions depends on the specific requirements of the use case.

The geometry and optical principles in high Numerical Aperture (NA) objective lens

The objective can be modeled as a pair of principal surfaces that are spherical and planar. When a point source located at the origin emanates a spherical wave, it is altered into a plane wave upon crossing the principal sphere. This plane wave can then be focused into a point in the image space by a low NA tube lens. If the point source is displaced, the spherical wave's interaction with the principal sphere creates a more complex phase profile.

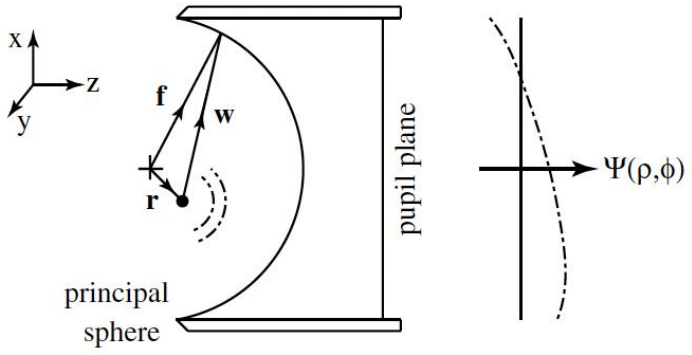

Figure 2.9. The geometric design of a high numerical aperture (NA) microscope objective. The objective lens is represented as a pair of principal surfaces, one spherical and the other planar [73].

If the point source is located at (x, y, z) (cartesian coordinate system, centered at the focal point of the principal sphere), the phase profile in the pupil plane as a function of the point source position can be expressed as [73]:

$$\Psi(\rho, \phi; \mathbf{r}) \approx nk \sin\alpha \left\{ x\rho\cos\phi + y\rho\sin\phi + z\sqrt{\frac{1}{\sin^2\alpha} - \rho^2} \right\}, \tag{2-5}$$

Here, ρ represents the normalized radius and ϕ is the polar angle in the polar coordinate system at the pupil plane. The semi-aperture acceptance angle of the lens is given by α while the medium in which the point source is located has a refractive index of n, and k signifies the wavevector.

The pupil function indicates that lateral displacements of the point source create plane waves in the pupil, which are then focused by the tube lens to laterally displaced points in the image space. Axial displacements, on the other hand, lead to a curved phase profile [73].

Expanding the phase profile for axial displacement (equation (2-5)) shows that it can be considered as the phase profile for high NA defocus [73].

$$znk\sqrt{1 - \rho^2\sin^2\alpha} = znk\left\{1 - \frac{\rho^2\sin^2\alpha}{2} + \frac{\rho^4\sin^4\alpha}{8} + \cdots\right\}, \tag{2-6}$$

The quadratic term accurately describes focusing using the tube lens in the paraxial regime. However, the higher-order terms that represent spherical aberrations cannot be compensated by the tube lens. This implies a breakdown of stigmatic imaging for points where these aberrations occur [73]. This is a fundamental insight for understanding the limitations of such optical systems.

To refocus an object under examination in a high numerical aperture (NA) microscope system without physically moving the object, an ideal imaging system can be created that reproduces the three-dimensional distribution of object space within the focal region of a second high NA lens. This is achieved with a magnification of n_1/n_2. A subsequent microscope is used to image this replicated space. Refocusing can then be performed by moving this subsequent microscope with the replicated image, thereby avoiding any direct movement of the object itself [73].

This method involves two objective lenses arranged back-to-back, with a 4f imaging stage mapping their pupil planes. These lenses denoted L1 and L2, don't necessarily need to be identical and can operate with different immersion media (n_1 and n_2) [73].

Phase profiles for a point source in the focal region (x, y, z) of L1 [73]:

$$\Psi_1(\rho_1,\phi)=kn_1\sin\alpha\left(x\rho_1\cos\phi+y\rho_1\sin\phi+z\left(\frac{1}{\sin^2\alpha_1}-\rho_1^2\right)^{1/2}\right) \tag{2-7}$$

And the corresponding stigmatically focused point in the focal region $(n_1/n_2)\times(x,y,z)$ is provided as [73]:

$$\Psi_2(\rho_2,\phi)=kn_2\sin\alpha_2\frac{n_1}{n_2}\times\left(x\rho_2\cos\phi+y\rho_2\sin\phi+z\left(\frac{1}{\sin^2\alpha_2}-\rho_2^2\right)^{1/2}\right) \tag{2-8}$$

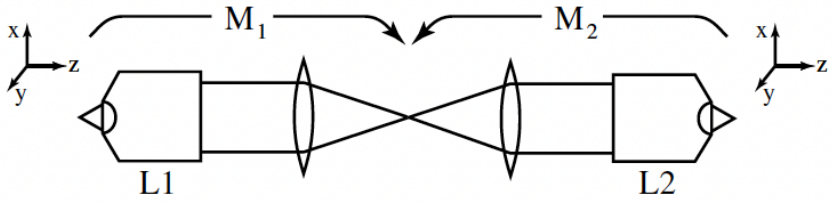

Figure 2.10. Perfect imaging system. Two back-to-back microscope systems can function as a perfect imaging system if total magnification is relative refractive indices [73].

If the magnification of the 4f system is defined as:

$$M = \frac{\rho_2}{\rho_1} = \frac{\sin \alpha_1}{\sin \alpha_2} \tag{2-9}$$

the pupil planes of the two lenses are mapped together. Under this condition, the two-phase profiles are identical (equations (2-7), (2-8)), and the point source is stigmatically imaged in the focal region of L2 [73].

As a result, the system images a three-dimensional region of object space with an isotropic magnification factor of n_1/n_2, meeting the criteria for a perfect imaging system. In this setup (Fig. 10), the first microscope magnifies the object, and the second one demagnifies it, providing a uniform magnification ratio essential for 3D imaging. Spherical distortion from the first system is compensated by the second one [73].

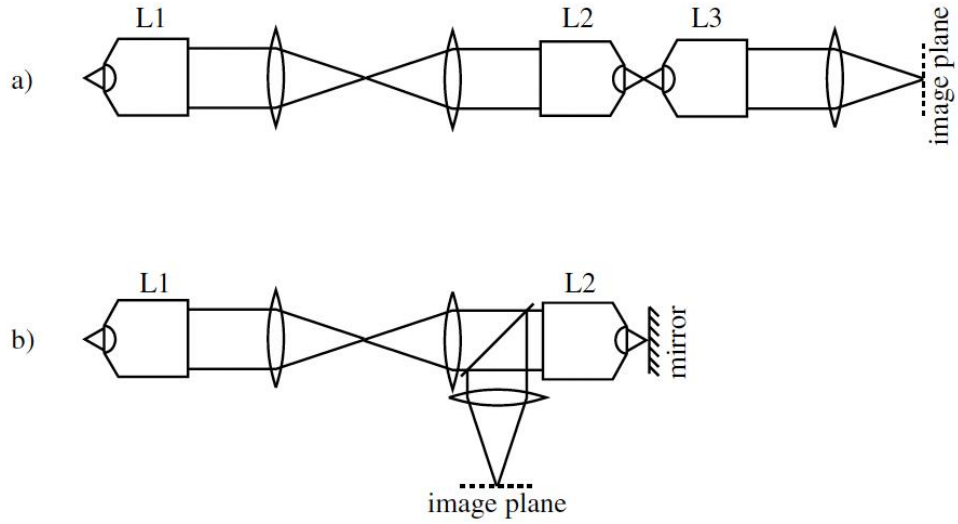

Figure 2.11. Pupil-matched remote focusing system. a) Imaging the replica of the sample generated by the L1 and L2 through the third microscope (L3). b) By placing the mirror at the focus of objective L2, the reflected light is captured by L2 (instead of L3) and then imaged onto the camera [73].

A third microscope system is employed to magnify the replica of the object. By adjusting the position of the third lens, different planes can be imaged without spherical distortion, enabling remote refocusing without moving the original object [73].

A second system is proposed for faster refocusing. In this system, the third lens is removed, instead, a flat mirror is used to reflect the rays into the second lens. A beam splitter redirects these rays toward the final lens and image plane. This setup provides faster refocusing speeds than moving the third lens in the initial system [73].

2.7 Summary

The chapter provides a comprehensive overview of volumetric imaging in fluorescence microscopy, tracing its historical evolution and exploring its multifaceted applications and challenges. Volumetric imaging, which captures three-dimensional data of biological samples, has been pivotal in unveiling intricate cellular structures and processes, offering a more in-depth understanding compared to traditional two-dimensional imaging. The combination of volumetric imaging and fluorescence microscopy, a technique where certain molecules are illuminated to emit light and visualized, allows for precise observation and analysis of specific structures and functions within biological specimens. This integrated approach has had significant implications in various research areas, including neuroscience, oncology, stem cell research, environmental studies, and pharmaceuticals, allowing for real-time observation and understanding of dynamic processes and interactions at the microscopic level.

However, while this technique is revolutionary, it is not without its challenges. These include maintaining image clarity, especially when imaging deep into specimens; managing rapid imaging processes without compromising image quality or causing damage to the specimens; and dealing with substantial amounts of generated data, requiring robust storage and sophisticated processing tools. Furthermore, the field grapples with issues like photobleaching, where fluorophores lose their ability to fluoresce over time, and phototoxicity, where the light used can damage the biological samples. Despite these challenges, the convergence of volumetric and fluorescence microscopy continues to be an indispensable tool in biological and medical research, driving further technological and computational advancements in the field.

Furthermore, adaptive elements in volumetric imaging like tunable lenses, spatial light modulators (SLMs), deformable mirrors (DMs), and pupil-matched remote focusing (pmRF) technologies enable dynamic, high-resolution microscopy without physically moving the microscope objective or specimen. Tunable lenses, which adjust focal length in real-time, facilitate applications in various fields including microscopy, medical imaging, and robotics. SLMs, imposing spatial modulation on light beams, are critical for creating complex optical fields, utilized in microscopy, data storage, and telecommunications. Deformable mirrors dynamically change shape to correct distortions in light wavefronts, improving image clarity in areas like astronomy, retinal imaging, and laser systems. Pupil-matched remote focusing helps create perfect imaging systems, essential for refocusing and three-dimensional imaging in high numerical aperture (NA) microscope systems without disturbing the original object. Each adaptive element offers unique advantages, with selection dependent on specific application requirements and desired outcomes.

In summation, the chapter reviews volumetric imaging in fluorescence microscopy, highlighting its importance in cellular research and its challenges. Despite issues like image clarity, speed, and resolution, adaptive technologies enhance their application in volumetric imaging in biology.

CHAPTER 3: Enhancement of Axially Swept Light Sheet Microscopy (ASLM) via Dual-Focus Generation in Remote Focusing Systems

3.1. Introduction

In this chapter, we demonstrate the development of an advanced method for creating a thin light sheet over a large field of view (FOV) utilizing axially swept light sheet microscopy (ASLM)[48]. We also introduce an innovative technique designed to address the challenges associated with low signal-to-noise ratio and limited imaging speed, building upon our previously published findings[48]. These enhancements pave the way for more efficient and higher-quality imaging in various microscopy applications.

3.1.1 Background

Confocal and two-photon microscopes are currently the workhorses of most biomedical imaging facilities. However, owing to their slow imaging speed, high light dosage, poor penetration depth, and anisotropic resolution these microscopes are not suitable for imaging large tissues [49]. Light sheet fluorescence microscopy (LSFM) is a rapidly evolving microscopy technique that can acquire fast 3D images with high spatiotemporal resolutions across large field-of-views (FOVs) yet being gentle to the sample which greatly reduces photobleaching and phototoxicity [49,74]. Owing to its myriad of advantages LSFM has been used to image across various biomedical fields involving

in vivo imaging of cells, spheroids, tissues, organs, embryos (worms, flies, zebrafish, etc.), and plants [49,74–83].

LSFM, in its simplest form, employs a Gaussian beam that is focused in only one direction through a cylindrical lens and excites fluorophores only in the in-focus plane of a detection objective. This is accomplished using two orthogonal objectives where an excitation objective generates a thin sheet of light at the focal plane of a detection objective. This plane is imaged directly onto a scientific Complementary Metal-Oxide-Semiconductor (sCMOS) camera, resulting in a massive parallelization of data collection compared to the point scanning microscopes [49]. It should be noted here that in LSFM the lateral resolution is determined by the numerical aperture (NA) of the detection objective while the waist of the excitation beam governs the resolution in the third dimension (also called *z*-resolution or axial resolution). Because of the beam's Gaussian nature, there exists a trade-off between the thickness of the beam waist and the area over which the beam can be approximated as a sheet of light. Therefore, an everlasting impetus in the field of LSFM research circles around alleviating this problem: How to create a thin sheet of light over a large FOV?

3.1.2. Advancements in Light Sheet Fluorescence Microscopy (LSFM) to Enhance FOV

Several methods have been proposed to extend the FOV without sacrificing the *z*-resolution. Propagation invariant beams, such as Bessel beams [84–87], Lattice light sheet [50], Airy beams [88], and Field synthesis light sheet [89], theoretically retain a narrow beam waist over an

arbitrarily long distance. However, for one-photon illumination, these techniques do not provide a significant improvement over a Gaussian beam in confocal parameter and beam waist [90]. Another approach, classified as multi-view imaging, generates final images by computationally fusing the complementary views [52,53,83,91–94]. This is often carried out by rotating the sample in a conventional LSFM [92,95], swapping perpendicular illumination and detection arm sequentially (e.g., Dual-view iSPIM) [91], using two illuminations and detection objectives arranged along two perpendicular axes (e.g., MuVi-SPIM, SiMView) [52,53,93], and four orthogonal objectives where each objective has both illumination and detection arm (e.g., IsoView) [94]. The Multiview imaging technique improves the spatial resolution and makes resolution more isotropic across the FOV. Nevertheless, because one has to image the sample from multiple directions, this method reduces imaging speed and requires massive post-processing. Another approach called digitally-scanned-light sheet microcopy (DSLM) creates a time-averaged light sheet by rapidly moving the beam vertically and horizontally through the sample [96]. When the Bessel beam is scanned laterally, this method creates out-of-focus blur and reduces image resolution and contrast owing to the beam sidelobes [97]. Tiling light sheet selective plane illumination microscopy (TLS-SPIM) employs a similar scheme and tiles light sheets to multiple positions in multiple frames so that a large FOV can be imaged by repeating this process and stitching all images together [98–100]. However, this technique suffers from low imaging speed, high computational post-processing, and poor axial resolution compared to conventional LSFMs.

3.1.3. Axially Swept Light Sheet Microscopy (ASLM): Understanding and Addressing Its Challenges

Lately, axially swept light sheet microscopy (ASLM) based microscopes have shown great promise when it came to volumetric imaging of large tissues at diffraction-limited isotropic resolution. In this technique, the waist of the light sheet is translated in the axial direction and synchronized with the rolling shutter readout of the sCMOS camera [101]. This ensures only the light sheet's waist is captured while rejecting the out-of-focus blur thereby providing robust optical sectioning and high-resolution imaging over large FOVs [101]. Ever since its conception [101], several microscopes designed and built upon this core technique have come into existence [102–104]. For example, the Cleared-tissue ASLM (ctASLM) extended this idea to develop an instrument that was capable of imaging at sub-300 nm level isotropic resolution while maintaining compatibility with all tissue-clearing methods [102]. Another initiative is known as the mesoscale selective plane-illumination microscope (mesoSPIM), which integrated ASLM by employing an electrotuneable lens (ETL) showed that volumetric imaging of centimeter-sized cleared samples with 5-6 µm isotropic resolution was possible within minutes [103]. However, as explained further in the 'Method' section, ASLM suffers from two fundamental constraints: low detection signal and the limited frame rate for full-FOV-imaging, both of which adversely affect the imaging speed. These further complicate matters such as fluorophore selection for the biological specimens, achievable temporal resolution, and ease of alignment while building the instrument.

Here, we propose to upgrade the core ASLM technique to create a new imaging platform that not only improves the detection signal but also allows these microscopes to image faster. Furthermore,

our suggested technique simplifies the process of determining ASLM parameters, making this new version far superior to the previous one. We demonstrate the performance of our microscope by imaging fluorescent beads and a chemically cleared mouse brain.

3.2. Method

3.2.1. Principles of Single Focus and Dual Focus in ASLM

LSFMs that employ Gaussian illumination suffer from a fundamental problem: the axial resolution decreases, thereby resulting in blurred images, as one moves away from the waist of the light sheet, as shown in **Fig. 3.1.a.** ASLM overcomes this by creating a virtual light sheet with a diffraction-limited waist over the entire FOV of the camera. The working principle of ASLM can be seen in **Fig. 3.1.b.** The waist of the light sheet is swept along the propagation direction of the light such that it is synchronized with the camera readout using the rolling shutter feature of sCMOS cameras [101,102]. Since the light sheet is imaged directly onto the 2D array of the sCMOS camera, high optical sectioning is achieved by restricting the active pixels of the 2D array to roughly twice the Rayleigh length of the beam [101]. By rejecting the out-of-focus blur this scheme allows one to maintain a high NA beam waist over a large FOV.

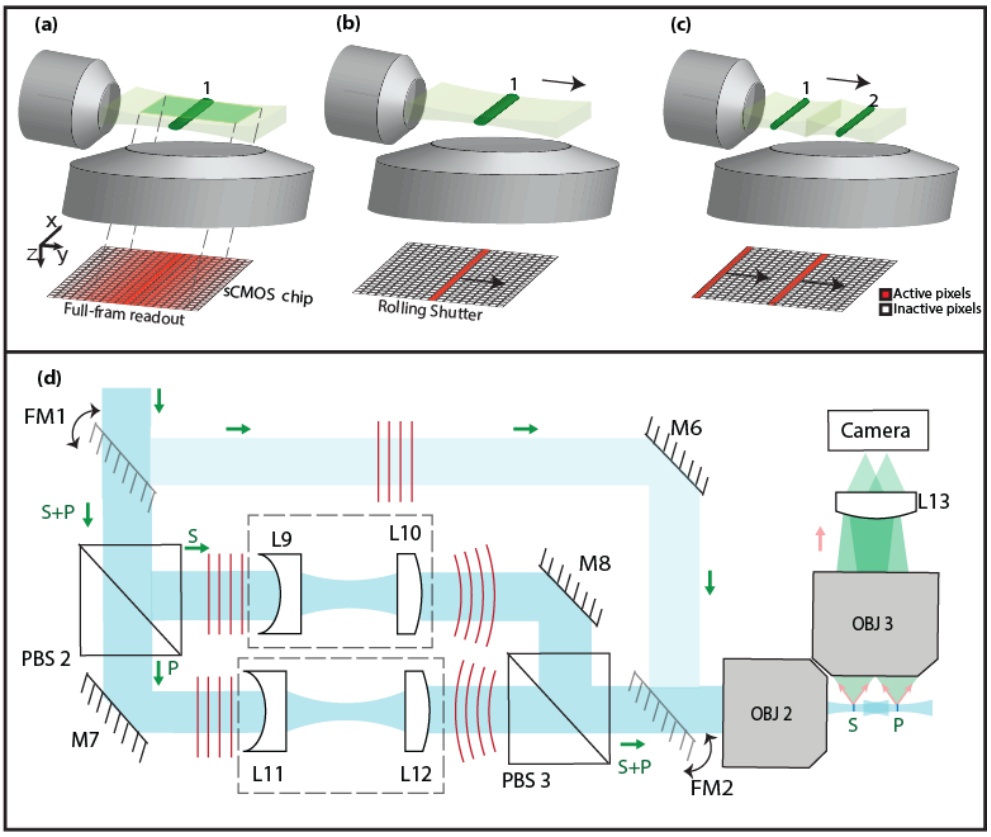

Figure 3.1. Optical principle of a traditional LSFM and ASLM in single and dual-focus configurations. (a) The variable thickness of a Gaussian light sheet causes uneven illumination across the FOV in a traditional LSFM which limits the axial resolution only to the waist of the light sheet. (b) The ASLM works on the premise of scanning a high NA light sheet in its axial direction. The light sheet scan is synchronized with the rolling shutter readout of an sCMOS camera, which is tuned to the width of the beam waist. This decouples the FOV from beam-waist limited axial resolution. (c) In dual-focus ASLM mode, two foci are staggered and scanned simultaneously only over half of the sCMOS chip. (d) In a dual-focus setup, the incoming beam is split by PBS2 into two paths with S and P polarizations. The combination of a concave and a convex lens, (L9 and L10) for S and (L11 and L12) for P, alters the wavefronts of the two beams differently. When combined using PBS3 and fed into objective lens 2 (OBJ2), it generates two axially staggering spots. Flip mirrors (FM1 and FM2) were engaged to create a standard single-focus ASLM for benchmarking.

However, the ASLM concept has two fundamental drawbacks. First, in ASLM, as explained above, to capture one frame within a certain acquisition time, a strip of active pixels is rolled over the entire camera chip, as shown in **Fig. 3.1.b.** Therefore, the effective exposure time at each pixel is only a fraction of the acquisition time which ultimately lowers the signal-to-noise ratio (SNR). As a result, the user at this point should either increase the excitation power to generate higher

fluorescence signal which may result in an adverse phototoxic effect, or capture the images at a lower frame-rate which effectively increases the exposure time at each pixel but slows down imaging speed. Therefore, ASLM-based microscopes make a compromise of either improving imaging speed or SNR. Second, all ASLM-based microscopes use some sort of actuator that sweeps the light sheet along the axial direction. For ctASLM this is the linear-focus-actuator (LFA) located in the remote focusing arm while for mesoSPIM an ETL is used for this purpose. Because the light sheet is scanned over the entire camera chip, these actuators must oscillate with larger strokes to cover the entire FOV. For sub-100 ms acquisition times, non-linear phenomena start to creep in through the actuators which makes the scan of the light sheet non-uniform. In practice, this non-uniformity not only limits scanning to about 10 frames/sec over the full FOV but also makes finding ASLM parameters to synchronize the rolling-shutter and the sweeping focus difficult.

Here we propose to alleviate these problems by simultaneously scanning two staggered light sheets in the axial direction and simultaneously synchronizing two rolling shutters in the two halves. By doing so each light sheet covers only one-half of the FOV and together cover the entire FOV in one camera acquisition cycle. This concept is shown schematically in **Fig. 3.1.c**. There are several advantages of this method as opposed to scanning a single focus across the entire FOV. First, since each light sheet covers only half of the FOV, the effective exposure time at the active pixels doubles, thereby improving the acquired signal strength two-fold. The second, sweeping dual focus over half FOV requires shorter travel for the LFA. This shorter travel eases the oscillatory motion of the LFA. This not only results in a more uniform scan of the foci across the FOV at shorter acquisition times but also makes finding the ASLM parameters a lot easier. The third advantage manifests through the viewpoint of the highest achievable frame rate. For the same detection

photon budget, scanning dual-focus will allow users to scan at twice the frame rate using the same laser power in each waist (as that of the single-focus case). This can be particularly useful, in terms of the total acquisition time, for samples where the strength of the fluorescence signal is not an issue.

3.2.2. Microscope Layout

Figure 3.2 depicts the schematic arrangement of our microscope. Four Coherent Obis lasers (LX 405-100C, LX 488-50C, LS 561-50, and LX 637-140C) were used for excitation. These where then combined with dichroic beam splitters (LM01-427-25, LM01-503-25, and LM01-613-25, Semrock). To clean up the beams, a 50-mm achromatic doublet (AC254-50-A, ThorLabs), focused the beams through a 30-µm pinhole (P30D, ThorLabs), and the beams were then recollimated using a 200-mm achromatic doublet (AC254-200-A-ML, ThorLabs). A 5× Galilean beam expander (GEB05-A) expands the original beams by 20 folds before being focused with a cylindrical lens (ACY254-50-A, ThorLabs), onto a resonant mirror galvanometer (CRS 4 kHz, Cambridge Technology), driven by a 12-volt power supply (A12MT400, Acopian), to wobble the light sheet. A 200 mm achromatic doublet (AC508- 200-A, ThorLabs), directed the cylindrical lens's one-dimensional focus to passed through a 50:50 polarizing beam splitter (10FC16PB.7, Newport), and a quarter waveplate (AQWP3, Boldervision), before being focused onto a mirror with a 4× microscope objective (XL Fluor ×4, NA 0.28, Olympus Life Sciences). The mirror was attached on a voice coil with a travel of 10 mm, positional repeatability of less than 50 nanometers, and a

response time of less than 3 milliseconds (LFA-2010, Equipment Solutions). The same ×4 objective recaptured the reflected light from the mirror and the second passing through the quarter waveplate rotated the beam's polarization state. Then the light was reflected from the cube polarizing beam splitter and directed toward the illumination objective (Cleared Tissue Objective, NA 0.4 Advanced Scientific Imaging) through the 200-mm and 75-mm achromatic doublets (AC508-200-A and AC508-75-A, ThorLabs). A 3-mm N-BK7 glass piece (37–005, Edmund Optics) was inserted between the ×4 objective and the voice coil actuated mirror to compensate for spherical aberrations. In a dual-focus setup, the beam is split into two paths and then recombined with two polarizing beam splitters (10FC16PB.7, Newport) before collection by a microscope objective (Cleared Tissue Objective, Advanced Scientific Imaging). The beams' wavefronts in each path are altered differently with combination of achromatic doublet and plano-concave lens (AC254-100-A and LC1582-A-ML, ThorLabs) with different separations in each path. As a result, two foci are formed by a microscope objective.

An identical microscope objective (Cleared Tissue Objective, Advanced Scientific Imaging), a tube lens (ITL200-A, ThorLabs), a 6-position motorized filter wheel (FW102C, ThorLabs), and a sCMOS camera (Flash 4.0, Hamamatsu Corporation) made up the detection arm. For emission filters, we used four long-pass filters (FF01-444/20-25, FF01-525/30-25, FF01-505/15-25 and BLP01-647R-25, Semrock), for blue, green, red and far-red, respectively. The specimen, as well as the illumination and detection objectives, were immersed in a large chamber designed using Adobe Inventor and machined through Protolabs (R). To collect a z-stack, a 480-µm travel piezo (Piezo Jena NanoX 400) was used to scan the specimen in a sample-scanning mode. Sub-volumes were

acquired by moving the position of the specimen and the piezo stage with a three-axis motorized stage (3DMS and MP-285A, Sutter Instruments).

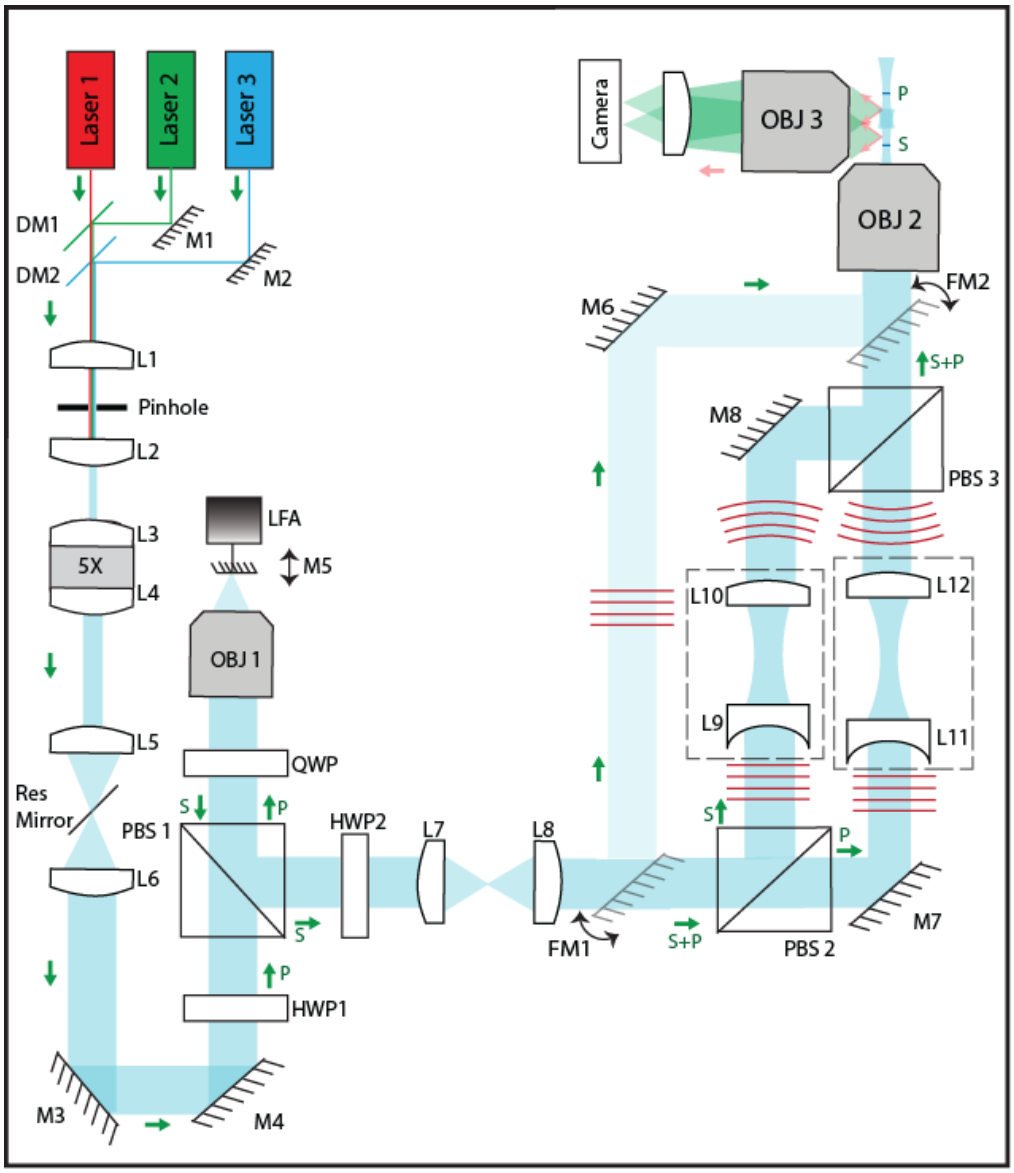

Figure 3.2. Schematic diagram of ASLM with single and dual-focus configurations. The lenses L7 and L8 match the pupil of objective lenses 1 and 2 (OBJ 1 and OBJ 2) to support the remote focusing arm by utilizing flip mirrors (FM1 and FM2) in single-focus arrangements. Moving back and forth the mirror M5, attached to the LFA, sweeps the focus axially. In dual foci configuration, the incoming beam is split into two paths by PBS2. The lenses L9 and L10, as well as lenses L11 and L12 in each path, with different spacing between them, modify the wavefronts of the beam differently, causing OBJ 2 to create two foci at separate points in the axial direction.

Figure 3.1.d and **Fig. 3.2** show the schematic diagram to implement our proposed idea. There are three main concepts that are essential to achieve this goal: (1) generation of two simultaneous light sheets, (2) fast, aberration-free, scanning of these light sheets across half of the FOV such that the entire camera chip is covered yet maintaining a fixed distance between the two foci, and (3) synchronizing the position of sub-array readout on the sCMOS camera with axial scanning of light sheet for the two halves independently. To generate a dual-focus setup, the polarizing beam splitter (PBS2) is used to split the illuminating beam into two paths, which are then fed into a lens assembly each containing a concave (L9 and L11) and a convex lens (L10 and L12). Owing to a different distance between the two lenses in each arm, each of these pairs modifies the wavefront of the beams differently in each path (**Fig. 3.1.d, Fig. 3.2)**. This generates two foci, one with 'S' and another with 'P', which are staggered in space in the axial direction. A mirror attached to the LFA located in the remote focusing arm may move back and forth, to sweep the focus axially and therefore results in the ASLM with a dual-focus configuration (**Fig. 3.1.d, Fig. 3.2**).

3.2. 3. Microscope control

A Dell precision 7920 computer with two processors Intel(R) Xenon(R) Silver 4210R CPU having a processing speed of 2.40 GHz and 2.39 GHz and is integrated with 128 GB RAM was used to acquire the microscopic data. A NVIDIA Quadro RTX 4000 Graphics processing unit (GPU) having dedicated memory of 8 GB and shared memory of 63.8 GB (GPU memory 71.8 GB) was also integrated into the system. 64-bit operating system ×64-based processor facilities the system to operate. LabView 2020 64-bit provides us the opportunity to work with the required software

which includes the LabView Run-Time Engine, Vision Run-Time Module, Vision Development Module and other required drivers like NI-RIO drivers (National Instruments). DCAM-API software was used for the Active Silicon Firebird frame-grabber to actively interfere with the scientific complementary metal-oxide semiconductor (sCMOS) camera (Flash 4.0, model: C13440-20CU) manufactured by Hamamatsu, Japan. It generated deterministic transistor logic (TTL) trigger sequences through 150 Watts shutter instrument (100-240 V~50/60 Hz; model: MP-285A) with a field programmable gate array (FPGA) (PCIe 7852R, National Instruments). The generated triggers control the resonant mirror galvanometers, placement of stage, voice coils, blanking and modulation of laser, firing camera and other external triggers. K-Hyper Terminal software facilitates engaging LFA with the system hardware. Some key features along with some routines under the agreement of material transfer are licensed by the Howard Hughes Medical Institute's Janelia Farms Research Campus.

3.2.4. Optical Alignment of Single Focus and Dual Focus ASLM

Figure 3.3 elucidates the working principle behind this concept by experimentally simulating the idea using a traditional light focus (called 2D focus here onwards) employing a standard achromatic lens (not cylindrical lens) in fluorescein solution. As can be seen, when the 2D focus (**Fig. 3.3.a**) is scanned in the propagation direction with a synchronized rolling shutter it results in a sharp line (**Fig. 3.3.b**). This is because the active pixels on the camera reject the fluorescence arising from

outside the focal volume. A 1D focus (waist of the light sheet) when scanned similarly would become a thin virtual sheet (the concept behind ASLM).

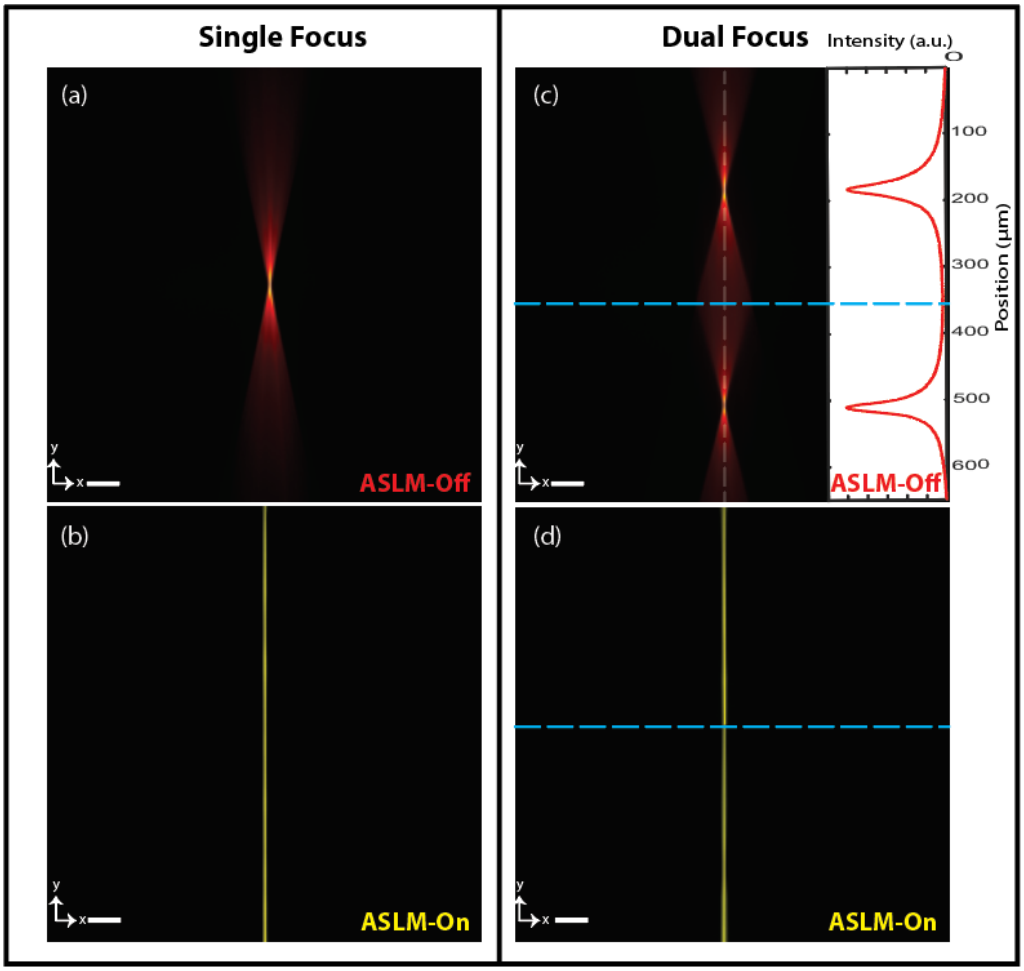

Figure 3.3. Visualization of the proposed concept. (a) Sharp single 2D focus spot at the center of the FOV. (b) Scanning of the single focus. The sharp line is the indication of matched rolling shutter speed with the 2D focus scanning rate for the entire FOV. (c) Sharp dual 2D focus spots on the centers of the individual half FOV. In the inset, the intensity profile shows that the two focus spots are separated enough that there is no out-of-focus contribution of one light sheet into the other. (d) Corresponding image as in (b) with dual-foci. The straight line indicates that the two foci are perfectly aligned, maintain constant separation and synchronized with the rolling shutter for the two FOVs. Scale bar: 50 µm.

Figure 3.**3.c-d** shows the working principle behind our dual-focus concept. When two 2D foci are scanned for only half of the FOV they cover the entire camera chip, and appear as two sharp lines. It should be noted that the purpose of 2D focus is to simply allow the visualization of the focal volume and the resulting ASLM-type-scan in fluorescein and is in no way different than a light sheet where the confinement of light happens in 1D. To ensure that the spurious contribution of unfocused light from the 'tail' of one light sheet does not bleed into the waist of the other, we plotted a line profile through the two foci depicting the intensity profile across the entire FOV (inset of **Fig. 3.3.c).** Owing to a separation of ~335 µm between the two foci, the intensity of out-of-focus light has reduced to near zero. Because these two foci maintain their separation throughout the travel, we can ensure that out-of-focus fluorescence from one light sheet never affects the other thereby preserving the most important feature of ASLM: optical sectioning.

It should be noted that the confocal detection of dual beams has been previously investigated in DSLM-based techniques, albeit in the lateral direction. Two counter-propagating rolling shutter modes have been used to image two parallel light sheets generated using identical illumination objectives facing each other [106], and an acousto-optic deflector (AOD) [107]. However, this counter-propagating movement not only results in inhomogeneous lighting and striping artifacts throughout the whole FOV but also degrades image quality due to crosstalk between the two light sheets. In addition, because these techniques were designed to improve the light confinement in the lateral direction for DSLM, the axial resolution of the light sheet has always been an issue, as in sub-micron isotropic resolution has never been achieved. Our method on the other hand is developed particularly for ASLM and maintains its most salient feature: isotropic sub-micron resolution over a large FOV. Not only do we create two fixed-distance, high-NA, Gaussian light

sheets capable of axial scanning, but our rolling shutters also aren't counter-propagating, as a result, our method doesn't have a crosstalk problem like others.

3.3. Results

3.3.1. Nonlinearity Behavior of Linear Focus Actuator (LFA) in Sweeping Focus

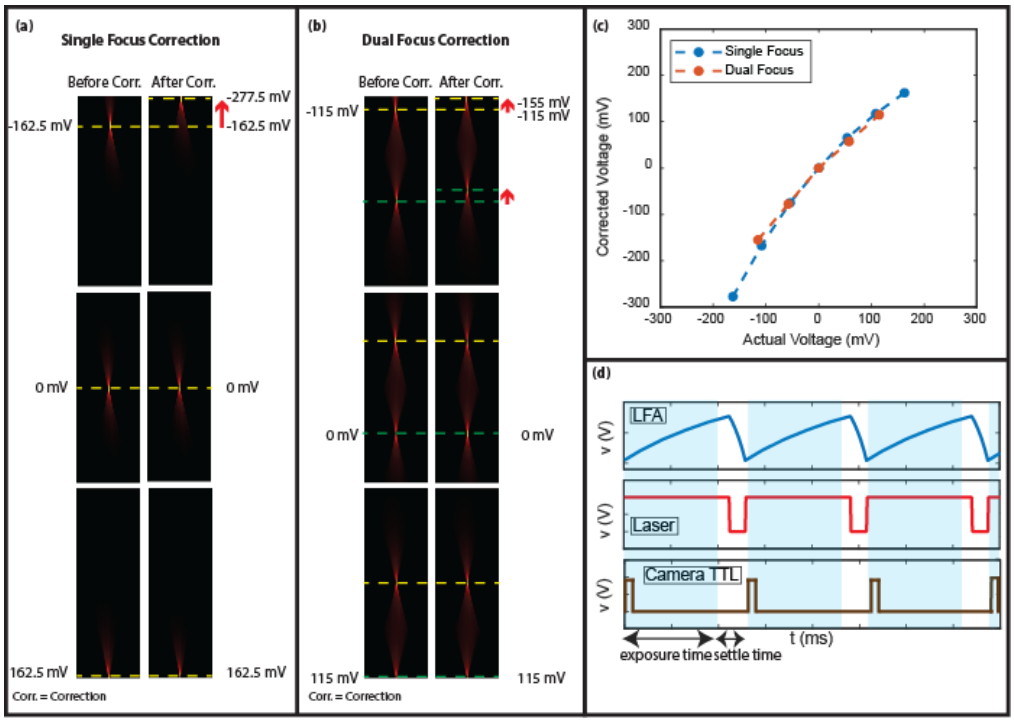

Figure 3.4. Position response of the 2D focus with respect to the applied LFA voltage for (a, left) single and (b, left) dual-focus configuration. (c) The corrected voltage plotted against the actual voltage for single (blue) and dual-focus (red). (a, right) Single-focus and (b, right) dual-focus position response of the 2D focus after applying the correction. One can see that for the dual focus case the correction required is about half of that required for the single focus case. (d) The corrected sawtooth signal for the LFA is synchronized precisely with a series of deterministic transistor-transistor logic (TTL) triggers signal for the camera, laser modulation to carry out ASLM.

As discussed previously, in ASLM, the axial position of the beam is deterministically modulated by an actuator through the remote focusing arm. However, this deterministic requirement can often be compromised by a few interdependent factors: (a) speed of imaging—the smallest acquisition time in which the waist of the light sheet must travel the entire FOV to capture one frame, (b) FOV requirement— which decides the maximum distance the focus needs to travel, and (c) inherent nonlinear response of the LFA to the applied voltage. In **Fig. 3.4** we try to quantify and correct for this nonlinear response by making use of the 2D focus spots. **Figure 3.4.a** (left) shows this nonlinear relationship between the applied voltage and the resulting focus shift for single focus as it is translated across the FOV. This not only makes synchronizing the camera's rolling shutter to the axially moving focus very difficult but also reduces the overall FOV coverage. To overcome this, we designed a correction routine in our control software which, when pre-calibrated, corrects for this nonlinear response by providing additional voltage to the LFA (**Fig. 3.4.a**, right). One can see from **Fig. 3.4.b** that the voltage required to correct for the nonlinearity decreases significantly because the two focus spots now must move only half as much as the single focus case. It should be noted that these corrections are for the static case and act as a coarse adjustment only. When the LFA oscillates rapidly these numbers are adjusted further to generate a more continuous correction. **Figure 3.4.c** shows the corrected voltage for both single and dual-focus mode across the entire FOV. Volumetric scans were then taken by synchronizing these voltages along with digital modulation of lasers and camera trigger pulse train (**Fig. 3.4.d**).

3.3.2. Quantifying FOV coverage for frame-rate assessment

To evaluate how scanning dual-focus improved the imaging speed over traditional ASLM, we employed a 2D focus to carry out ASLM and visualized how well the coverage across the entire FOV was by drawing line profiles. For 100 ms acquisition time, the single focus mode could cover the entire FOV with a sharp line, as measured by line profiles (**Fig. 3.5.a** and **Fig. 3.6.a,d)**. When the camera exposure time was lowered to 50 ms, sharp focus could only be achieved for one-third of the FOV (**Fig. 3.5.b** and **Fig. 3.6.b,e**), while the rest of the FOV appears blurry. Compared to this for the dual-focus setup with even 50 ms camera exposure time, each half of the FOV is scanned by sharp lines of the scanning beam, resulting in a sharp line over the entire FOV as shown in **Fig. 3.5.c** (**Fig. 3.6.c, f**). With these optimized ASLM parameters we simply switched the achromatic lens with a cylindrical lens, to generate light sheet, and imaged a PEGASOS cleared, Thy1-GFP mouse brain (see Supplement 1) [108]. The maximum intensity projection (MIP) of the mouse brain in the XY and YZ directions are shown in **Fig. 3.5.d** using 50 ms acquisition time. Due to the uncompromised sub-micron resolution across the entire FOV, high-quality neuronal imaging of 670×670×200 μm^3 volume could be performed in 30 sec which using a traditional ASLM would have taken over a minute. It should be noted that this two-fold improvement in imaging speed might not seem much for such a small volume but can reduce hours or even days of acquisition time when imaging larger samples.

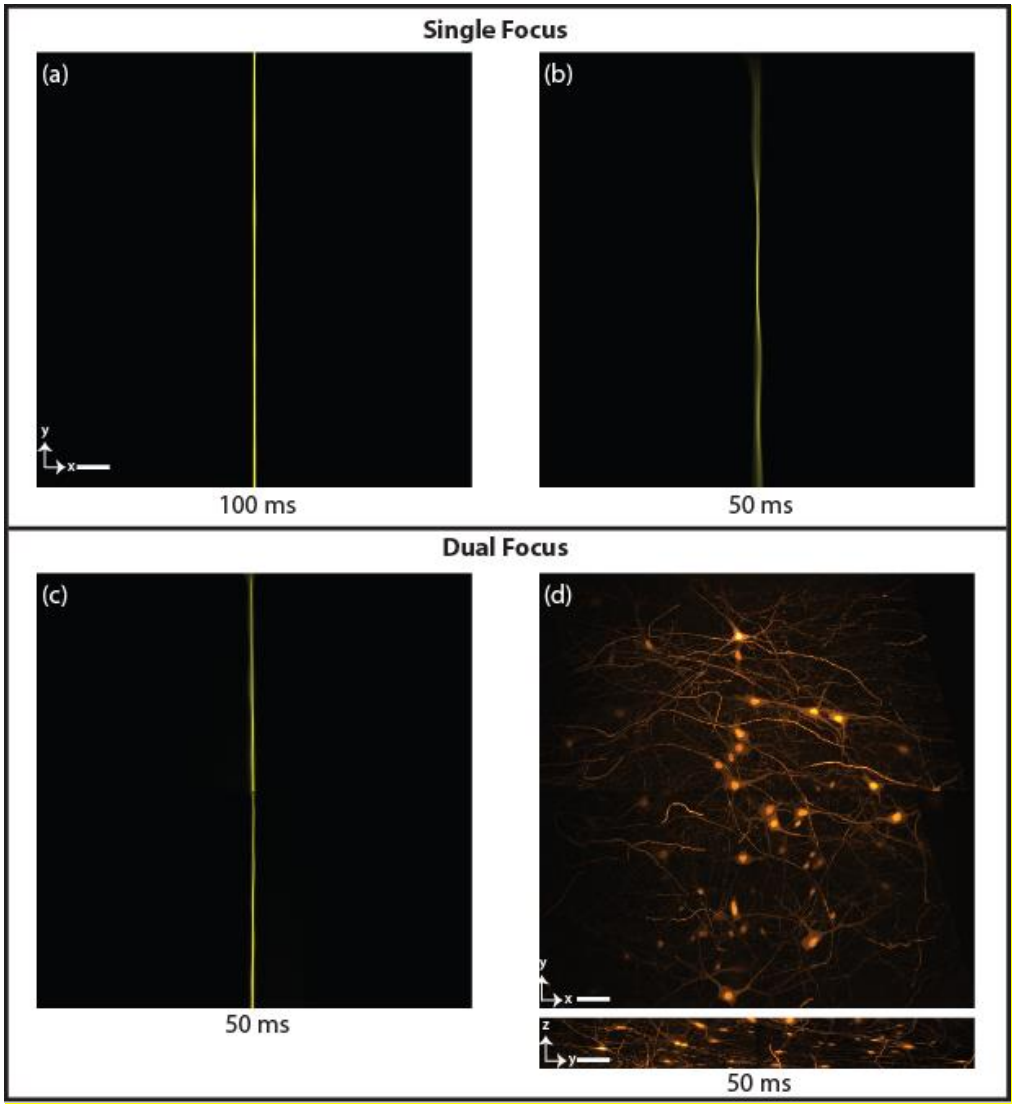

Figure 3.5. XY view of 2D single and dual-focus beams in ASLM mode over 670 × 670 µm^2 FOV in fluorescein solution for different camera exposure times and orthogonal views of mouse brain. XY view of the FOV for single focus arrangement for (a) 100 ms and (b) 50 ms acquisition time. It can be seen that for the 100 ms acquisition time the rolling shutters maintain synchronous motion with the moving focus which is depicted by a sharp line. (b) For 50 ms exposure time, this synchronization becomes very difficult to maintain: depicted by sharp line only for one-third of the FOV and blurry regions towards the edges. (c) Using two foci the full FOV can be scanned even at 50 ms exposure time. This is because of the reduced load on the LFA which now has to travel only half as much distance as the single focus case. (d) Orthogonal views of the mouse brain in a dual-focus light sheet configuration 50 ms exposure time: twice as fast as a traditional ASLM. Scale bar: 50 µm.

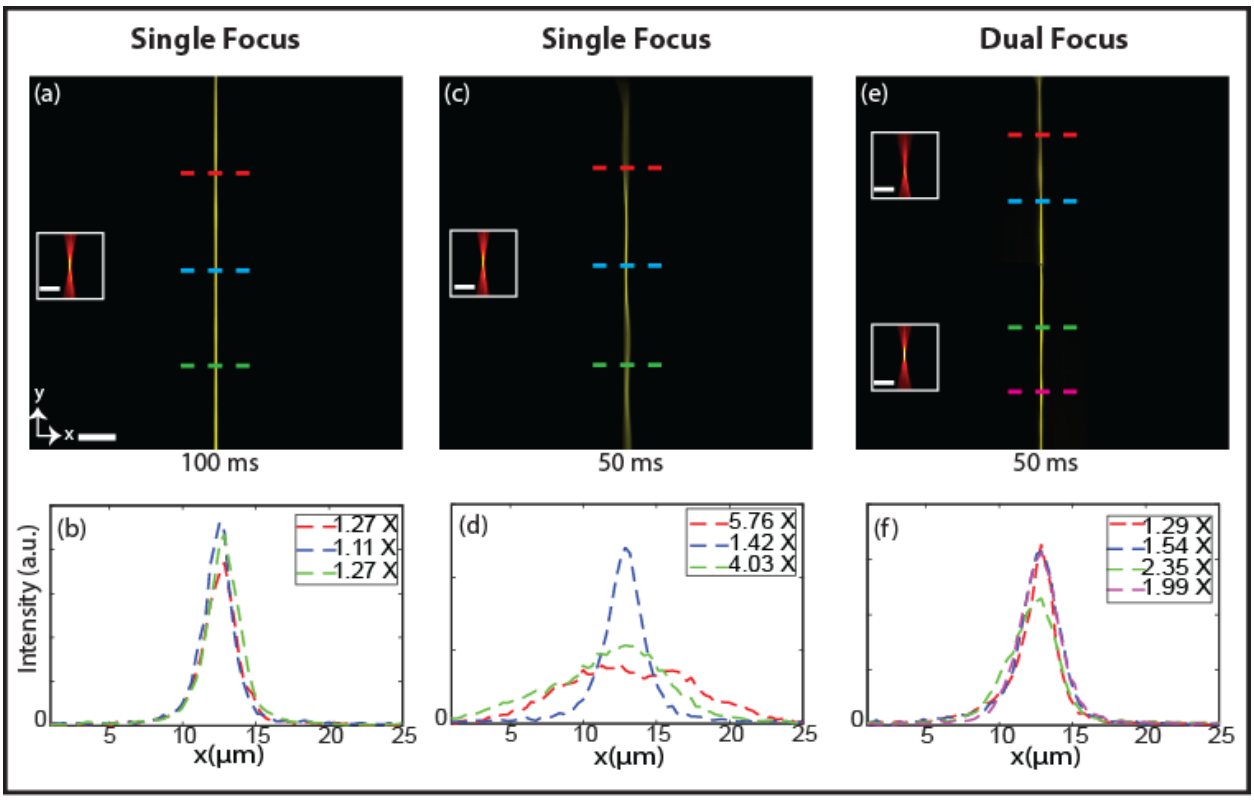

Figure 3.6. Comparison of 670 × 670 μm² FOV coverage of scanning 2D focus in single and dual-focus ASLM mode for different camera exposure times 100 ms, 50 ms and beam intensity profile at different regions of FOV in the propagation direction. The values in the plots are FWHM, normalized with respect to the corresponding 2D focus of LSFM mode (shown in the insets). (a) The whole FOV is covered by a sharp line of 2D scanning beam in a single focus for 100ms. (b) The plots show the beam profile across the FOV shown in (a). The beam is unform across the whole FOV. (c) One-third of FOV in the center is captured by a sharp line of 2D scanning beam while other regions are caught by out-of-focus bluer in single focus for 50ms. (d) The plots show that only the center region is in the focus of the scanning beam in (c). (e) The full FOV is scanned individually by two 2D scanning beams in 50ms in dual-focus resulting a sharp line of scanning beam across the whole FOV. (f) The beam is unform in the whole FOV in (e). The scale bars 50μm in figures and 25μm in insets.

3.3.3. Resolution assessment of the microscope

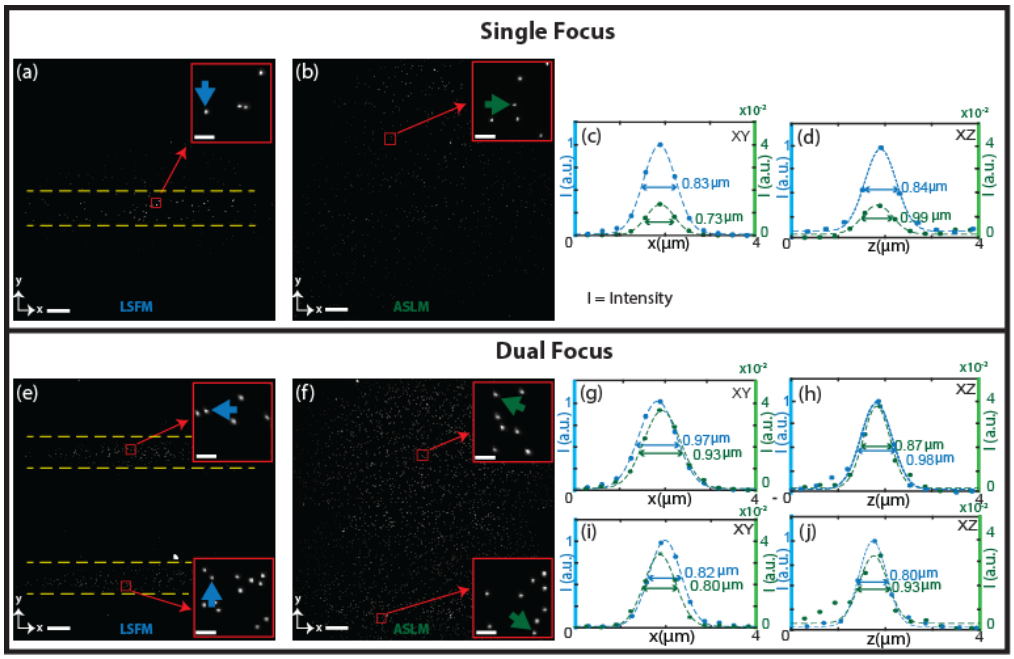

Figure 3.7. Resolution and signal-strength assessment using 500 nm fluorescent beads embedded in agarose gel, imaged by single and dual-focus configurations in LSFM and ASLM mode. (a) The confined region within the dashed-yellow lines contain the light sheet waist in LSFM mode, and insets are the magnified view of the small red boxes. (b) The corresponding ASLM mode shows a uniform FOV coverage (inset: zoomed in view). (c, d) Plots depicting the lateral PSF (blue for LSFM and green for ASLM) (c) and axial PSF (d) of beads picked by arrows in insets. The peak of the ASLM (green) plot is normalized to LSFM intensities (blue). (e) and (f) are the corresponding images for LSFM and ASLM mode employing dual focus mode respectively. The insets show zoomed-in view of a few randomly chosen beads from both halves of the FOV. (g-j) The plots showing the lateral (g, i) and axial (h, j) PSF of beads shown with arrows in insets of (e) and (f). The FWHM of beads was calculated by Gaussian-curve fitting. Scale bar: (a, b, e, and f) 50 µm and (insets) 5 µm

In order to characterize the resolution of the microscope, we imaged 500 nm green fluorescent beads embedded in a 2% agarose gel and measured the full-width-half-max (FWHM) of the point-spread-functions (PSF). Standard magnification calibration slides were used to access the actual magnification of these objectives since their focal lengths and the effective magnification changed with the RI of the immersion medium. We found, for water, with a 200 mm focal length tube lens the effective magnification was 20.21× which ultimately decided the sCMOS pixel size to 0.32 µm.

Figure 3.7.a and **Fig. 3.7.e** show the XY view of MIP of stacks of beads over the entire FOV in single and dual-focus Gaussian light sheet mode, *i.e.*, axial scanning turned off, respectively. The enclosed dashed yellow region depicts the waist of the light sheet since this is where the intensity of the emitted beads is the maximum. The inset, depicted by red boxes, shows an enlarged view of a randomly chosen region with several beads. In order to obtain a quantitative evaluation of our microscope's resolution, we measured the FWHM of the beads shown in these insets (**Fig. 3.7.c-d and Fig. 3.8**). The FWHMs for both cases (~0.8 μm) suggest that we achieve aberration-free diffraction-limited resolution. When the axial scanning is turned on, both single and dual-focus results in uniform coverage for the entire FOV (**Fig. 3.7.b** and **Fig 3.7.f**). Similar FWHM measurements of the PSFs indicate that while we have diffraction-limited performance in the case of single-focus (**Fig. 3.7. c-d**), the resolution of the microscope in dual-focus mode decreases slightly (**Fig. 3.7. g-j**). This is because of the aberrations induced by two extra lenses we used in the remote focusing arm in order to separate the two foci (L11/L12 and L9/L10 in **Fig. 3.1.d**). We would like to point out that these are raw, unprocessed images and routine deconvolution operations can certainly improve the final quality even further.

Next, we compared the detection signal performance of dual-focus with the traditional ASLM. For this, we use average intensity measurement from beads for both modes of illumination. So that the comparison can be made fairly the intensities of the PSFs for single and dual-focus ASLM are normalized to their respective Gaussian light sheet mode. This is to ensure that any discrepancies in the illumination laser power, between the two modes, did not affect the detection signal assessment. The total excitation laser power for single and dual-focus the laser power was set at 20mW and 40mW (with each arm receiving 20mW) respectively.

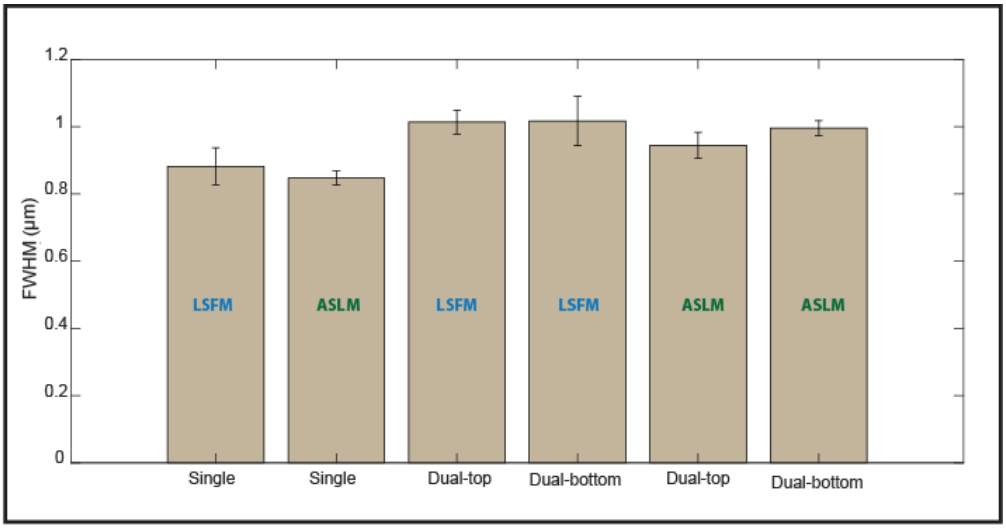

Figure 3.8. FWHM of all beads in red boxes of Fig.5 for various configurations. 10 randomly chosen beads were used to carry out the measurements.

As can be seen from **Fig. 3.7.c**, the average intensity for single focus dropped from 1 a.u. for a Gaussian focus to 0.014 a.u. for ASLM. A similar plot involving two foci (**Fig. 3.7.g** and 3.**7.i**) showed that the intensity changed from 1 a.u. for dual-focus Gaussian mode to 0.037 a.u for ASLM. This 2.5× improvement confirms our original hypothesis that the dual-focus arrangement enhances ASLM's signal strength.

3.3.4. Dual and Single Focus Comparison of Mouse Brain Images

Figure 3.9.a-d compares the MIP of XY and YZ view of a dense neuronal labeling within the cleared brain sample using single and dual-focus ASLM mode. The total excitation laser power for single and dual-focus the laser power was set at 20mW and 40mW (with each arm receiving 20mW) respectively.

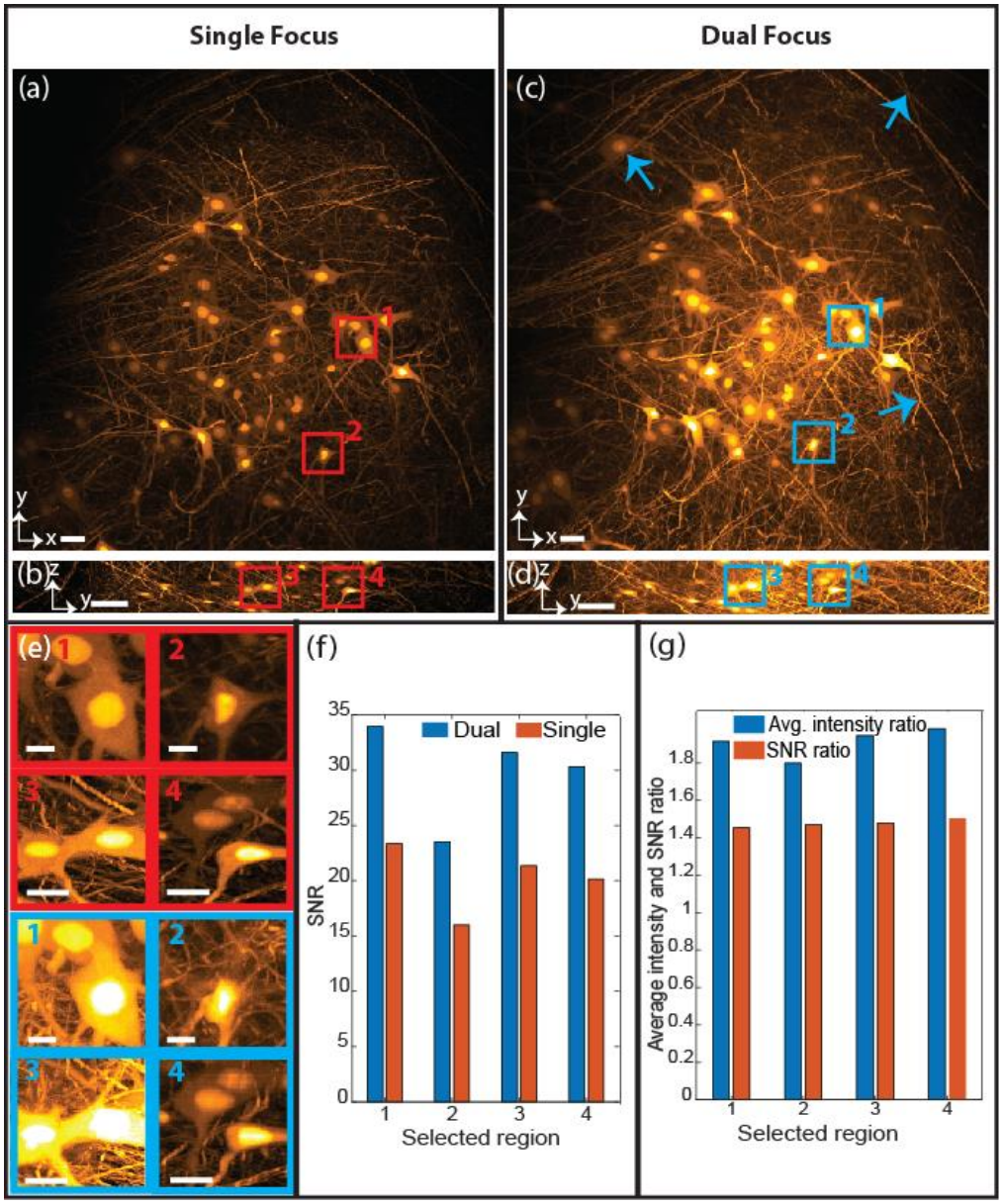

Figure 3.9. Neuronal imaging of mouse brain acquired by single and dual-focus mode for 100 ms camera exposure time. (a-d) Orthogonal views of MIP. To visualize the intensity improvement over dual-focus imaging, the minimum and maximum intensity of both images are set equal. (e) Enlarged view of selected regions from (a-d). (f, g) Quantitative analysis of images shown in (e) in terms of SNR and signal intensities. As can be seen from the bar-charts of (f), dual-focus achieves higher SNR compared to single-focus. Bar charts of (g) depict that for 2× improvement in average signal intensity, for dual-focus, results in a 1.4× SNR improvement. Scale bar: (a-d) 50 µm (e) 10 µm.

When the lowest and highest intensities of both the images were adjusted to roughly similar levels, one can see that lower intensity regions in the brain section become more visible for dual-focus ASLM mode (depicted by blue arrows in **Fig 3.9.c**). In order to quantify the increase in signal-

intensity between single and dual-focus modes, SNR calculations [26,42]. were performed on four randomly chosen regions of **Fig. 3.9.a-d** (as shown in **Fig. 3.9.e**). As can be seen from **Fig. 3.9.f** SNR improvements of up to 10 were observed between the two modes. As is evident from the intensity ratios of **Fig. 3.9.g** a nearly two-fold improvement in average signal intensity results in 1.4-fold improvement in SNR between the two modes. We corroborated this finding by performing a similar analysis on a different section of the mouse brain, as shown in **Fig. 3.10**

In order to compare the images captured by the dual and single focus arrangement, signal-to-noise ratio (SNR) is computed for the selected four regions of both **Fig. 3.9** and **Fig. 3.10**. To quantify the background, a blank image with no sample was acquired. The SNR is computed using the following equation:

$$SNR = \frac{I_s - I_{bg}}{\sqrt{I_s - I_{bg} + \sigma_{bg}^2}} \tag{3.1}$$

where, I_s represents the mean signal intensity of the image, I_{bg} and σ_{bg} are the calculated mean and standard deviation of the background image respectively [26,42].

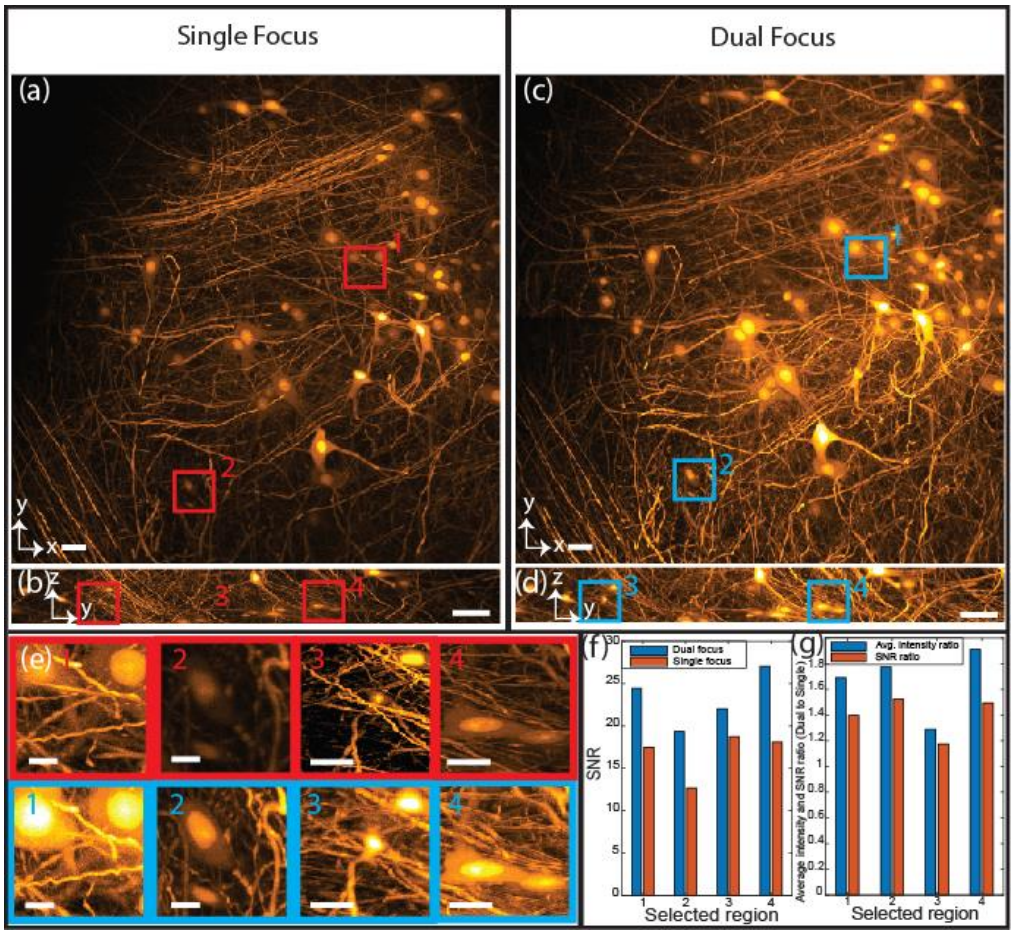

Figure 3.10. Dual and single focus image comparison (using similar assessment as also shown in Fig. 9) for different regions of mouse brain. (a-b) Lateral and axial view of mouse brain images respectively, captured by single focus ASLM arrangement. (c-d) Lateral and axial view for the same region as shown in a and b respectively, captured by dual-focus ASLM. (e) Randomly taken four regions where red and blue boxes represent single and dual focus images respectively. (f) SNR values for these four regions shown in (e). (g) Ratio of average signal intensity and SNR (dual to single) for the chosen four regions shown in (e).

3.4. Discussion

3.4.1. Controlling Axial Separation of Light Sheets

In principle, while it is possible to scan an arbitrary number of light sheets for the gain of better SNR, in practice, there are two major considerations: First, the availability of an sCMOS camera

that can roll the shutter independently in more than two regions. While some emerging sCMOSs have proposed to offer programmable scanning modes [109], these features are in their nascent stage and will need further investigation. Second is the spurious contribution of unfocused light from the 'tail' of one light sheet into the waist of another. This can adversely affect the optical sectioning capability of the ASLM. The actual number is dependent on the NA of the light sheet and the magnification of the detection arm. Our simulations suggest that a maximum of four 0.4 NA light sheets may fit within this FOV, without a significant bleed through. To do this we used the intensity formula for Gaussian beam.

$$I(r,z) = I_0 \left(\frac{w_0}{w(z)}\right)^2 exp\left(\frac{-2r^2}{w(z)^2}\right) \tag{3.2}$$

Here, I_0 is the beam intensity at waist. The variable r denotes the distance from the beam's central axis in the radial direction, and z is the distance along the axis from the waist [110]. The beam waist at z, $w(z)$, can be derived from

$$w(z) = w_0 \sqrt{1 + \left(\frac{z}{z_R}\right)^2} \tag{3.3}$$

where

$$z_R = \frac{\pi w_0^2 n}{\lambda} \tag{3.4}$$

z_R is the Rayleigh length and n is the refractive index of the medium. Figure 3.11 depicts the simulated foci and their intensity profiles along the Z-axis within the Field of View (FOV). For simplicity in this simulation, we used the normalized beam intensity at waist ($I_0 = 1$). This figure clearly demonstrates that as the number of foci increases, there's a noticeable bleed of intensity from one focus to another. To quantify this effect, we assessed the intensity at the Full Width at Half Maximum (FWHM) of each focus and compared it to the intensity at FWHM of a single focus

which there is no bleeding effect (Fig 3.11.a). The resulting intensity overlap at FWHM was found to be 1% for two foci, 10% for four foci, and 26% for six foci.

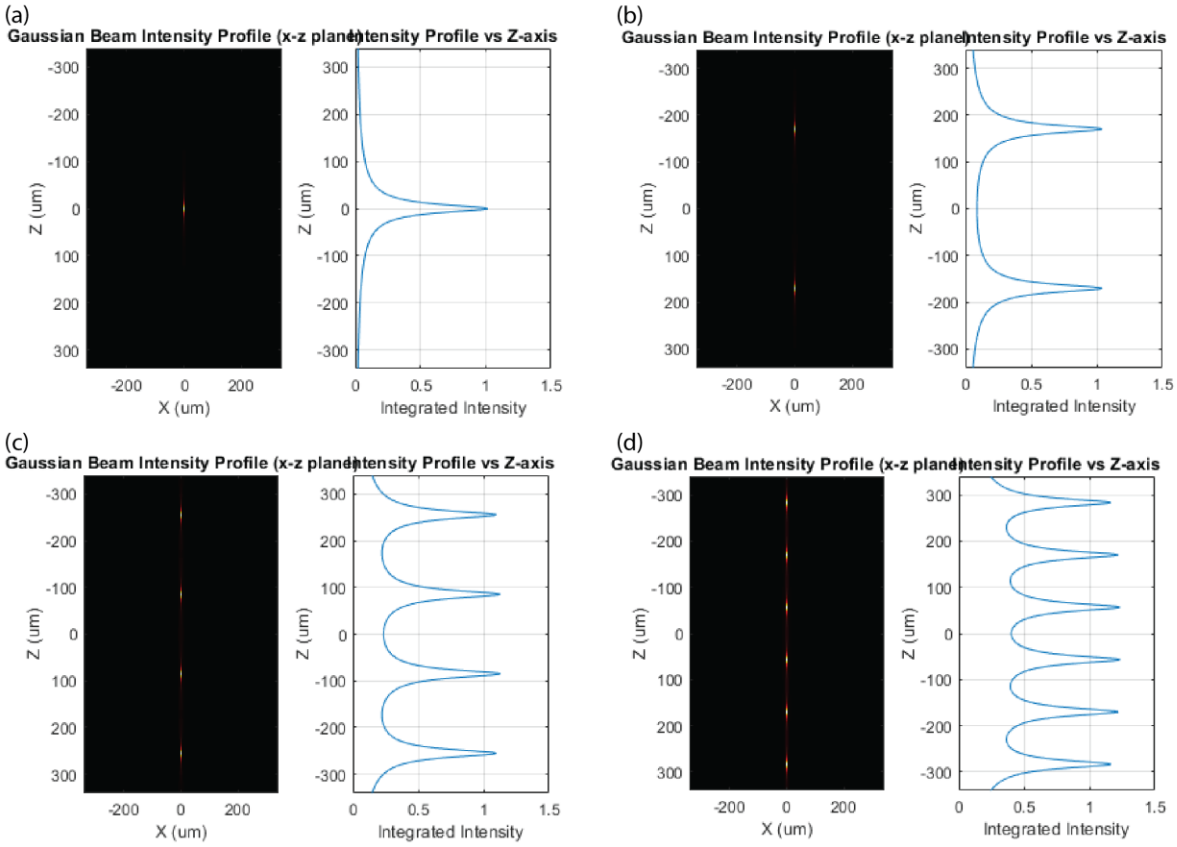

Figure 3.11. Multi-foci light sheet in FOV. Modeling of evenly distributed foci within the Field of View (FOV), showcasing the beam profile along the Z-axis for one, two, four, and six foci.

Because we used a combination of concave and convex lenses to control the axial separation of the light sheets, the focal lengths and the effective magnification for the two states of polarization in the illumination arm changed slightly which not only made synchronizing the rolling shutter in two FOVs challenging, but also resulted in resolution-loss. Although we found this arrangement adequate and acceptable, in terms of the overall performance, several alternative schemes could

make the light sheet separation control easier. For example, by using a step or a tilted mirror in the remote focusing arm [104] or binary SLM to generate tiled discontinuous light sheets [100] or, pLSFM scheme [111] axially staggered light sheets may be generated to carry out our scheme. We found that more precise control over the light sheet positions could translate into faster imaging speed. As such at its current settings we could triple the speed of imaging (data not shown here) with 95% FOV coverage. Our future implementations will investigate these options to push the limits of ASLM even further.

3.5. Summary

In summary, we have demonstrated a new scheme whereby axially scanning two simultaneous light sheets improved the overall performance of ASLM both in terms of imaging speed and detected signal. We achieve this by splitting the sCMOS' FOV into two and then running synchronized sub-array readout in the two halves independently. This enabled us to image a cleared mouse brain across a large FOV (670×670 μm^2) with twice the frame rate (20 frames/sec) compared to the original ctASLM (10 frames/sec) at this FOV. Also, for a particular frame rate, compared to conventional ASLM, our concept illuminates the sample for twice the dwell time, doubling the signal intensity as evaluated by SNR. Additionally, because this new technique is developed upon the general ctASLM design, with several key innovations, it retains ctASLM' s most salient feature *i.e.* multicolor imaging across the entire refractive index range with diffraction-limited isotropic resolution. We, therefore, believe that our version of ASLM brings

about the most advanced light sheet microscope that there is for large-volume 3D imaging of tissues.

Chapter 4: Axial De-Scanning through Pupil-Matched Remote Focusing in the Detection Arm of Light-Sheet Microscopy

4.1. Introduction

The ability to image at high speeds is necessary in biological imaging to capture fast-moving or transient events or to efficiently image large samples. However, due to the lack of rigidity of biological specimens, carrying out fast, high-resolution volumetric imaging without moving and agitating the sample has been a challenging problem. Pupil-matched remote focusing has been promising for high NA imaging systems with their low aberrations and wavelength independence, making it suitable for multicolor imaging. However, owing to the incoherent and unpolarized nature of the fluorescence signal, manipulating this emission light through remote focusing is challenging. Therefore, remote focusing has been primarily limited to the illumination arm**,** using polarized laser light for facilitating coupling in and out of the remote focusing optics. Here we introduce a novel optical design that can de-scan the axial focus movement in the detection arm of a microscope. Our method splits the fluorescence signal into S and P-polarized light and lets them pass through the remote focusing module separately and combines them with the camera. This allows us to use only one focusing element to perform aberration-free, multi-color, volumetric imaging without (a) compromising the fluorescent signal and (b) needing to perform sample/detection-objective translation. We demonstrate the capabilities of this scheme by acquiring fast dual-color 4D (3D space + time) image stacks, with an axial range of 70 µm and camera limited acquisition speed. Owing to its general nature, we believe this technique will find

its application to many other microscopy techniques that currently use an adjustable Z-stage to carry out volumetric imaging such as confocal, 2-photon, and light sheet variants.

4.1.1 Limitations of Traditional Axial Scanning Techniques in BioPhotonics

Fast 3D positioning or scanning of an optical system's focal point or focal plane has the potential to transform many areas of BioPhotonics, especially those that require studying the complex dynamics of living organisms. Processes like investigation of neuronal activities of the brain, blood flow in the heart, and cell signaling require high-speed volumetric imaging[112–114]. However, volumetric imaging requires an axial scan either through the translation of the sample or the detection objective lens (Fig. 4.5a). Such axial translations result in imaging modalities that are often slow with speeds limited to a few hundred Hz[115–117]. Additionally, with fragile samples, such as an expanded sample in hydrogel[118], fast movements of the sample stage may agitate the sample and induce distortions when collecting volumetric images.

To avoid the slow translation of bulky objectives or the sample stages, several attempts, employing variable-focus (vari-focus) lenses, mechanical mirrors, and acousto-optics modulators have been proposed to refocus the light for 3D imaging. However, they all suffer from unacceptable aberrations introduced by the focusing elements. A large category of those techniques utilize different types of tunable lenses such as ferroelectric liquid crystal (LC), acoustic waves (TAG lens), and acoustic optics modulators (AOM)[119] to achieve fast focal shifts

(~1kHz). Ferroelectric LC and TAG lenses introduce a focal shift by varying the gradient of the refractive index of the liquid medium, however, the generated phase variation only approximates the defocus phase, leading to increased spherical aberration at large focal shifts[61,120,121]. AOM-based vari-focus techniques on the other hand use two AOMs with counterpropagating acoustic waves to cancel out the transverse scan but can only achieve focus shift in one dimension (acting as a cylindrical lens)[122,123].

4.1.2 The Role of Adaptive Optics in Overcoming Vari-Focus Limitations

Adaptive optics-based vari-focus techniques overcome these limitations through accurate wavefront control using either a spatial light modulator (SLM) or a deformable mirror (DM), which can achieve a response rate of ~1 kHz and 20 kHz respectively. However, SLMs are polarization and wavelength-dependent and cannot model a continuous wavefront of the defocus phase due to its limited phase modulation depth. Large phase shifts are generated through multiple phase-wrapping of 2π. With finite fly-back at the phase-wrapping borders, part of the incident light is not correctly modulated and results in decreased intensity at the focus[124]. DMs are not polarization and wavelength-dependent and can model a continuous defocus wavefront. However, the axial scan range of a DM is limited by the stroke length of the DM actuators. For example, for an objective with a numerical aperture (NA) of 0.8, the maximum axial scan range that DM based techniques can generate is ~40 μm[70]. Furthermore, using DM for focus control requires accurate alignment and complicated calibration of the DM to reduce the aberrations caused by imaging samples out of the nominal focal plane of the objective[120].

4.1.3 Limitations of pmRF Techniques in Detection Path of Fluorescence Microscopy

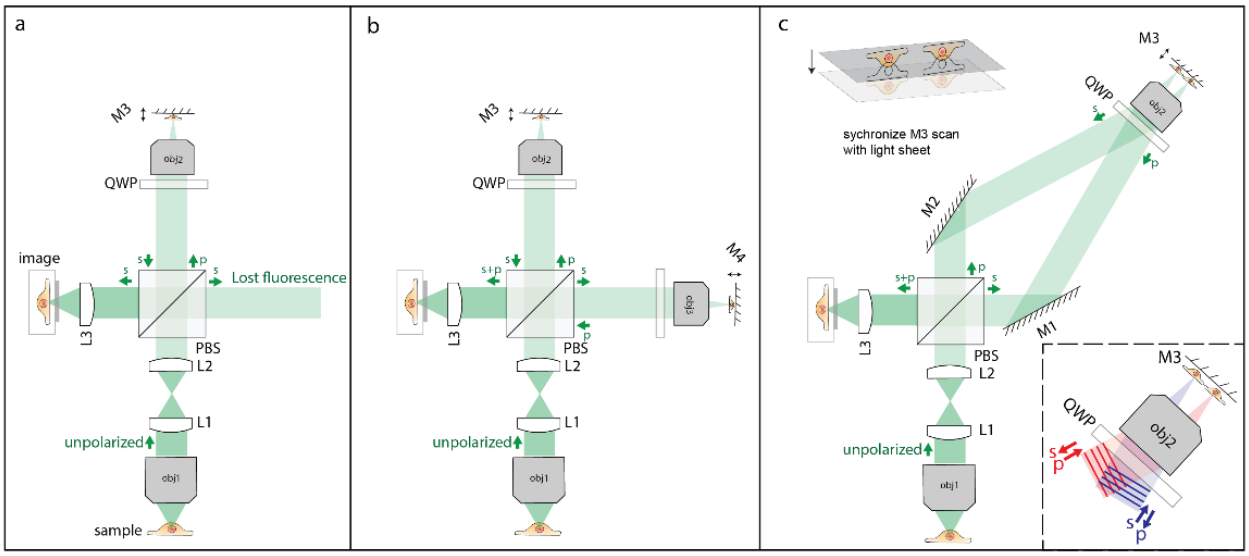

Figure 4.1. Three different pmRF modalities in the detection path of the microscope. a) In a conventional pmRF system, due to the unpolarized nature of the fluorescent light only one polarization state is imaged by the camera and another one is lost. b) By using two LFAs in both arms, the camera can capture both polarization states. This modality is costly and complicated which requires synchronization between two LFAs. c) In our proposed pmRF system, only one LFA is capable of *Z*-scanning for both polarization states without losing any fluorescent light. The inset shows how two incoming-polarized light changes their polarization states after reflection from the mirror M3.

Unlike the adaptive optics or DM-based approaches that require correcting the defocus plane-by-plane, pupil-matched remote focusing (pmRF), pioneered by Botcherby et al.[73,105], instantaneously corrects defocus across 3D volumes for high-NA optics thereby conserving the microscope's temporal bandwidth[73,102,105,125–132]. In addition, because pmRF allows precise mapping of the wavefront coupled into the back-pupil of the objective, where the angular magnification is unity, such techniques have been routinely used to carry out aberration-free high-quality axial focus control[73,102,105,125–132]. In pmRF techniques, a fast axial scan is achieved by the translation of a small mirror in front of the remote objective using a focus actuator[102,125,129] or by a lateral scan of a galvo mirror in combination to a step or tilted

mirror at the remote objective[104]. Because of the fast response time of the focus actuator or the galvo mirror, an axial scan rate of 1-5 kHz or 12 kHz can be achieved respectively. However, current pmRF techniques for focus control are primarily limited to the illumination path. This is because pmRF uses the concept of optical isolators[133], where the polarization of the returning beam is rotated orthogonally to the incoming beam so that it can be separated from the incoming beam at the polarized beam splitter (PBS) (Fig. 4.1a). *This configuration ensures minimum light loss through the pmRF module but requires the incoming beam to be polarized, which is why this method is primarily used in the illumination arm where illumination laser light is usually polarized in nature and its manipulation through the optical isolator can be easily done.* In the detection arm, however, the emitted fluorescence is unpolarized in nature. To the best of our knowledge, because, using purely linear optical elements, lossless conversion of unpolarized light into a single polarized state is not yet possible [134,135] (Supplementary Note 1), manipulating the fluorescent light using the optical isolators is unfeasible. As a result, microscopes that use pmRF to carry out axial scanning, incur 50% light loss due to one state of the polarized light being discarded after the PBS[73,127,130] (Fig. 4.1a).

A straightforward method to mitigate this problem is to have another copy of the pmRF module at the unused port of the PBS (Fig. 4.1b) to collect the other half of the fluorescent light. However, this would require precise synchronization of two linear-focus-actuators (LFA), which is not only a difficult task at high speeds but also will be expensive since this method warrants two such LFAs. In this article, we present a novel optical design that overcomes these problems and presents a modular setup that can perform remote focusing on the detection arm of a fluorescent microscope without incurring polarization-induced losses. When attached to a light-sheet

microscope, this technique allows optical refocusing without requiring the movement of the sample, or the detection objective (Fig. 4.5b and Fig. 4.1c). As a result the microscope can acquire 3D volumetric data limited by camera speed. This technique is applicable to many other microscopy techniques that currently use an adjustable *Z*-stage to carry out volumetric imaging such as confocal, 2-photon, and light sheet variants.

4.2 Method

4.2.1 Design and Working Principle of the Axial-Refocusing Unit

***Optical axial-refocusing*:** Our refocusing unit is shown in Fig. 4.5b. Here, the water immersion detection objective (Obj1) is pupil matched to a second air objective (Obj2) through two intermediate lenses following the original design by Botcheherby et al.**[73,105]**. However, unlike traditional refocusing geometry, we split the collected unpolarized fluorescence into S and P-polarized light using a polarizing beam splitter cube (PBS) in the infinity space of Obj2. The generated orthogonal paths are then projected onto Obj2 using two angled mirrors M1 and M2. Because of this angular launch in infinity space, Obj2 forms two distinct laterally shifted images at its nominal focal plane. A small mirror placed on an LFA reflects the light back through the path it came from where a quarter wave plate (QWP) converts the S-polarized light to P on its way back (and P-polarized light to S) after being reflected from the mirror (Fig. 4.5c). When the returning light (in each arm) reaches the PBS, it now acts as an optical valve where the S path (which was initially P) gets reflected while the P-polarized light (which was initially S) gets

transmitted by the PBS. As a result, both S and P polarized light exits the PBS through the fourth and unused face of the PBS cube (Fig. 4.5d). This light after passing through a tube lens forms identical images, one with S and another with P, at the sCMOS camera. *A precise alignment using mirrors M1 and M2 overlays the two images, thereby resulting in a combined image by simply an incoherent addition without any interference artifacts.*

There are a few important design considerations that need to be considered for our de-scanning setup. Firstly, it is essential that mirror M3 consistently moves in parallel with the focal plane of Obj2 during the LFA's oscillatory motion. This prevents any unwanted focal shifts between the S and P paths, ensuring that the resulting image from both S and P polarizations remain focused on the camera at the same time. This arrangement ensures that both beams return through their incoming paths, resulting in easier alignment for overlaying the final images formed by the S and P-polarized beams.

Secondly, it is advantageous that θ (angle between S and P polarized beam hitting the Obj2) (*Fig. 4.2*) be as small as possible because this directly controls the distance between the two focal points at M3 (depicted by ΔL in Fig. 4.5c). A smaller ΔL ensures: (1) a smaller mirror could be utilized to carry out the remote-focusing, reducing the inertial load on the LFA, and enhancing its efficiency; (2) The alignment becomes less sensitive to tip-tilt misalignment of M3; and (3) This guarantees that both images fit within Obj2's field of view (FOV).

Thirdly, there exists an inverse relationship between the angle θ and the distance between Obj2 and the PBS (inset of Fig.4.2). Therefore, this gives us an option: *either adhere to the 4f system or minimize ϑ*. We found that for our matching objectives Obj1 and Obj2 the 4f system (with

matching lenses L1 and L2) resulted in a θ of 20^{o} (inset of Fig.4.2). However, operating in this range poses a risk as it is challenging to ensure that both reflected beams are entirely captured by Obj2. Hence, there is a balance between adhering to the 4f system and minimizing the angle θ. We found that with our current design, we can still achieve diffraction limited resolution (Fig.4. 5e).

Finally, because we generated two identical images on the camera using S and P-polarized light, it was crucial to overlay these images with precision higher than the diffraction-limited resolution to produce the final image. To do this, we developed a cross-correlation-based algorithm that quantifies the shift between overlayed S and P images in real-time with sub-pixel accuracy, allowing interactive adjustment of the mirrors M1 and M2 during system alignment.

4.2.2 Implementation of Axial-Refocusing Unit in a Light-Sheet System

In order to test the performance of our design we implemented this setup into the detection arm of a light-sheet microscope with orthogonal illumination and detection objectives. The system layout is shown in (Fig.4.5b and Fig.4.2). The sample is illuminated by a sheet of light generated with a cylindrical lens in the illumination arm, and the emitted fluorescence from the sample is collected by the detection objective lens, which is set orthogonal to the illumination objective lens to capture 2D information from the sample. A galvanometric scan mirror (GSM) in the illumination arm translates the light-sheet in the *Z*-direction. Because the position of the LFA in the detection arm determines the focal plane of the detection objective lens, we synchronized

the GSM and LFA with the sawtooth signal to ensure that the detection path is always focused on the plane of the light-sheet (Fig.4.3). This allowed us to carry out volumetric imaging by acquiring a sequence of images from different focal planes. The LFA moves back and forth rapidly, synchronized with the movement of the GSM enabling us to quickly collect 3D image stacks.

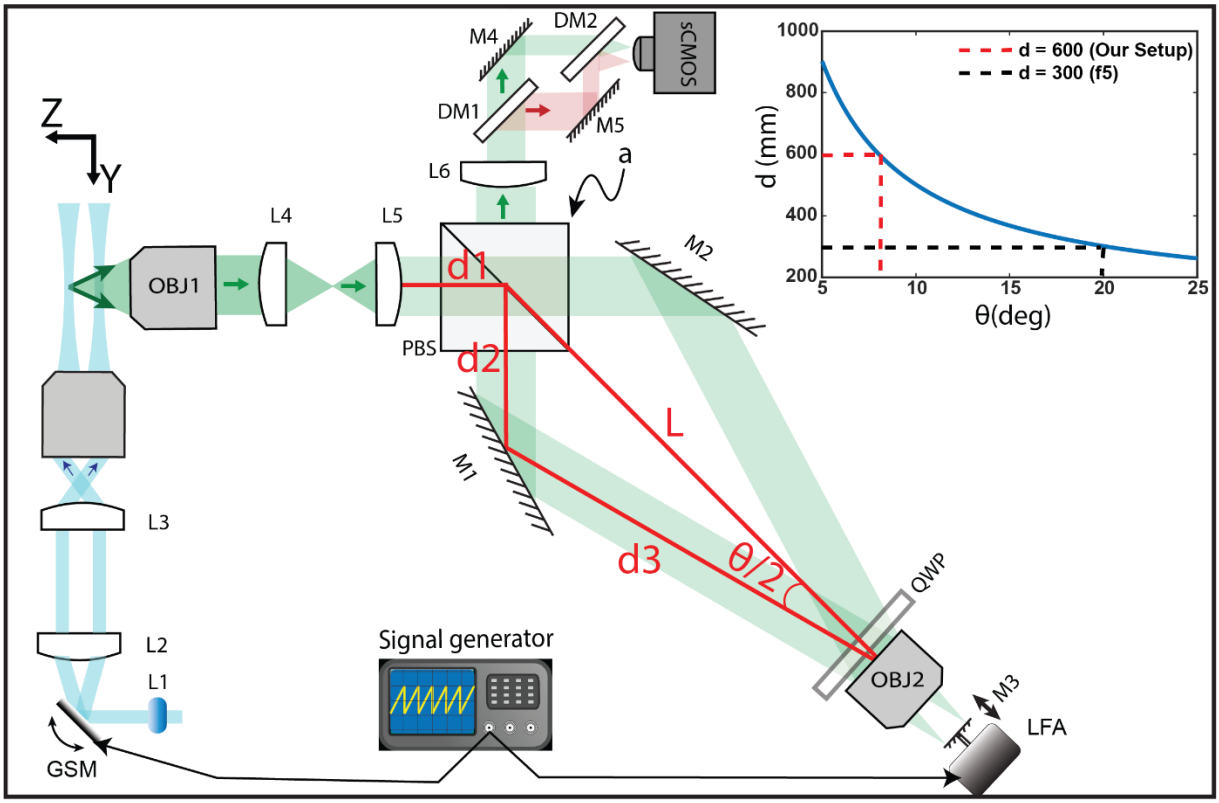

Figure 4.2. implementation of the pmRF into the detection path of the light sheet microscopy. In the illumination arm, the light sheet generated by the cylindrical lens is translated in the *Z*-direction by the GSM. The fluorescent light is captured through the proposed pmRF system. The GSM is synchronized with the LFA to ensure that the camera images the emitted fluorescence from the plane where the translated light sheet excites the specimen. Two Dichroic mirrors (DM1 and DM2) separate the FOV into half to obtain simultaneous dual color imaging with 637 nm and 488 nm laser excitations. The separation between the two foci reduces by reducing the θ (angle of the incident beam onto the OBJ 2. In inset, d = d1+d2+d3, the plot shows the relationship between the d and θ.

The optical correction of defocus in our high-NA microscope allowed fast de-scanning of a 3D volume over an axial range of ~70 µm at speeds limited primarily by the camera framerate (~in our case 799 camera frames/s at 2304 ×256 pixels using Hamamatsu Orca-fusion BT). We employed a dual-color imaging strategy by partitioning the FOV, enabling simultaneous capture of two distinct fluorescent labels within each slice without sacrificing imaging speed. To do this we used a pair of dichroic mirrors to separate the emitted wavelengths from the two labels into side-by-side dual-color images (Fig.4.2). Once acquired, these separate image sets are then precisely registered and merged to generate 4D (*X, Y, Z,* and *λ*) stacks. By sequentially capturing 4D stacks, we generated 5D (X, Y, Z, λ, and time) datasets that allowed us to track the dynamic behavior of biological processes. It is important to note that our setup is wavelength-independent, an attribute not feasible with technologies like diffractive tunable lenses or spatial light modulators.

4.2.3 The Role and Synchronization of the LFA and GSM in Light Sheet Microscopy

In our light sheet microscopy setup, the Galvo-Scanning Mirror (GSM) controls the translation of the light sheet along the detection arm, while the Linear Focus Actuator (LFA) determines the focal plane within the sample space. To acquire a 3D image stack of a sample, the system captures images plane-by-plane. This is achieved by translating the light sheet through the sample using the GSM and focusing each 2D image onto the camera using the LFA. To ensure precise focusing in Z-scan mode, it's crucial to synchronize the LFA and GSM. This is accomplished by first applying

specific voltages to the GSM. Subsequently, focused images are obtained on the camera by applying corresponding voltages to the LFA in static mode. For calibration, 200 nm beads embedded in a 2% agarose gel are used. When operating in Z-scan mode, the LFA oscillates rapidly but remains in sync with the GSM, owing to this calibration process. Figure 4.3 illustrates the relationship between the voltages applied to the LFA and GSM, revealing a relatively linear correlation between the two.

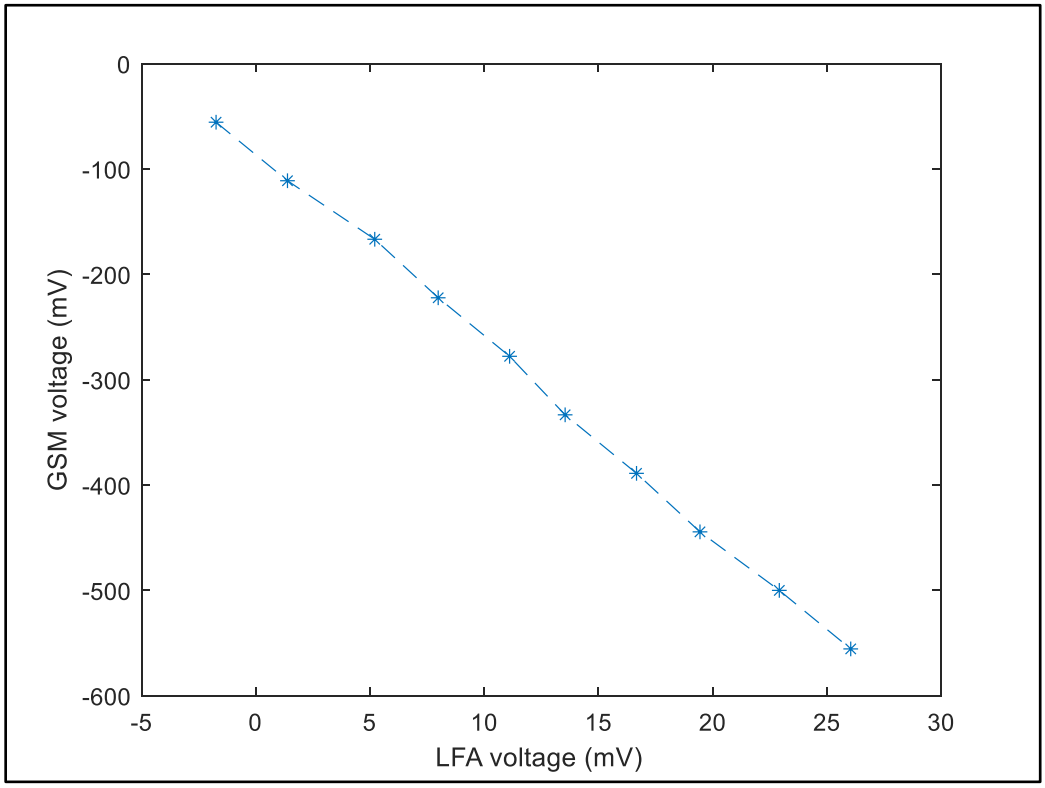

Figure 4.3. voltage synchronization of the LFA and GSM. The relatively linear relationship between applied voltages to the GSM and LFA is needed to acquire a 3D stack of the sample by imaging plane by plane in the axial direction.

4.2.4 Overlaying S and P images with sub-pixel accuracy

Two identical images -- one corresponding to S and another to P polarized light -- are formed at the camera and added incoherently to generate the final image. We used a custom-written MATLAB script to monitor the offset between the two images in near real-time while adjusting the positions of M1 and M2 (Fig.4.4).

The offset between the two images using a cross-correlation-based algorithm as was used in Wester, M.J. et al[136], which achieves sub-pixel accuracy by fitting second-order polynomials through the peak of the scaled cross-correlation between the S and P polarized images.

Initially, an image is acquired as a reference by obstructing one optical path (either S or P). Subsequently, the alternative optical path is used to collect new images. The shift between each new image and the reference image is then measured using the method described in Wester, M.J. et al[136] and is available as the MIC_Reg3DTrans.findStackOffset method in the matlab-instrument-control toolbox[137]. And while new images are collecting, mirrors M1 and M2 are adjusted to minimize the shift.

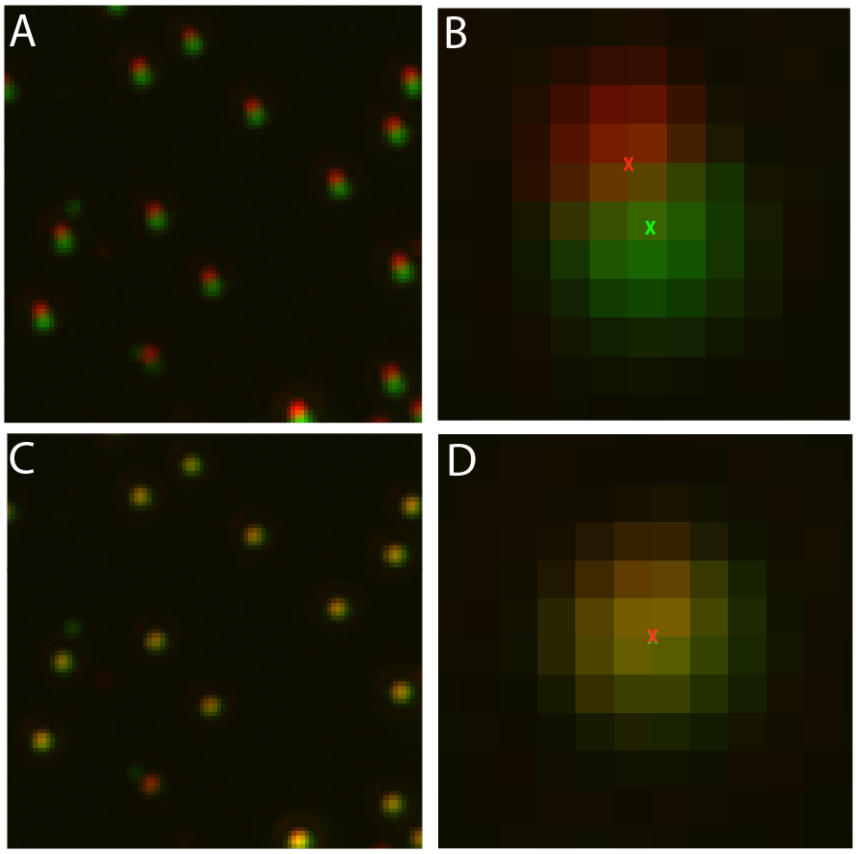

Figure 4.4. Fine optical alignment of the S and P polarized images. The fine optical alignment of the system is performed using 200 nm beads embedded in 2% agarose gel. The green and red beads are S and P polarized images respectively. A, B) In the initial setup, the S and P-polarized images are a few pixels away. C, D) The fine alignment is performed using MATLAB script and positioning mirrors M1 and M2 interactively (Fig. 4.5b). At the final image, both S and P images are overlayed on each other in subpixel accuracy.

4.2.5 Optical setup

The illumination arm consists of two laser sources (Coherent Sapphire 488 nm and Obis LX 637 nm) which were combined with a dichroic beam splitter (LM01-503-25, Semrock). To clean up the beams, the beams were focused through a 50-µm pinhole (P50D, Thorlabs) by a 45-mm achromatic doublet (AC254-045-A, Thorlabs) and then recollimated using a 150-mm achromatic doublet (AC254-150-A-ML, Thorlabs). The original beams were expanded by 9 folds with a 3×

Galilean beam expander (GBE03-A) before being focused with a cylindrical lens (ACY254-50-A, Thorlabs), onto a resonant mirror galvanometer (CRS 4 kHz, Cambridge Technology), driven by a 12-volt power supply (A12MT400, Acopian), to wobble the light sheet. One-dimensional focus was then recollimated with a 100-mm achromatic doublet (AC254-100-A-ML, Thorlabs) and hit the galvanometric scan mirror (GSM) (GVS111, Thorlabs), driven by a 15-volt power supply (GPS011, Thorlabs), for rapid shifting of the light sheet along the detection arm. This galvanometric mirror was conjugated to the back pupil of the objective lens (Nikon 40x/0.8 NA) through 100-mm and 200-mm achromatic doublet (AC508-100-A-ML and AC508-200-A-ML, Thorlabs).

In the detection arm, the same objective lens (Nikon 40x/0.8 NA) in an orthogonal setup was used and pupil-matched to the scanning objective lens (Nikon Plan Apo 20x/0.75 NA) through a 200-mm tube lens (TTL200-A, Thorlabs) and a 300-mm achromatic doublet (AC508-300-A-ML, Thorlabs). A 50:50 polarizing beam splitter (PBS) (10FC16PB.3, Newport), splits the beam in S and P polarized light. Using mirrors M1 and M2 these light paths where then launched at an angle towards the Obj2 (Fig.4.2). It is extremely critical to minimize the angle of the launch. Both experiment and simulation predicted that we used 8 degrees as the launch angle (called θ) (Fig.4.6a, inset of Fig.4.2). The S and P polarized light passed through a quarter waveplate (AQWP10M, Thorlabs) and were focused onto a mirror positioned at the focus of the scanning objective lens. The mirror (PF03-03-P01 - Ø7.0 mm Protected Silver Mirror, Thorlabs) was attached to a voice coil with a travel of 10 mm, positional repeatability of fewer than 50 nanometers, and a response time of fewer than 3 milliseconds (LFA-2010, Equipment Solutions). Then the reflected light was recaptured by the same scanning objective lens and quarter-wave

plate to rotate the beam's polarization state. Afterward, the light was directed toward an sCMOS camera (Hamamatsu Orca-fusion BT) by reflecting from the same cube polarizing beam splitter and a 300-mm achromatic doublet (AC508-300-A-ML, Thorlabs). For emission filters, we used two long-pass filters (FF01-525/30-25, and BLP01-647R-25, Semrock), for blue, and far-red, respectively. To image dual channels simultaneously, the field of view (FOV) was separated into half using dichroic mirrors (DMLP605R, Thorlabs) between the 300-mm achromatic doublet and the camera. We immersed the specimen and the illumination and detection objectives in a chamber designed using Adobe Inventor and machined through Protolabs (R). The LFA and GSM, in the detection and illumination arms respectively, were synchronized together to always keep the translated light sheet in the focus of the detection objective lens to acquire a 3D stack of the specimen.

4.2.6 Microscope control

A Dell Precision 7920 computer with two processors Intel(R) Xenon(R) Silver 4210R CPU having a processing speed of 2.40 GHz and 2.39 GHz and was integrated with 128 GB RAM was used to acquire the microscope's data. An NVIDIA Quadro RTX 4000 Graphics processing unit (GPU) with dedicated memory of 8 GB and shared memory of 63.8 GB (GPU memory of 71.8 GB) was also integrated into the system. 64-bit operating system ×64-based processor facilities the system to operate. LabView 2020 64-bit allowed us to work with the required software, including the LabView Run-Time Engine, Vision Run-Time Module, Vision Development Module, and other

required drivers like NI-RIO drivers (National Instruments). DCAM-API software was used for the Active Silicon Firebird frame-grabber to actively interfere with the scientific complementary metal-oxide semiconductor (sCMOS) camera (ORCA-Fusion BT Digital CMOS camera, model: C15440-20UP) manufactured by Hamamatsu, Japan. It generated deterministic transistor logic (TTL) trigger sequences through 150 Watts shutter instrument (100-240 V~50/60 Hz; model: MP-285A) with a field programmable gate array (FPGA) (PCIe 7852R, National Instruments). The generated triggers controlled the resonant mirror galvanometers, placement of the stage, voice coils, blanking and modulation of laser, firing camera, and other external triggers. K-Hyper Terminal software facilitated engaging LFA with the system hardware. Some key features along with some routines under the agreement of material transfer were licensed by the Howard Hughes Medical Institute's Janelia Farms Research Campus.

4.3 Results

4.3.1 Quantification of Resolution in the Axial Re-Focusing Module

To quantify the performance of the proposed scheme, we used full width at half max (FWHM) measurements of 3D point spread function (PSF) to validate that the incoherent addition of S and P images was not compromising the resolution. To do this, we measured the PSF of each polarization component individually and compared it with the PSF of the unified S+P image. As illustrated in Fig.4.5e, both the S and P-polarized images rendered onto the camera exhibit

identical FHWM, resulting in an equivalent resolution for the combined S+P image. Further quantification involving 10 randomly chosen beads, reveals that the microscope achieved diffraction-limited resolutions: 394±31 nm laterally (*X*-*Y*) and 654±130 nm axially (*Z*). These measurements were performed in proximity to the nominal focal plane (MIP of 10 slices, each separated 500 nm).

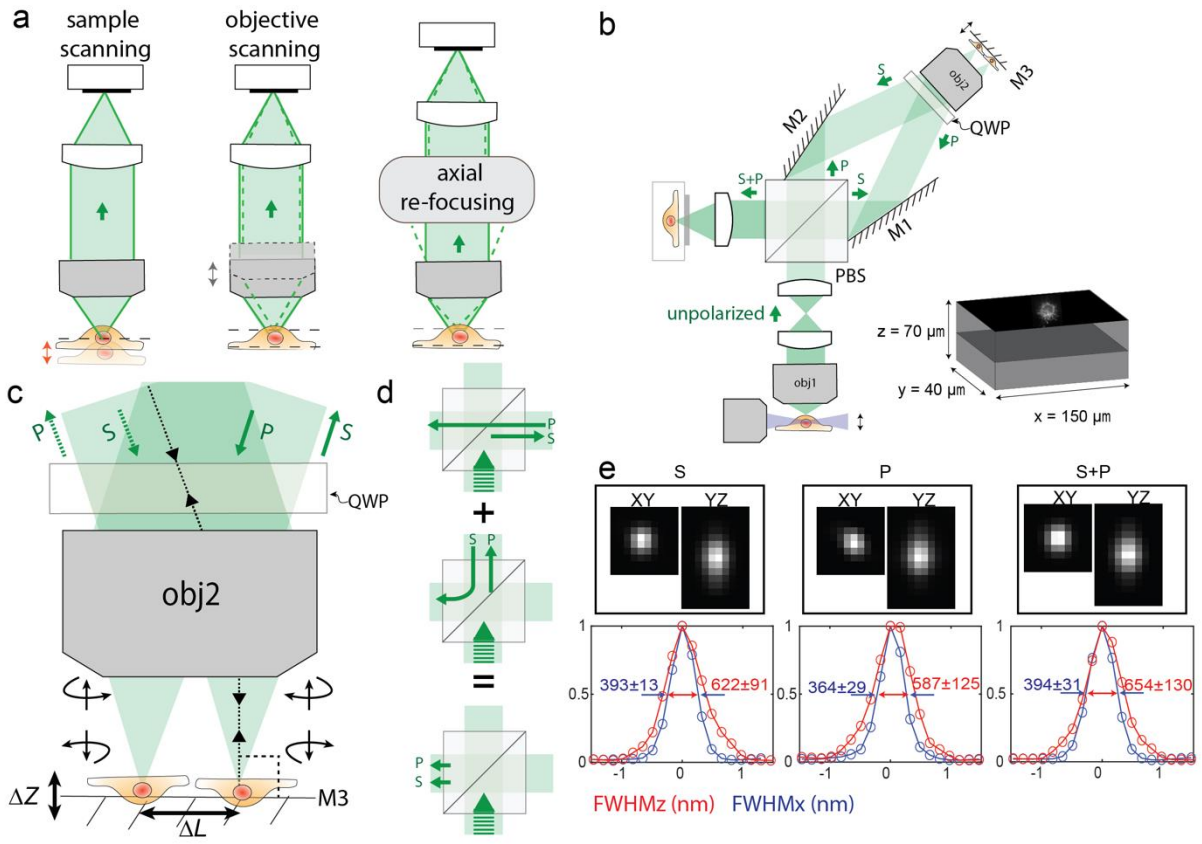

Figure 4.5. Schematic diagram of a remote focusing system implemented in light-sheet microscopy and its performance. a) Three different modalities to acquire volumetric imaging of the sample along the focus direction. Either the sample or objective lens can be moved for axial re-focusing. Alternatively, both the sample and objective lens can remain stationary by using a remote focusing system. b) Implementation of the remote-focusing system on the detection arm of the light sheet microscope. In this configuration, objective lenses 1 and 2 are pupil-matched through two lenses to form a perfect imaging system. Combined with mirror M3 and a polarizing beam splitter (PBS), the whole system works as a remote focusing system. The novel design of this remote-focusing system is implementation in the detection arm for unpolarized fluorescent light emitted from the sample. To do this, two tilted mirrors M1 and M2 are utilized to direct both S and P-polarized beams toward Objective lens 2 and then combine the reflected beams from mirror M3 to create an image by S and P-polarized beams onto the camera by focusing through the tube lens. The mirror M3 is attached to the linear focus actuator (LFA), moving back and forth to scan the sample in the *Z*-direction to acquire a 3D image. In the illumination arm, the generated light sheet by a cylindrical lens is translated by a galvanometric scan mirror (GSM) along the detection arm. To focus the detection path on the plane of the light sheet, the synchronization of GSM and LFA is carried out by sawtooth signals. Simultaneous dual-channel imaging of the cell is achieved in 40 µm×150 µm FOV over 70 µm in the *Z*-direction. c) The polarization state of the incoming beams changes after reflection from mirror M3 (S to P, and P to S). d) The reflected beams from mirror M3 have a different polarization state compared to the incoming beams; therefore, they exist from a different side of the PBS than the incoming beams. e) The point spread function (PSF) of 200 nm beads formed by S, P, and S+P polarized beams. The microscope performs at the diffraction limit, 394 nm resolution, for S, P, and S+P in the lateral directions (*X-Y*), while it maintains a resolution of 654 nm in the axial direction (*Z*).

To evaluate the performance of the de-scanning system, we imaged 3D volumes of 200 nm beads

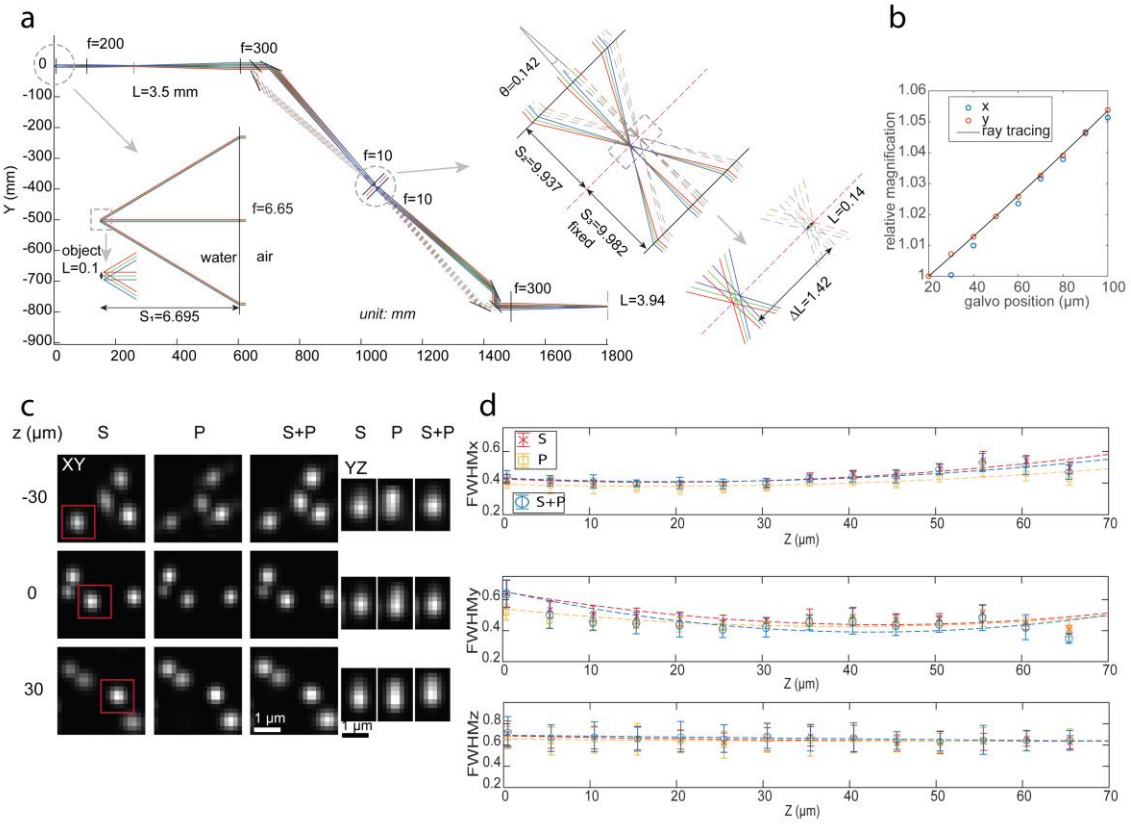

Figure 4.6. Ray tracing of the setup and resolution assessment. a) Ray tracing of the detection path. L: image size, f: effective focal length, S: image or object position relative to the lens, unit: mm. b) Calibration of lateral magnification at various object positions, a target illuminated by a white light LED is imaged for magnification measurement. c) Maximum intensity projections of data acquired on 200 nm beads from 10 slices spaced 500 nm in the *Z*-direction. The images show orthogonal views of the MIPs across scan range for S,P and S+P. The elongated PSF in the *Z* direction exhibits less resolution in the axial direction controlled by the light sheet waist. d) The FWHM of the 200 nm beads in the lateral and axial directions over the scan range. The minimum lateral resolution, 394 nm, occurs at the center of the scan range and increases by moving away from the center. These plots show a constant axial resolution of 650 nm over the axial scan range. The microscope functions in the scan range of 70 µm.

embedded in a 2 % agarose cube across the scan range and accessed the quality of the generated PSFs. Fig. 4.6c shows the maximum intensity projection (MIP) of beads (from 10 axial slices, each slice spaced 500 nm) separated by 30 µm for S, P, and S+P across the scan range, after 10 iterations of Richardson-Lucy (RL) deconvolution. We found that our remote focusing setup demonstrated close to diffraction-limited performance over a scan range of ~70 um. As evident

from the ‘S’ and ‘P’ images the quality of the beads visually appears similar across the entire scan range thereby resulting in an identical ‘S+P’ image. In the axial direction (the YZ view) the PSFs are limited by the Gaussian light sheet’s waist (beads from red boxes in XY view), which was determined by the tradeoff that exists between the FOV and Z resolution. We found that in order to image an entire cell, we needed a lightsheet that would generate a FOV of ~8 μm (Fig. 4.9). As a result, we reduced the NA of the illumination objective and chose a light sheet whose waist was at FWHMz of ~ 650 nm after deconvolution (850 nm before deconvolution).

Figure 4.6d displays the measured FWHMs from 200 nm beads after RL deconvolution for S, P, and S+P polarize images in the lateral (*XY*) and axial (*Z*) directions across the entire scan range. The figure shows a minimum lateral FWHM of 394 nm at the center of the scan range which slowly increases as the beads move away from the nominal focal plane. This can be attributed to residue index mismatch aberrations that were not corrected by the remote focusing system[127]. Additionally, we found that the S polarization path suffered more in lateral resolution compared to the P polarization path and the trend is different along *X* and *Y* directions. This asymmetric FWHMs (*X*-*Y*) across scan range (*Z*) and the discrepancy between S and P paths is likely due to field-dependent aberrations from Obj2, where the S and P images were formed at different field points of Obj2 (Fig. 4.5b). Furthermore, our microscope shows a constant axial FWHM of ~ 650 nm over the entire scan range as the axial resolution is mainly determined by the light-sheet waist.

4.3.2 Magnification of the Axial-Refocusing System

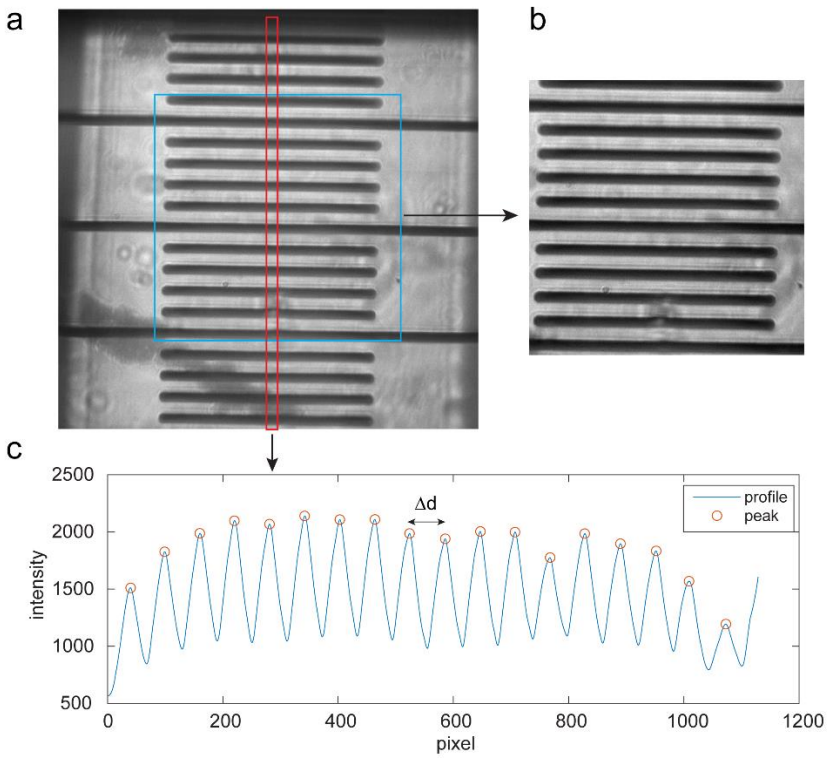

Figure 4.7. Quantification of microscope magnification. (a) bright field image of a calibration target at the center of the scan range. (b) the cropped region from the blue box in a, which is used for estimating relative magnification (Fig.4. 6). (c) smoothed intensity profile of the cropped region (red box in a), averaged separation of consecutive peaks (red circle) is used for estimating the absolute magnification (Methods).

One brightfield image of the calibration target was captured at each of the galvo positions from -40 to 40 µm with a step size of 10 µm. The target image consisted of parallel line segments; we cropped a region of 700x700 pixels from each image (Fig.4.7a-b). We then calculated the affine transformation (from the Dipimage toolbox) of each image with respect to a reference image. The zoom factors from affine transformation were used to quantify the relative magnification between each image to the reference image. The absolute magnification of one image was

calculated as follows: crop a narrow section of multiple parallel lines, obtain the intensity profile by averaging over the line dimension, smooth the intensity profile by applying a running average with a window size of 30 pixels, find all peaks from the smoothed intensity profile (Fig.4.7c), calculate the average distance (in pixels, denoted as Δd) between consecutive peaks, as the distance between consecutive parallel lines is 10 mm, then the pixel size at the sample plane can be estimated from $10/\Delta d$ mm, therefore the magnification can be calculated from the pixel size of the camera divided by pixel size at the sample plane.

4.3.3 Light-Sheet Dimension Analysis

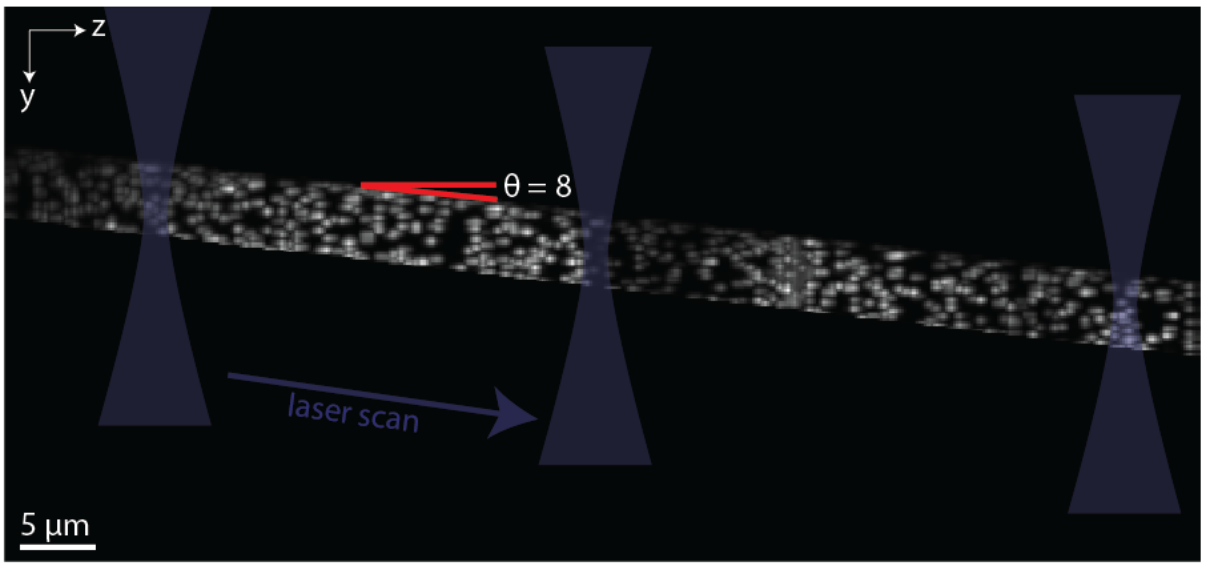

Figure 4.8. *YZ* view of MIP of stacks of 200 nm beads. The light sheet translates in *Y* while scanned in *Z* direction. The angle between the light sheet translation and the *Z*-axis is 8 degrees. The beads are RL deconvolved and only the beads in the light sheet waist region are cropped and shown here.

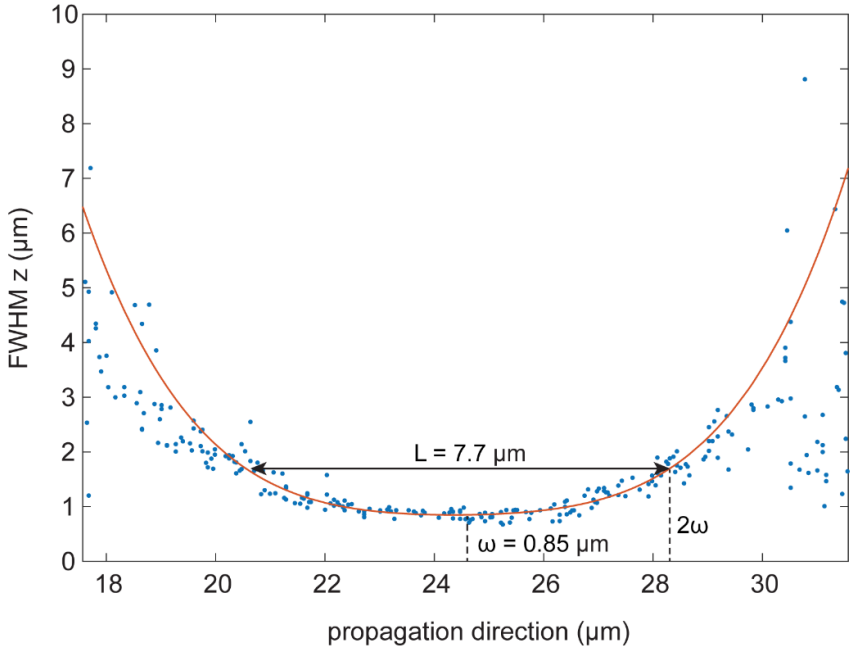

Figure 4.9. Quantification of light-sheet dimensions on raw data (before deconvolution). FWHM along the scanning direction (FWHMz) is estimated by imaging 200 nm beads (Methods). FWHMz (measured from multiple beads, blue dots) versus the light sheet propagation direction is fitted by a 4th order polynomial (red line). The minimum of FHWMz (ω) is 850 nm, and the length of the light sheet (L) is 7.7 μm when FWHMz=2ω.

To quantify the light-sheet dimension, bead data in agarose gel were collected at different slit widths. At each slit width, we estimated the FWHMs in *XYZ* for all selected beads as described above, however, here we used the full FOV of the color channel for bead imaging. As the position of the light-sheet waist shifted in y with respect to the axial dimension, we corrected the y coordinates of the selected bead by $y'_{cor} = y_{cor} - az_{cor}$, where a is the y shift by moving one pixel in *Z* (Fig.4.8). Then we fitted the $FWHM_z$ verse y'_{cor} for all selected beads with a polynomial function (Fig.4.9). The length of the light-sheet was found when the $FWHM_z$ was twice the minimum from the polynomial fit.

4.3.4 Investigating Intensity Distribution of S, P, and S+P Polarized Light in Axial Scanning

To investigate the intensity distribution along the *Z*-direction for S, P, and S+P polarized images; we imaged 2D focus using a conventional achromatic lens (not a cylindrical lens) in a fluorescein solution. Figure 4.10 shows the successive images of 2D focus obtained by scanning the light focus in the *Z*-direction for different polarizations. Enlarged views of foci are shown for clarity here. The plots are drawn based on the peak intensity of the light focus along the axial direction. It is evident that the intensity of the 2D focus is highest at the center and gradually decreases as we move away from it. Additionally, these plots display roughly the same intensity for S and P polarizations, which is equal to half the intensity of the S+P image. Thus, as expected, the final image is generated by incoherently adding the S and P polarized images.

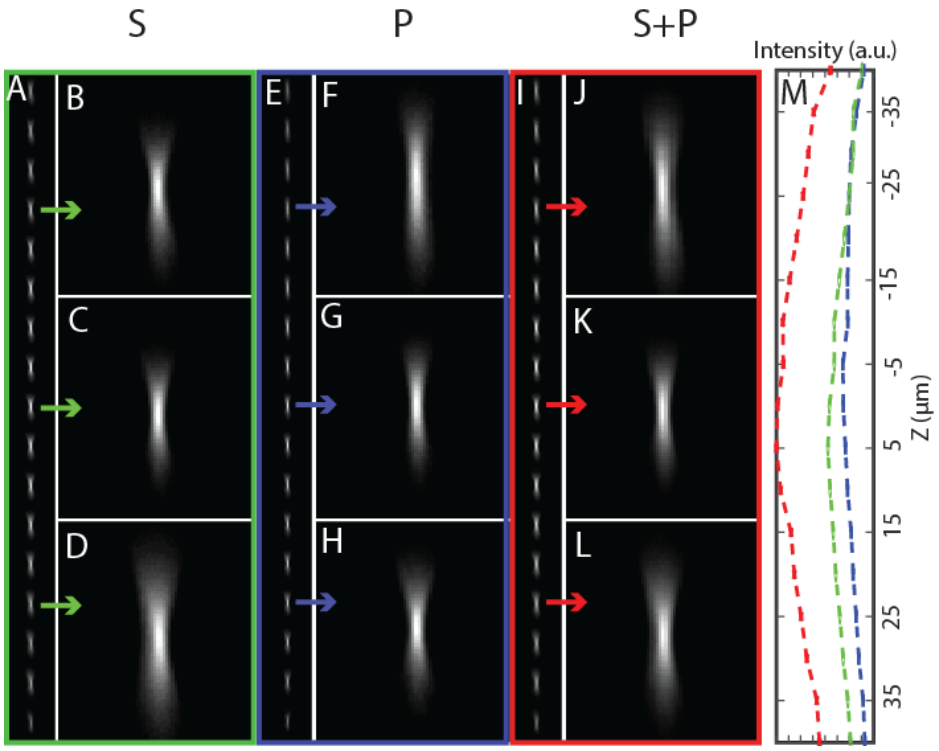

Figure 4.10. Scanning of the 2D focus and intensity evaluation along the axial direction. Images of the 2D focus along the axial direction for different polarizations formed by the conventional lens in fluorescein solution. The plot shows the same intensity of the S and P polarized focus along the *Z* direction which is maximum at the center and decreases gradually moving away from the center. The S+P focus intensity is added up incoherently by S and P foci.

4.3.5 Ray Tracing Simulation of the Detection Path

To understand the image formation of the proposed setup, we simulated the ray tracing of the detection path (Fig. 4.6a). The ray tracing assumes all rays satisfy paraxial approximation and all lenses are simple lenses. The detection objective is a water immersion objective, we calculated its effective focal length as $f_{\mathrm{obj}} = f_{\mathrm{Tube}} n / M_{\mathrm{obj}}$, where f_{Tube} is the focal length of the designed tube lens, M_{obj} is the magnification of the objective, and n is the refractive index of water. Here we have f_{obj} equal to 6.65 mm. The pmRF module (from the beam splitter to LFA) is modeled two times to simulate the forward and backward transmission through the module. The LFA is

omitted from the simulation, instead, we change the distance between the two copies of the pmRF objectives so that the distance (S_3) of the image plane to the second pmRF objective remains as a constant. We simulated with an object of 100 μm, the image size after the pmRF objective is ~140 μm, indicating a lateral magnification of 1.4, which is close to the requirement of perfect imaging with $M_{\text{lateral}} = n_{\text{water}}/n_{\text{air}} = 1.33$. The small deviation is limited by the geometry of the pmRF module: the separation (ΔL) of the S and P-images formed by the pmRF objective is approximate to $\Delta L = f_{\text{RFobj}}\theta$, where $f_{\text{RFobj}} = 10$ mm is the effective focal length of the RF objective and θ is the angle between the S and P-polarized rays meeting at the RF objective. The larger the ΔL, the larger the aberration introduced by the pmRF objective. To reduce ΔL, the pmRF objective is located ~500 mm from the PBS, therefore, the pmRF module is no longer an exact 4f system, the magnification, M_{lateral}, varies with the axial position of the object. Furthermore, the beam path from the detection objective to the tube lens is also not a 4f system, where the tube lens is ~100 mm away from the detection objective. The combination of the two non-4f systems can partially reduce the axial dependence of the magnification. Fig. 4.6b shows the change of the lateral magnification with respect to the galvo position (the axial position of the light sheet) from both ray tracing and the experimental data. There is a ~5% magnification change over an axial range of 80 μm. This magnification change can be further reduced by optimizing the axial position of the tube lens.

4.3.6 Rapid Dual-Color, Volumetric Imaging of Live Cells

As a first demonstration of the 3D cellular imaging capabilities, we monitored the 3D motion of secretory granules in living mast cells. Mast cells possess distinct secretory granules that contain the mediators of the allergic response and are released upon mast cell activation by allergen[138]. These granules are distributed across the cytosol and have been shown to undergo both Brownian diffusion and directed motion[138]. Upon activation of the membrane receptor, FcεRI, via crosslinking by multivalent antigen[139,140], the granules undergo increased directed motion that moves them to the plasma membrane where they will fuse and release mediators that regulate allergic responses[138,141].

We applied the developed system for dual-color, volumetric imaging of live cells and tracked the 3D motion of green fluorescent protein-labeled Fas ligand (GFP-FasL) loaded secretory granules in the cytosol of RBL-2H3 mast cells [138]. IgE-bound FcεRI was simultaneously imaged by addition of anti-DNP IgE-CF640R. With addition of the antigen-mimic, DNP-conjugated to BSA (DNP-BSA), FcεRI aggregates and undergoes endocytosis as seen in Figure 4.11a. During data acquisition, the light sheet is parallel to the *XY* plane and scans along the *Z* direction. Within the light-sheet region, the *XY* and *XZ* maximum intensity projections (Fig.4.11a) of the cell image show GFP-FasL granules in three dimensions. The cells were imaged at ~ 0.6 volumes (80×15×40 μm^3 in *XYZ*) per second for 80 volumes, for a total imaging time of ~2 minutes (Fig.4.11a-d). To quantify the granule dynamics, isolated granules were identified and tracked in 3D using the U-track3D software[142]. We calculated the mean square displacement (MSD) of each trajectory over time and extracted the diffusion coefficient, D, and velocity, v, by fitting the MSD curve with

$MSD(t) = 6Dt^2 + v^2t^2 + o$, where o is an offset related to localization and tracking uncertainties[143,144] (Fig.4.11c,d). We found that most granules undergo Brownian Diffusion and a few exhibited directed motion, consistent with granules being transported along the microtubules (Fig.4.11a,b)[138]. The measured transport velocities of the two trajectories indicated in Fig.4.11a,b are ~0.1 μm/s, consistent with previous work that performed tracking in 2D[138].

To test the limits of the new system in terms of speed, we set out to image Brownian motion on the microscopic level. For this, we stressed the cells by incubating them in Hank's balanced salt solution (HBSS) (Method) at room temperature for over 1 hour, which induced cell blebbing. This also caused more rapid diffusion of the granules that we were able to capture using an imaging speed of ~8.3 volumes/s for 80 volumes for a total time of 10 s. With this imaging speed, we retained good signal-to-noise and the ability to track the 3D motion of individual granules (Fig 4. 11e-g). Under these non-physiological conditions, average granule diffusion was increased by ~41 times (Fig.4.11h). Two tracks shown in Fig. 4.11e have diffusion coefficients of 0.41 $\mu m^2/s$ and 0.64 $\mu m^2/s$.

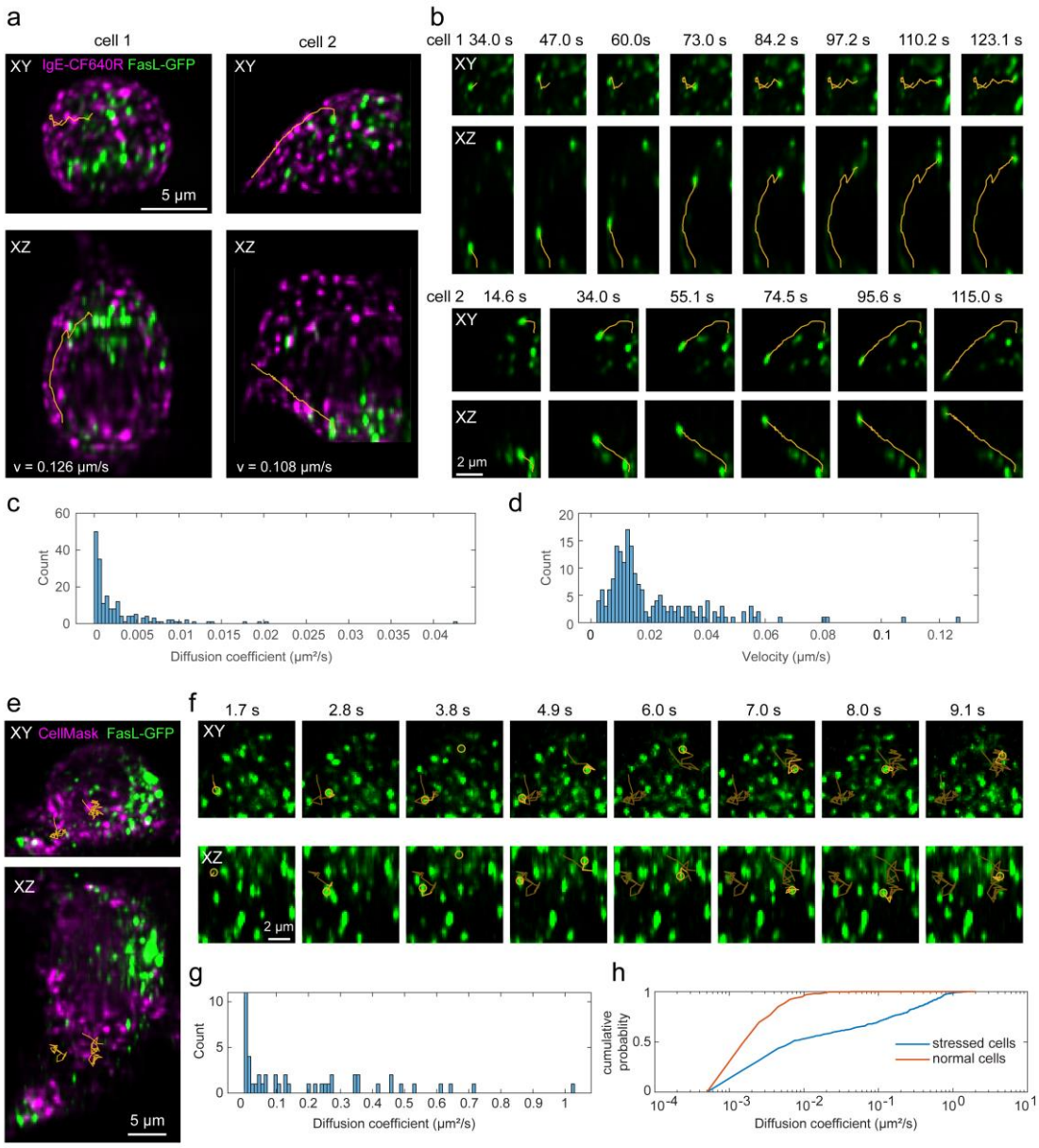

Figure 4.11.Dual-Color volumetric imaging of live RBL cells. (a-d) Dual-color volumetric imaging of granule motions in a live RBL-2H3 GFP-FasL cell, where the cell membrane is labeled with IgE-CF640R and granules contain GFP-FasL, at an imaging speed of ~ 0.6 volumes (80×15×40 μm^3 in *XYZ*) per second for 80 volumes, for a total imaging time of ~2 minutes. (a) Maximum intensity projection views of the cell images at one-time point and overlay with representative trajectories of granule movement (orange lines). (b) Time series of the trajectories in a. (c, d) Histograms of estimated diffusion coefficients and velocities of all trajectories found in cell 1 and cell 2. (e-g) Dual-color volumetric imaging of live RBL-2H3 GFP-FasL cell, where the cell membrane is labeled with CellMask DeepRed and the granules contain GFP-FasL using an imaging speed of ~8.3 volumes/s for 80 volumes for a total time of 10 s. (e) Maximum intensity projection views of the cell images at one-time point and overlay with representative trajectories of granule movement (orange lines). (f) Time series of the trajectories in e. (g) Histograms of estimated diffusion coefficients of all trajectories in the cell. (h) Cumulative probability of the estimated diffusion coefficients under normal (a-d) and stressed (e-g) imaging conditions. 400-500 trajectories with a diffusion coefficient > 0.001 μm^2/s from four cells under each condition are selected.

4.4 Discussion

In this work, we developed an axial scanning module in the detection path of a light-sheet microscope utilizing the pmRF technique proposed by Botcherby et al.[73,105]**.** While inheriting all the benefits from the pmRF technique, such as fast scanning and all-optical aberration compensation (no wavefront control element), our design overcomes a critical limitation of the original pmRF technique, as in, the loss of 50% of the emitted fluorescence in the detection path[127,130,145]. Here we engineered a new optical design, where we split the emitted fluorescence into S and P polarized light to carryout remote focusing and then seamlessly combine them to achieve minimum light loss.

We demonstrated our implementation of the developed scanning module through a light-sheet microscope with two orthogonally arranged objectives. We can perform simultaneous two-color imaging at 8.3 volumes (80×15×40 μm^3 in *XYZ*) per second with a lateral resolution of 394 nm and an axial resolution of 650 nm (after deconvolution). As our method is fully optical, the imaging speed scales with advancements in LFA technology and camera acquisition speed.

The S and P polarized beams are directed at an oblique angle into the remote objective (*Fig.4.5b*). This angled approach creates two separate images at the mirror attached to the LFA (M3). However, there are limitations to this angular arrangement. The two images formed away from the optical axis are prone to aberrations. To reduce the image separation, the remote objective must be positioned further from the PBS to reduce the incident angles of S and P-polarized lights. However, this increased distance breaks the 4f configuration between the two objectives (detection and remote objectives) that is critical to achieving aberration-free imaging. Future

studies will investigate into more compact designs that will better satisfy the 4f condition and will reduce the separation between the two foci at M3.

Of note, our approach offers several advantages over the existing axial refocusing methods. First, it provides an extended, aberration-free scan range for high numerical aperture (NA) optics. This is a significant benefit when compared to techniques based on deformable mirrors (DMs), where our method approximately doubles the axial scan range of DMs[70]. Second, it is wavelength independent, which makes it suited for simultaneous multicolor imaging when compared to SLMs and tunable lenses. Additionally, unlike SLMs which depend on polarization, our arrangement is not dependent on the polarization of the fluorescence. Furthermore, unlike SLMs, which are typically slow (especially the nematic liquid crystal ones), and even their faster counterparts (ferroelectrics) tend to be less effective, our method allows for imaging speed that are only limited by the sCMOS's framerate.

Although recent advancements in single-objective oblique plane microscopy (OPM) have achieved speeds comparable to our method, our technique presents several notable advantages. In OPM, the de-scanning of the returning fluorescent light leads to skewed images. Before these images can be viewed, they require intensive de-skewing processes[113,146–150].On the other hand, our approach captures 3D volumes in a conventional orthogonal setup. This is achieved by recording high-speed images while sweeping the light-sheet through the sample. Each frame captured by the camera represents an optical cross-section of the specimen. As a result, the 3D image stacks generated using our method are immediately available for viewing. They may benefit from an optional deconvolution, but there's no delay caused by necessary post-processing. Furthermore, the OPM setup necessitates a third objective, which in the latest setups

require expensive objectives like ‘Snouty’ or ‘King Snout’[113,146–149]. Our setup on the other hand does not have this requirement and our secondary objective performs the role of a tertiary objective. Moreover, while not demonstrated explicitly here, our method can be employed to achieve isotropic resolution, a feat the OPM cannot achieve.

Compared with the original Botcherby's remote focusing setup, our pmRF module folds the beam path between the detection and the remote objectives. This configuration complicated the optical alignment. A potential solution is to arrange both objectives inline in a 4f configuration. Furthermore, we note that although an all-optical design has its merit of simplicity and robustness, using an objective lens in the pmRF module introduces ~30-40% light loss (Fig.4.12) compared with the axial scanning techniques based on DMs, future development of objective with high-transmission efficiency is desirable.

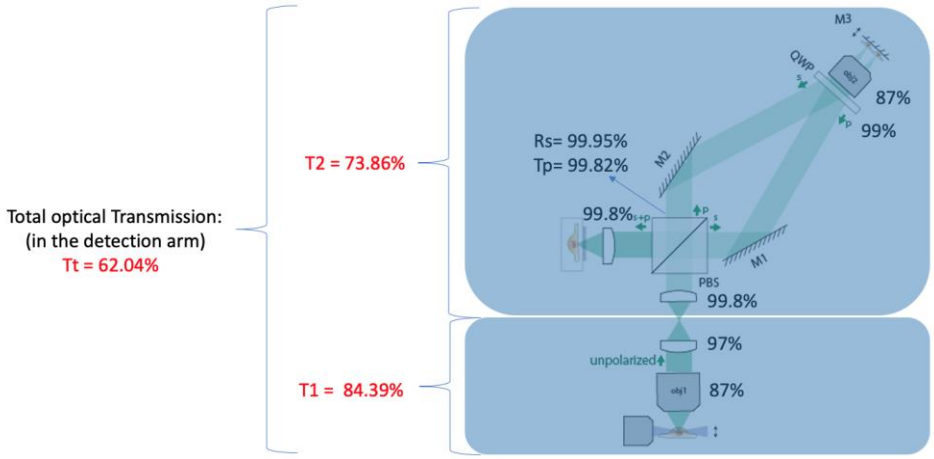

Figure 4.12. Quantify optical transmission through the microscope. Our proposed configuration introduces 26.14% light loss to the microscope.

4.5 Summary

In our study, we developed a novel axial scanning module based on the pupil-matched remote focusing (pmRF) technique. This design allows for rapid scanning and optical aberration compensation without the need for wavefront control elements. Our innovative approach overcomes light loss limitations of the original pmRF technique by collecting both S and P-polarized light.

Our module has potential applications across a range of microscopy modalities such as confocal, two-photon, and light-sheet microscopy, as it revolutionizes their axial scanning capabilities. In our implementation of this scanning module on a light-sheet microscope with two orthogonally arranged objectives, we achieved simultaneous two-color imaging at 8.3 volumes per second, with impressive resolution and minimal aberration.

A significant challenge in biomedical imaging is to carry out high-resolution volumetric imaging of live cells without disrupting the specimen. Previous solutions have faced issues with aberrations introduced by the focusing elements. Our design elegantly bypasses these issues by splitting the fluorescent signal into S and P-polarized light, which then traverse through the remote focusing module separately before being recombined at the camera. This method facilitates aberration-free, volumetric imaging without compromising the fluorescent signal or requiring sample/objective translation.

We demonstrated our system's capabilities by capturing rapid, dual-color 4D image stacks, covering an axial range of 70 µm at an acquisition speed of 700 frames per second. While

demonstrated using light-sheet microscopy, our technique has the potential to enhance other microscopy techniques that rely on axial scanning.

Finally, it is our firm belief that owing to its generalized design, we envision our method has the potential to transform many popular microscope modalities like confocal, 2-photon, and the rapidly emerging field of light sheet microscopy, by reinventing how they perform scanning in the axial dimension.

CHAPTER 5: Conclusion and Future Directions

5.1 Conclusion

5.1.1 Axially Swept Light Sheet Microscopy (ASLM)

The culmination of this research introduces a new concept in the field of Axially Swept Light Sheet Microscopy (ASLM), which considerably enhances the capabilities of the existing technique. ASLM is a valuable tool in biology and medicine, enabling isotropic subcellular resolution imaging over a large field-of-view (FOV) in diverse specimens, from live cells to chemically cleared organs. Our advanced ASLM model relies on scanning two staggered light sheets simultaneously, synchronized with a scientific camera's rolling shutter. As such, this approach facilitates either twice as fast imaging or doubled detection signal, depending on the experimental needs, without compromising the other factor.

Our optical system demonstrates considerable potential, illustrated through successful imaging of fluorescent beads and a PEGASOS cleared-tissue mouse brain. This modification builds upon the original ctASLM design, enabling multicolor imaging across an extensive refractive index range with diffraction-limited isotropic resolution. Our version of ASLM can be considered a significant advancement for large-volume 3D imaging of tissues, as it optimizes the balance between imaging speed, detected signal, and gentle illumination.

5.1.2 Axial de-Scanning in the Detection Arm of Light Sheet Microscope

This research aimed to develop an innovative approach to overcome the challenges associated with high-speed, high-resolution volumetric imaging of live cells without agitating the biological specimen. In this regard, our novel optical design utilizing the pupil-matched remote focusing (pmRF) technique has shown substantial promise.

Our study demonstrated the new system's efficacy by acquiring fast, dual-color, four-dimensional image stacks at an axial range of 70 µm and an acquisition speed of 700 frames per second. The developed system successfully bypasses the significant limitations of existing remote focusing techniques, namely the aberrations introduced by focusing elements and the constraints associated with manipulating incoherent and unpolarized fluorescence light. Our design separates the S and P polarized fluorescence signals, allows them to pass through the remote focusing module independently, and recombines them at the camera, enabling an aberration-free, volumetric imaging without compromising the fluorescent signal or necessitating any sample/detection-objective translation.

The key strengths of our pmRF approach include an extended aberration-free scan range for high numerical aperture (NA) optics, wavelength independence facilitating simultaneous multi-color imaging, compatibility with unpolarized light, and fast imaging capabilities restricted only by the camera's frame rate. Moreover, it employs a linear focus actuator (LFA) as a refocusing element, avoiding the complexities associated with deformable mirrors (DMs) or spatial light modulators (SLMs), thus simplifying implementation.

5.2 Future Directions

5.2.1 Axially Swept Light Sheet Microscopy (ASLM)

Despite these advancements, our work has opened several avenues for future exploration and improvement in the realm of ASLM.

5.2.2 .1 Maximizing Light Sheets

While our current design uses two light sheets, it is theoretically possible to use an arbitrary number of sheets for superior signal-to-noise ratio (SNR). This approach, however, comes with practical considerations, including the capability of sCMOS cameras for independent rolling shutter operation across multiple regions and the potential detrimental impact of unfocused light from one light sheet bleeding into the waist of another. Simulations suggest that up to four 0.4 NA light sheets might be feasible within the FOV. Hence, future research may investigate the possibilities of using multiple light sheets in conjunction with advanced sCMOS camera technology.

5.2.2.2 Improved Light Sheet Control

Our current design utilizes a combination of concave and convex lenses to control the axial separation of the light sheets. This arrangement, while effective, causes a slight change in focal lengths and effective magnification for the two states of polarization in the illumination arm. It has been a challenge to synchronize the rolling shutter in two FOVs due to these changes, and it has led to some resolution loss. Several alternative schemes, including the use of a step or a tilted mirror in the remote focusing arm, a binary SLM to generate tiled discontinuous light sheets, or the pLSFM scheme, could simplify light sheet separation control and maintain resolution. More precise control over light sheet positions could translate into even faster imaging speeds.

5.2.2.3 Increasing Imaging Speed and FOV Coverage

Our preliminary experiments suggest that with the optimized control over light sheet positions, we could potentially triple the imaging speed with 95% FOV coverage. The feasibility of this approach needs further exploration, which we aim to undertake in our future research.

5.2.2.4 Evaluating Light Dosage Effects

While our method illuminates the sample for twice the dwell time, thereby doubling the signal intensity as evaluated by SNR, it does also double the light dosage to the sample. While we have maintained a constant peak illumination power in each focus to ensure gentle illumination, the impacts of this increased light dosage on sample integrity and photobleaching effects merit further investigation.

5.2.2 Axial de-Scanning in the Detection Arm of Light Sheet Microscope

While our novel optical design significantly advances real-time functional imaging of live cells, there are avenues for improvement and adaptation.

5.2.2.1 Design Optimization

The current configuration has the S and P polarized beams directed at an oblique angle into the remote objective, creating two separate images prone to aberrations. A more compact design can be achieved by adding a right-angle mirror between the mirrors M1 and M2. This adaptation will

maintain the critical 4f configuration between the detection and remote objectives while minimizing the separation between S and P images.

5.2.2.2 Improved Optical Alignment

The pmRF module's current arrangement folds the beam path between the detection and the remote objectives, complicating optical alignment. In future iterations of the system, arranging both objectives inline in a 4f configuration could potentially simplify optical alignment.

5.2.2.3 High-Transmission Efficiency Objective

Given that the use of an objective lens in the pmRF module introduces a light loss of around 30-40%, it is desirable to explore the development of objectives with higher transmission efficiency. These advancements will enhance the performance of our system and facilitate its use in more demanding applications.

5.2.2.4 Extension to Other Microscopy Techniques

While we have primarily demonstrated our approach using light-sheet microscopy, there is potential to apply the pmRF technique to other microscopy techniques that rely on axial scanning. Future work should focus on extending this design to microscopy modalities such as confocal, two-photon, and even super-resolution imaging.

In conclusion, our findings offer an advanced ASLM method, facilitating the improvement of imaging speed and signal detection in a range of biological specimens. By further examining and addressing the considerations raised in this study, future research has the potential to push the boundaries of ASLM and revolutionize the field of large volume 3D imaging. We also believe that our findings provide a significant step forward in the field of real-time functional imaging of live cells. The future adaptation and optimization of the proposed system may lead to its widespread use, driving a paradigm shift in how microscopic scanning in the axial dimension is conducted in diverse fields of biological and biomedical imaging.

APPENDICES

APPENDIX A

Sample Preparation of Cleared-Tissue Mouse Brain

Briefly, mice were anesthetized and perfused transcardially with 50ml ice-cold heparin PBS and then 50ml 4% PFA. We then dissected the mouse brain and fixed it in 4% PFA overnight at room temperature. Following fixation, samples were washed with PBS and then incubated with decolorization solution (25% (v/v in H2O) Quadrol (Sigma-Aldrich, 122262) at 37C with gentle shaking. The decolorization process lasted 2 days, with a daily change of Quadrol. Subsequently, we immersed samples in gradient tert-butanol (tB) solutions (30% tB (Sigma-Aldrich, 471712) solution (70% v/v H2O, 27% v/v tB and 3% w/v Quadrol), (2) 50% tB solution (50% v/v H2O, 47% v/v tB and 3% w/v Quadrol) and (3) 70% tB solution (30% v/v H2O, 67% v/v tB and 3% w/v Quadrol)) at 37C with gentle shaking on two consecutive days. Next samples were dehydrated with tBP solution containing 70% tB, 27% (v/v) poly (ethylene glycol) methyl ether methacrylate average Mn500 (PEG MMA500) (Sigma-Aldrich, 447943), and 3% (w/v) Quadrol at 37C for 2 days, with solution, changed daily. Finally, samples were immersed in BBP clearing medium (consisting of 75% (v/v) benzyl benzoate (Sigma-Aldrich, B6630), 22% (v/v) PEG MMA500, and 3% (w/v) Quadrol) at 37C with shaking until reaching complete transparency. Samples were then kept in BBP clearing medium before imaging.

APPENDIX B

Inherent Limitations of Linear Optical Elements in Achieving Full Polarization of Unpolarized Light

It should be emphasized here that such a pmRF configuration would have been feasible if the conversion of unpolarized light into fully polarized light with unity transmission efficiency were possible. However, to the best of our knowledge, using purely linear optical elements such as a lossless conversion is not yet possible [134,135]. This can be shown mathematically as follows: a fully unpolarized light with normalized intensity can be represented by a coherency matrix[13],

$$S = \frac{1}{2}\begin{bmatrix}1 & 0\\ 0 & 1\end{bmatrix} = \frac{1}{2}I, \qquad \text{(Appendix B.1)}$$

where I represents the identity matrix. A linear polarization device can be represented by a Jones matrix J[151]. If such a device is lossless, J must be unitary which satisfies [152],

$$J^{\dagger}J = I, \qquad \text{(Appendix B.2)}$$

where the dagger represents conjugate transpose. Propagation of the unpolarized light through a lossless polarization device can be calculated from[153],

$$S' = J^{\dagger}SJ = \frac{1}{2}J^{\dagger}J = \frac{1}{2}I = S, \qquad \text{(Appendix B.3)}$$

where the output light is identical to the input light. Therefore, no matter which linear polarization device is used, the output light remains unpolarized.

APPENDIX C

Bead and Cell Sample Preparation for Axial De-Scanning Microscope

Bead sample:200 nm beads embedded in 2% agarose gel was used for microscope resolution assessment. To make 2% agarose gel, 2 g of agarose powder (A9045-25G, SIGMA life science) was mixed with 100 mL water and swirled thoroughly before putting into the microwave oven to heat. Once the solution boiled and got completely clear and the agarose was dissolved, we should remove the solution from the oven and let it cool down. Then, 200 nm beads (YG, Polysciences) were mixed with water with a ratio of 1/100 to form a solution of the 200 nm beads. It was sonicated before mixing with the molten 2% agarose gel with a volumetric ratio of 1/10. Then this molten combination was poured into the cubic mold where the sample holder was placed there and sat there for a few minutes to dry and form a $1cm^3$ cubic sample (200 nm beads embedded into 2% agarose gel) attached to the sample holder.

Cell samples: RBL-2H3 GFP-FasL cells were cultured in Gibco Minimum Essential Media (MEM) media supplemented with 10% heat-inactivated Fetal Bovine Serum (FBS), 1% Penicillin/Streptomycin, and 1% L-glutamine [138]. The cells were primed with 1 µg/ml anti-DNP-IgE[154] (Fig. 4.11e-g) or anti-DNP-IgE-CF640R (Fig. 4.11a-d) and seeded at a density of 100,000 cells per well in 12 well dish over 5 mm glass coverslips and incubated with 5% CO_2 at 37°C overnight. IgE-CF640R was prepared using CF640R NHS-ester (Biotium #92108). For fast imaging experiments, the cellular membranes of anti-DNP-IgE primed cells were labeled with CellMask™

Deep Red Plasma Membrane Stain (Thermo Fisher Scientific #C10046, 5mg/ml, 1000X) according to manufacturer's instruction for 10 minutes in modified Hank's balanced salt solution (HBSS) (additional 10 mM Hepes, 0.05% w/v BSA, 5.45 mM glucose, 0.88 mM $MgSO_4$, 1.79 mM $CaCl_2$, 16.67 mM $NaHCO_3$) and rinsed with HBSS. Cells were stimulated with 1 μg/ml DNP-BSA in the sample chamber. Data was acquired in 2 min captures for up to 15 minutes post antigen treatment.

APPENDIX D

Sample Mounting in Axial De-Scanning Microscope

Cells samples on 5 mm coverslips were loaded onto the holder as depicted in Appendix Fig.1. In the sample holder, two metal wires were designed to clamp the coverslip tightly. This sample holder was attached to the *XYZ* Translation Stage with Standard Micrometers using a rotation mount. As a result, the coverslip had four degrees of freedom, including the translation on the *X-Y-Z* axis to locate the cells while imaging and the rotation around the X-axis to face the coverslip with the desired angle relative to the illumination and detection objectives. Here, the coverslips were faced 8 degrees relative to the optic axis of the detection objective (Appendix Fig.1). In order to minimize the buffer volume for live cell imaging, the 6 ml chamber was designed to immerse the sample, illumination, and detection of objective lenses into it (Appendix Fig.1).

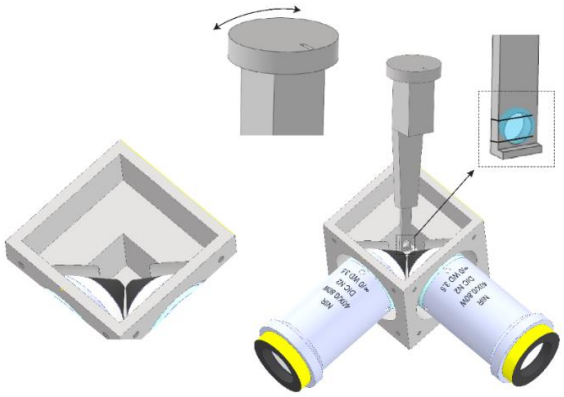

Appendix Figure 1. Sample holder and chamber. Perpendicular architecture of illumination and detection objectives which are immersed in water media or similar (Hanks's buffer) for live cell imaging. The chamber volume is 6 ml to minimize using the antigen. The bottom part of the sample holder has two clamps to clip the 5 mm coverslip and the upper part is designed in a circular shape to be attached to the rotation mount capable of changing the coverslip angle relative to the light sheet propagation direction.

APPENDIX E

Image Processing Pipeline in Axial De-Scanning Microscope

Data were analyzed with the custom script written in Matlab. The procedure for quantifying the microscope's resolution from fluorescence bead data is as follows: 1) A 3D-PSF model was generated from the raw data. 2) The light-sheet region was cropped from each slice of the raw data. The width of the light-sheet region was defined by the distance to the waist of the light-sheet where the axial resolution increases by 2 times. We sat the light-sheet width to be ~6 mm. Note that the light-sheet region translated along its width direction (the *Y*-axis) while it was being scanned in the axial direction (*Z*-axis relative to the detection objective) (Fig.4.8). Therefore, the light-sheet region to be cropped was also shifted in *Y* accordingly (Supplementary Video 1). 3) the cropped region was deconvolved with the 3D-PSF model using Richard-Lucy deconvolution from ImageJ. 4) the deconvolved data stack was divided into segments with an axial dimension of 5 µm. For each segment, candidate beads were selected and their FWHMs along each dimension were estimated from Gaussian fitting of their intensity profiles along that dimension. 5) the measured FWHMs were used to quantify the resolution of the microscope as shown in Fig. 4.6d.

Dual-color live-cell data was processed as follows: 1) cell signal from each color channel was cropped with a user-selected region. 2) for each color channel, the *XYZ* drifts of the data stack at each time point relative to the reference data stack were estimated, where the maximum-intensity projection (MIP) along each dimension of the two data stacks was generated and the 2D

shift between each pair of the MIP images was calculated through cross-correlation. 3) an average of the *XYZ* shifts from both channels was used to correct the drift between time points. 4) the *XYZ* shift between the two-color channels was calculated by first averaging over the time dimension for each color channel, then estimating the shift from the MIP images as in step 3. Then register the two channels by applying the estimated shift. 5) after drift correction and channel registration, the resulting image stacks were deconvolved with the 3D-PSF model generated from the bead data using Richard-Lucy deconvolution from Matlab. 6) to reduce noise and correct photo-bleaching, the deconvolved images were subtracted by a background value with negative pixel values set to zero and divided by a normalization factor equal to the 99.95 quantiles of all pixel values in the corresponding time points and color channel.

APPENDIX F

Ray Tracing Method in the Detection Path of Axial Re-Focusing Module

Ray tracing was based on geometric optics with paraxial approximation. The ray propagation was calculated using the ABCD matrices. Two matrices were used, the translation matrix,

$$M_d = \begin{bmatrix} 1 & 0 \\ d/n & 1 \end{bmatrix}, \quad \text{(Appendix F.1)}$$

and the matrix of a thin lens,

$$M_f = \begin{bmatrix} 1 & -n/f \\ 0 & 1 \end{bmatrix}, \quad \text{(Appendix F.2)}$$

where d is the translation distance, f is the focal length of the thin lens and n is the refractive index of the propagation medium. For our system, n is 1.33 before the detection objective (including the objective) and n equals 1 for the rest of the ray tracing. The starting point of each ray was represented by a vector of $[n\alpha, y]^T$, where α and y are the angle and the y position of the ray with respect to the optical axis. The propagation of the ray is then calculated from

$$\begin{bmatrix} n\alpha' \\ y' \end{bmatrix} = M \begin{bmatrix} n\alpha \\ y \end{bmatrix}. \quad \text{(Appendix F.3)}$$

For a defined FOV, we selected three field points, two mark the edge of the FOV and one at the optical axis. For each field point, we generated three rays at different angles that will intersect three points at the pupil plane, where two points mark the edge of the pupil and one at the center of the pupil. Rays from the same field point were colored the same. The optical axis after the polarizing beam splitter was rotated by 45 degree to be along the splitting plane of the PBS. The

ray tracing after the PBS was done by first transforming the ray coordinates to the ones defined by the optical axis and propagating the ray with the ABCD matrix, then transforming back to the global coordinates. Except for the distance between the tube lens and the detection objective (denoted as d_1), the rest distances between consecutive optical elements were measured with a ruler. The angle between the chief rays of the S and P-polarization (θ in Fig.4.6a) was set when the input and output beam diameters at the remote focusing objective were minimum. The distance d_1 was set when the relative magnifications from ray tracing match with the measured ones (Fig. 4.6b). The central position of the scan range, the distance of the objective to the detection objective (denoted as S_1), was set when the absolute magnification from ray tracing matches with measured one. Here $S_1 = 6.695$ mm, which was 45 μm away from the designed focal plane of the detection objective.

REFERENCES

1. "An Introduction to the Light Microscope, Light Microscopy Techniques and Applications," http://www.technologynetworks.com/analysis/articles/an-introduction-to-the-light-microscope-light-microscopy-techniques-and-applications-351924.
2. M. Chen, L. Tian, and L. Waller, "3D differential phase contrast microscopy," Biomed. Opt. Express, BOE **7**(10), 3940–3950 (2016).
3. J. W. Lichtman and J.-A. Conchello, "Fluorescence microscopy," Nat Methods **2**(12), 910–919 (2005).
4. J. Selinummi, P. Ruusuvuori, I. Podolsky, A. Ozinsky, E. Gold, O. Yli-Harja, A. Aderem, and I. Shmulevich, "Bright Field Microscopy as an Alternative to Whole Cell Fluorescence in Automated Analysis of Macrophage Images," PLOS ONE **4**(10), e7497 (2009).
5. R. Oldenbourg, "Polarized Light Microscopy: Principles and Practice," Cold Spring Harb Protoc **2013**(11), pdb.top078600 (2013).
6. F. L. Pedrotti, L. M. Pedrotti, and L. S. Pedrotti, *Introduction to Optics* (Cambridge University Press, 2017).
7. "The Microscope Objective," in *Understanding Light Microscopy* (John Wiley & Sons, Ltd, 2019), pp. 127–160.
8. "Airy disk," Wikipedia (2023).
9. "Rayleigh Criterion | COSMOS," https://astronomy.swin.edu.au/cosmos/r/rayleigh+criterion.
10. M. J. Booth, "Microscope Resolution Estimation and Normalised Coordinates," (2020).
11. "Depth of Field and Depth of Focus | Edmund Optics," https://www.edmundoptics.com/knowledge-center/application-notes/imaging/depth-of-field-and-depth-of-focus/.
12. "Basic Microscope Optics," in *Understanding Light Microscopy* (John Wiley & Sons, Ltd, 2019), pp. 55–74.
13. J. Goodman, *Introduction to Fourier Optics*, 3rd edition (Roberts and Company Publishers, 2004).
14. S. Liu, "Development of optical systems and imaging analyses for hyperspectral microscopy and 3D super-resolution imaging," Optical Science and Engineering ETDs (2015).
15. M. J. Nasse and J. C. Woehl, "Realistic modeling of the illumination point spread function in confocal scanning optical microscopy," J. Opt. Soc. Am. A, JOSAA **27**(2), 295–302 (2010).
16. "Point spread function," Wikipedia (2023).
17. M. Born, E. Wolf, and A. B. Bhatia, *Principles of Optics: Electromagnetic Theory of Propagation, Interference and Diffraction of Light* (Cambridge University Press, 1999).
18. "Deconvolution," Wikipedia (2023).
19. "Deconvolution Toolkit for Life Science Research," https://www.zeiss.com/microscopy/en/products/software/zeiss-zen/deconvolution-toolkit.html.
20. "Operating the Confocal Microscope," in *Understanding Light Microscopy* (John Wiley & Sons, Ltd, 2019), pp. 447–481.

21. T. H. Lee, *The Design of CMOS Radio-Frequency Integrated Circuits, Second Edition*, 2nd edition (Cambridge University Press, 2003).
22. "Contrast Generation and Enhancement," in *Understanding Light Microscopy* (John Wiley & Sons, Ltd, 2019), pp. 243–287.
23. "Fluorescence - Wikipedia," https://en.wikipedia.org/wiki/Fluorescence.
24. "Fluorescence Microscopy," in *Understanding Light Microscopy* (John Wiley & Sons, Ltd, 2019), pp. 383–403.
25. "Fluorophores and Fluorescent Proteins," in *Understanding Light Microscopy* (John Wiley & Sons, Ltd, 2019), pp. 405–423.
26. L. Fang, F. Monroe, S. W. Novak, L. Kirk, C. R. Schiavon, S. B. Yu, T. Zhang, M. Wu, K. Kastner, A. A. Latif, Z. Lin, A. Shaw, Y. Kubota, J. Mendenhall, Z. Zhang, G. Pekkurnaz, K. Harris, J. Howard, and U. Manor, "Deep learning-based point-scanning super-resolution imaging," Nat Methods **18**(4), 406–416 (2021).
27. J. Icha, M. Weber, J. C. Waters, and C. Norden, "Phototoxicity in live fluorescence microscopy, and how to avoid it," BioEssays **39**(8), 1700003 (2017).
28. P. Karran and R. Brem, "Protein oxidation, UVA and human DNA repair," DNA Repair **44**, 178–185 (2016).
29. "Sir George Stokes, 1st Baronet," Wikipedia (2023).
30. "Fluorescence microscope," Wikipedia (2023).
31. "Optical Sectioning and Confocal Microscopy," in *Understanding Light Microscopy* (John Wiley & Sons, Ltd, 2019), pp. 425–446.
32. "Multi-Photon Microscopy," in *Understanding Light Microscopy* (John Wiley & Sons, Ltd, 2019), pp. 543–560.
33. "Super-Resolution Fluorescence Microscopy," in *Understanding Light Microscopy* (John Wiley & Sons, Ltd, 2019), pp. 613–636.
34. "Foldout," in *Understanding Light Microscopy* (John Wiley & Sons, Ltd, 2019), pp. 816–817.
35. Y. Choe, "Physical Sectioning Microscopy," in *Encyclopedia of Computational Neuroscience*, D. Jaeger and R. Jung, eds. (Springer, 2013), pp. 1–4.
36. "Light-Sheet Microscopy," in *Understanding Light Microscopy* (John Wiley & Sons, Ltd, 2019), pp. 483–506.
37. S. Gul, M. S. Khan, A. Bibi, A. Khandakar, M. A. Ayari, and M. E. H. Chowdhury, "Deep learning techniques for liver and liver tumor segmentation: A review," Computers in Biology and Medicine **147**, 105620 (2022).
38. G. Meng, "High-Throughput Volumetric Imaging of Neural Dynamics in vivo," Ph.D., University of California, Berkeley (2021).
39. M. D. Wong, A. E. Dorr, J. R. Walls, J. P. Lerch, and R. M. Henkelman, "A novel 3D mouse embryo atlas based on micro-CT," Development **139**(17), 3248–3256 (2012).
40. H. Dibaji, A. K. N. Shotorban, M. Habibi, R. M. Grattan, S. Lucero, D. J. Schodt, K. A. Lidke, J. Petruccelli, D. S. Lidke, S. Liu, and T. Chakraborty, "Axial de-scanning using remote focusing in the detection arm of light-sheet microscopy," 2023.09.07.556729 (2023).
41. Y. Wang and H. Jeon, "3D cell cultures toward quantitative high-throughput drug screening," Trends in Pharmacological Sciences **43**(7), 569–581 (2022).
42. Y. Zhao, M. Zhang, W. Zhang, Y. Zhou, L. Chen, Q. Liu, P. Wang, R. Chen, X. Duan, F. Chen, H. Deng, Y. Wei, P. Fei, and Y.-H. Zhang, "Isotropic super-resolution light-sheet microscopy of

dynamic intracellular structures at subsecond timescales," Nat Methods **19**(3), 359–369 (2022).
43. "CMOS cameras | Hamamatsu Photonics," https://www.hamamatsu.com/us/en/product/cameras/cmos-cameras.html.
44. Y. S. Bykov, M. Cortese, J. A. G. Briggs, and R. Bartenschlager, "Correlative light and electron microscopy methods for the study of virus–cell interactions," FEBS Letters **590**(13), 1877–1895 (2016).
45. M. Wilson, J. DeRose, and C. Greb, "Introduction to Widefield Microscopy," (2017).
46. "IF imaging: Widefield versus confocal microscopy," https://www.ptglab.com/news/blog/if-imaging-widefield-versus-confocal-microscopy/.
47. C. Ren and T. Komiyama, "Wide-field calcium imaging of cortex-wide activity in awake, head-fixed mice," STAR Protocols **2**(4), 100973 (2021).
48. H. Dibaji, M. N. H. Prince, Y. Yi, H. Zhao, and T. Chakraborty, "Axial scanning of dual focus to improve light sheet microscopy," Biomed. Opt. Express, BOE **13**(9), 4990–5003 (2022).
49. O. E. Olarte, J. Andilla, E. J. Gualda, and P. Loza-Alvarez, "Light-sheet microscopy: a tutorial," Adv. Opt. Photon. **10**(1), 111 (2018).
50. B.-C. Chen, W. R. Legant, K. Wang, L. Shao, D. E. Milkie, M. W. Davidson, C. Janetopoulos, X. S. Wu, J. A. Hammer, Z. Liu, B. P. English, Y. Mimori-Kiyosue, D. P. Romero, A. T. Ritter, J. Lippincott-Schwartz, L. Fritz-Laylin, R. D. Mullins, D. M. Mitchell, J. N. Bembenek, A.-C. Reymann, R. Böhme, S. W. Grill, J. T. Wang, G. Seydoux, U. S. Tulu, D. P. Kiehart, and E. Betzig, "Lattice light-sheet microscopy: Imaging molecules to embryos at high spatiotemporal resolution," Science **346**(6208), 1257998 (2014).
51. "Lattice Lightsheet 7," https://www.zeiss.co.kr/microscopy/local-content/campaign/google-ad-for-lead-gen/zeiss-lattice-lightsheet-7.html.
52. U. Krzic, S. Gunther, T. E. Saunders, S. J. Streichan, and L. Hufnagel, "Multiview light-sheet microscope for rapid in toto imaging," Nat Methods **9**(7), 730–733 (2012).
53. R. Tomer, K. Khairy, F. Amat, and P. J. Keller, "Quantitative high-speed imaging of entire developing embryos with simultaneous multiview light-sheet microscopy," Nat Methods **9**(7), 755–763 (2012).
54. "Rayleigh length," Wikipedia (2022).
55. F. Mugele and J.-C. Baret, "Electrowetting: from basics to applications," J. Phys.: Condens. Matter **17**(28), R705 (2005).
56. B. Berge and J. Peseux, "Variable focal lens controlled by an external voltage: An application of electrowetting," The European Physical Journal E **3**(2), 159–163 (2000).
57. H.-C. Lin, M.-S. Chen, and Y.-H. Lin, "A Review of Electrically Tunable Focusing Liquid Crystal Lenses," Transactions on Electrical and Electronic Materials **12**(6), 234–240 (2011).
58. "High speed soft tuneable lenses," https://www.epfl.ch/labs/lmts/lmts-research/dea/fastlens/.
59. "Focusing on an Electrowetting Lens," COMSOL (n.d.).
60. H. Ren, D. Fox, P. A. Anderson, B. Wu, and S.-T. Wu, "Tunable-focus liquid lens controlled using a servo motor," Opt. Express, OE **14**(18), 8031–8036 (2006).
61. A. Mermillod-Blondin, E. McLeod, and C. B. Arnold, "High-speed varifocal imaging with a tunable acoustic gradient index of refraction lens," Opt. Lett. **33**(18), 2146 (2008).

62. S. Shian, R. M. Diebold, and D. R. Clarke, "Tunable lenses using transparent dielectric elastomer actuators," Opt. Express, OE **21**(7), 8669–8676 (2013).
63. J. Seagrave, "Understanding the jargon of LCOS Spatial Light Modulators (SLMs)," Laser 2000 (2021).
64. C. Maurer, A. Jesacher, S. Bernet, and M. Ritsch-Marte, "What spatial light modulators can do for optical microscopy," Laser & Photonics Reviews **5**(1), 81–101 (2011).
65. T. A. Bartlett, W. C. McDonald, J. N. Hall, P. I. Oden, D. Doane, R. S. Ketchum, and T. Byrum, "Recent advances in the development of the Texas Instruments phase-only microelectromechanical systems (MEMS) spatial light modulator," in *Emerging Digital Micromirror Device Based Systems and Applications XIII* (SPIE, 2021), **11698**, pp. 103–116.
66. T. Bifano, "MEMS deformable mirrors," Nature Photon **5**(1), 21–23 (2011).
67. "Deformable mirror," Wikipedia (2023).
68. I. Kanno, T. Kunisawa, T. Suzuki, and H. Kotera, "Development of Deformable Mirror Composed of Piezoelectric Thin Films for Adaptive Optics," IEEE Journal of Selected Topics in Quantum Electronics **13**(2), 155–161 (2007).
69. N. Doble and D. R. Williams, "The application of MEMS technology for adaptive optics in vision science," IEEE Journal of Selected Topics in Quantum Electronics **10**(3), 629–635 (2004).
70. W. J. Shain, N. A. Vickers, B. B. Goldberg, T. Bifano, and J. Mertz, "Extended depth-of-field microscopy with a high-speed deformable mirror," Opt. Lett., OL **42**(5), 995–998 (2017).
71. O. Albert, L. Sherman, G. Mourou, T. B. Norris, and G. Vdovin, "Smart microscope: an adaptive optics learning system for aberration correction in multiphoton confocal microscopy," Opt. Lett., OL **25**(1), 52–54 (2000).
72. V. Samarkin and A. Kudryashov, "Deformable mirrors for laser beam shaping," in *Laser Beam Shaping XI* (SPIE, 2010), **7789**, pp. 94–102.
73. E. J. Botcherby, R. Juškaitis, M. J. Booth, and T. Wilson, "An optical technique for remote focusing in microscopy," Optics Communications **281**(4), 880–887 (2008).
74. E. H. K. Stelzer, "S09-02 Light sheet based fluorescence microscopes (LSFM, SPIM, DSLM) reduce phototoxic effects by several orders of magnitude," Mechanisms of Development **126**, S36 (2009).
75. E. G. Reynaud, J. Peychl, J. Huisken, and P. Tomancak, "Guide to light-sheet microscopy for adventurous biologists," Nat Methods **12**(1), 30–34 (2015).
76. P. J. Keller, A. D. Schmidt, A. Santella, K. Khairy, Z. Bao, J. Wittbrodt, and E. H. K. Stelzer, "Fast high-contrast imaging of animal development with scanned light sheet-based structured illumination microscopy," Nat Methods **7**(8), 637–642 (2010).
77. L. Gao, L. Shao, C. D. Higgins, J. S. Poulton, M. Peifer, M. W. Davidson, X. Wu, B. Goldstein, and E. Betzig, "Noninvasive Imaging beyond the Diffraction Limit of 3D Dynamics in Thickly Fluorescent Specimens," Cell **151**(6), 1370–1385 (2012).
78. P. J. Keller, F. Pampaloni, and E. H. K. Stelzer, "Three-dimensional preparation and imaging reveal intrinsic microtubule properties," Nat Methods **4**(10), 843–846 (2007).
79. P. J. Verveer, J. Swoger, F. Pampaloni, K. Greger, M. Marcello, and E. H. K. Stelzer, "High-resolution three-dimensional imaging of large specimens with light sheet–based microscopy," Nat Methods **4**(4), 311–313 (2007).

80. E. G. Reynaud, U. Krzic, K. Greger, and E. H. K. Stelzer, "Light sheet-based fluorescence microscopy: more dimensions, more photons, and less photodamage," HFSP J **2**(5), 266–275 (2008).
81. E. H. K. Stelzer, F. Strobl, B.-J. Chang, F. Preusser, S. Preibisch, K. McDole, and R. Fiolka, "Light sheet fluorescence microscopy," Nat Rev Methods Primers **1**(1), 1–25 (2021).
82. P. J. Keller, F. Pampaloni, and E. H. Stelzer, "Life sciences require the third dimension," Current Opinion in Cell Biology **18**(1), 117–124 (2006).
83. R. M. Power and J. Huisken, "A guide to light-sheet fluorescence microscopy for multiscale imaging," Nat Methods **14**(4), 360–373 (2017).
84. F. O. Fahrbach, V. Gurchenkov, K. Alessandri, P. Nassoy, and A. Rohrbach, "Self-reconstructing sectioned Bessel beams offer submicron optical sectioning for large fields of view in light-sheet microscopy," Opt. Express, OE **21**(9), 11425–11440 (2013).
85. F. O. Fahrbach and A. Rohrbach, "A line scanned light-sheet microscope with phase shaped self-reconstructing beams," Opt. Express **18**(23), 24229 (2010).
86. K. M. Dean and R. Fiolka, "Uniform and scalable light-sheets generated by extended focusing," Opt. Express, OE **22**(21), 26141–26152 (2014).
87. L. Gao, L. Shao, B.-C. Chen, and E. Betzig, "3D live fluorescence imaging of cellular dynamics using Bessel beam plane illumination microscopy," Nat Protoc **9**(5), 1083–1101 (2014).
88. T. Vettenburg, H. I. C. Dalgarno, J. Nylk, C. Coll-Lladó, D. E. K. Ferrier, T. Čižmár, F. J. Gunn-Moore, and K. Dholakia, "Light-sheet microscopy using an Airy beam," Nat Methods **11**(5), 541–544 (2014).
89. B.-J. Chang, M. Kittisopikul, K. M. Dean, P. Roudot, E. S. Welf, and R. Fiolka, "Universal light-sheet generation with field synthesis," Nat Methods **16**(3), 235–238 (2019).
90. B.-J. Chang, K. M. Dean, and R. Fiolka, "Systematic and quantitative comparison of lattice and Gaussian light-sheets," Opt. Express, OE **28**(18), 27052–27077 (2020).
91. Y. Wu, P. Wawrzusin, J. Senseney, R. S. Fischer, R. Christensen, A. Santella, A. G. York, P. W. Winter, C. M. Waterman, Z. Bao, D. A. Colón-Ramos, M. McAuliffe, and H. Shroff, "Spatially isotropic four-dimensional imaging with dual-view plane illumination microscopy," Nat Biotechnol **31**(11), 1032–1038 (2013).
92. J. Swoger, P. Verveer, K. Greger, J. Huisken, and E. H. K. Stelzer, "Multi-view image fusion improves resolution in three-dimensional microscopy," Opt. Express, OE **15**(13), 8029–8042 (2007).
93. B. Schmid, G. Shah, N. Scherf, M. Weber, K. Thierbach, C. P. Campos, I. Roeder, P. Aanstad, and J. Huisken, "High-speed panoramic light-sheet microscopy reveals global endodermal cell dynamics," Nat Commun **4**(1), 2207 (2013).
94. R. K. Chhetri, F. Amat, Y. Wan, B. Höckendorf, W. C. Lemon, and P. J. Keller, "Whole-animal functional and developmental imaging with isotropic spatial resolution," Nat Methods **12**(12), 1171–1178 (2015).
95. S. Preibisch, F. Amat, E. Stamataki, M. Sarov, R. H. Singer, E. Myers, and P. Tomancak, "Efficient Bayesian-based multiview deconvolution," Nat Methods **11**(6), 645–648 (2014).
96. P. J. Keller, A. D. Schmidt, J. Wittbrodt, and E. H. K. Stelzer, "Reconstruction of Zebrafish Early Embryonic Development by Scanned Light Sheet Microscopy," Science **322**(5904), 1065–1069 (2008).

97. T. A. Planchon, L. Gao, D. E. Milkie, M. W. Davidson, J. A. Galbraith, C. G. Galbraith, and E. Betzig, "Rapid three-dimensional isotropic imaging of living cells using Bessel beam plane illumination," Nat Methods **8**(5), 417–423 (2011).
98. L. Gao, "Extend the field of view of selective plan illumination microscopy by tiling the excitation light sheet," Opt. Express, OE **23**(5), 6102–6111 (2015).
99. Q. Fu, B. L. Martin, D. Q. Matus, and L. Gao, "Imaging multicellular specimens with real-time optimized tiling light-sheet selective plane illumination microscopy," Nat Commun **7**(1), 11088 (2016).
100. D. Wang, Y. Jin, R. Feng, Y. Chen, and L. Gao, "Tiling light sheet selective plane illumination microscopy using discontinuous light sheets," Opt. Express, OE **27**(23), 34472–34483 (2019).
101. K. M. Dean, P. Roudot, E. S. Welf, G. Danuser, and R. Fiolka, "Deconvolution-free Subcellular Imaging with Axially Swept Light Sheet Microscopy," Biophysical Journal **108**(12), 2807–2815 (2015).
102. T. Chakraborty, M. K. Driscoll, E. Jeffery, M. M. Murphy, P. Roudot, B.-J. Chang, S. Vora, W. M. Wong, C. D. Nielson, H. Zhang, V. Zhemkov, C. Hiremath, E. D. De La Cruz, Y. Yi, I. Bezprozvanny, H. Zhao, R. Tomer, R. Heintzmann, J. P. Meeks, D. K. Marciano, S. J. Morrison, G. Danuser, K. M. Dean, and R. Fiolka, "Light-sheet microscopy of cleared tissues with isotropic, subcellular resolution," Nat Methods **16**(11), 1109–1113 (2019).
103. F. F. Voigt, D. Kirschenbaum, E. Platonova, S. Pagès, R. A. A. Campbell, R. Kastli, M. Schaettin, L. Egolf, A. van der Bourg, P. Bethge, K. Haenraets, N. Frézel, T. Topilko, P. Perin, D. Hillier, S. Hildebrand, A. Schueth, A. Roebroeck, B. Roska, E. T. Stoeckli, R. Pizzala, N. Renier, H. U. Zeilhofer, T. Karayannis, U. Ziegler, L. Batti, A. Holtmaat, C. Lüscher, A. Aguzzi, and F. Helmchen, "The mesoSPIM initiative: open-source light-sheet microscopes for imaging cleared tissue," Nat Methods **16**(11), 1105–1108 (2019).
104. T. Chakraborty, B. Chen, S. Daetwyler, B.-J. Chang, O. Vanderpoorten, E. Sapoznik, C. F. Kaminski, T. P. J. Knowles, K. M. Dean, and R. Fiolka, "Converting lateral scanning into axial focusing to speed up three-dimensional microscopy," Light Sci Appl **9**(1), 165 (2020).
105. E. J. Botcherby, R. Juskaitis, M. J. Booth, and T. Wilson, "Aberration-free optical refocusing in high numerical aperture microscopy," Opt. Lett. **32**(14), 2007 (2007).
106. Z. Yang, L. Mei, F. Xia, Q. Luo, L. Fu, and H. Gong, "Dual-slit confocal light sheet microscopy for in vivo whole-brain imaging of zebrafish," Biomed. Opt. Express, BOE **6**(5), 1797–1811 (2015).
107. V. Gavryusev, G. Sancataldo, P. Ricci, A. Montalbano, C. Fornetto, L. Turrini, A. Laurino, L. Pesce, G. de Vito, N. Tiso, F. Vanzi, L. Silvestri, and F. S. Pavone, "Dual-beam confocal light-sheet microscopy via flexible acousto-optic deflector," JBO **24**(10), 106504 (2019).
108. D. Jing, S. Zhang, W. Luo, X. Gao, Y. Men, C. Ma, X. Liu, Y. Yi, A. Bugde, B. O. Zhou, Z. Zhao, Q. Yuan, J. Q. Feng, L. Gao, W.-P. Ge, and H. Zhao, "Tissue clearing of both hard and soft tissue organs with the PEGASOS method," Cell Research **28**(8), 803–818 (2018).
109. "Programmable Scan Mode - Learn," https://www.photometrics.com/learn/exclusive-product-features/programmable-scan-mode.
110. "Gaussian beam," Wikipedia (2023).

111. K. M. Dean, P. Roudot, E. S. Welf, T. Pohlkamp, G. Garrelts, J. Herz, and R. Fiolka, "Imaging subcellular dynamics with fast and light-efficient volumetrically parallelized microscopy," Optica, OPTICA **4**(2), 263–271 (2017).
112. M. Bruzzone, E. Chiarello, M. Albanesi, M. E. Miletto Petrazzini, A. Megighian, C. Lodovichi, and M. dal Maschio, "Whole brain functional recordings at cellular resolution in zebrafish larvae with 3D scanning multiphoton microscopy," Sci Rep **11**(1), 11048 (2021).
113. V. Voleti, K. B. Patel, W. Li, C. Perez Campos, S. Bharadwaj, H. Yu, C. Ford, M. J. Casper, R. W. Yan, W. Liang, C. Wen, K. D. Kimura, K. L. Targoff, and E. M. C. Hillman, "Real-time volumetric microscopy of in vivo dynamics and large-scale samples with SCAPE 2.0," Nat Methods **16**(10), 1054–1062 (2019).
114. N. Wagner, N. Norlin, J. Gierten, G. de Medeiros, B. Balázs, J. Wittbrodt, L. Hufnagel, and R. Prevedel, "Instantaneous isotropic volumetric imaging of fast biological processes," Nat Methods **16**(6), 497–500 (2019).
115. "A Protocol For Real-Time 3d Single Particle Tracking - Video," https://www.jove.com/t/56711/a-protocol-for-real-time-3d-single-particle-tracking.
116. T. Panier, S. A. Romano, R. Olive, T. Pietri, G. Sumbre, R. Candelier, and G. Debrégeas, "Fast functional imaging of multiple brain regions in intact zebrafish larvae using selective plane illumination microscopy," Front Neural Circuits **7**, 65 (2013).
117. "Precision Microscope Stages, Auto-Focus Motors, Bio-Imaging | PI," https://www.pi-usa.us/en/products/microscope-stages-bio-imaging-life-sciences.
118. A. T. Wassie, Y. Zhao, and E. S. Boyden, "Expansion microscopy: principles and uses in biological research," Nat Methods **16**(1), 33–41 (2019).
119. S. Kang, M. Duocastella, and C. B. Arnold, "Variable optical elements for fast focus control," Nat. Photonics **14**(9), 533–542 (2020).
120. M. Žurauskas, O. Barnstedt, M. Frade-Rodriguez, S. Waddell, and M. J. Booth, "Rapid adaptive remote focusing microscope for sensing of volumetric neural activity," Biomed. Opt. Express **8**(10), 4369 (2017).
121. M. Bawart, M. A. May, T. Öttl, C. Roider, S. Bernet, M. Schmidt, M. Ritsch-Marte, and A. Jesacher, "Diffractive tunable lens for remote focusing in high-NA optical systems," Opt. Express, OE **28**(18), 26336–26347 (2020).
122. A. Kaplan, N. Friedman, and N. Davidson, "Acousto-optic lens with very fast focus scanning," Opt. Lett., OL **26**(14), 1078–1080 (2001).
123. G. Konstantinou, P. A. Kirkby, G. J. Evans, K. M. N. S. Nadella, V. A. Griffiths, J. E. Mitchell, and R. A. Silver, "Dynamic wavefront shaping with an acousto-optic lens for laser scanning microscopy," Opt. Express, OE **24**(6), 6283–6299 (2016).
124. P. S. Salter, Z. Iqbal, and M. J. Booth, "Analysis of the Three-Dimensional Focal Positioning Capability of Adaptive Optic Elements," International Journal of Optomechatronics **7**(1), 1–14 (2013).
125. H. Dibaji, M. N. H. Prince, Y. Yi, H. Zhao, and T. Chakraborty, "Axial scanning of dual focus to improve light sheet microscopy," Biomed. Opt. Express, BOE **13**(9), 4990–5003 (2022).
126. M. N. H. Prince, B. Garcia, C. Henn, Y. Yi, E. A. Susaki, Y. Watakabe, T. Nemoto, K. A. Lidke, H. Zhao, I. S. Remiro, S. Liu, and T. Chakraborty, "Signal Improved ultra-Fast Light-sheet Microscope (SIFT) for large tissue imaging," 2023.05.31.543002 (2023).

127. S. Mohanan and A. D. Corbett, "Understanding the limits of remote focusing," Opt. Express, OE **31**(10), 16281–16294 (2023).
128. "Sensitivity of remote focusing microscopes to magnification mismatch - Mohanan - 2022 - Journal of Microscopy - Wiley Online Library," https://onlinelibrary.wiley.com/doi/10.1111/jmi.12991.
129. "Aberration-free three-dimensional multiphoton imaging of neuronal activity at kHz rates," https://www.pnas.org/doi/10.1073/pnas.1111662109.
130. H. Sparks, L. Dvinskikh, J. M. Firth, A. J. Francis, S. E. Harding, C. Paterson, K. T. MacLeod, and C. Dunsby, "Development a flexible light-sheet fluorescence microscope for high-speed 3D imaging of calcium dynamics and 3D imaging of cellular microstructure," Journal of Biophotonics **13**(6), e201960239 (2020).
131. J. Kim, "Recent advances in oblique plane microscopy," Nanophotonics **12**(13), 2317–2334 (2023).
132. "Remote-refocusing light-sheet fluorescence microscopy enables 3D imaging of electromechanical coupling of hiPSC-derived and adult cardiomyocytes in co-culture | Scientific Reports," https://www.nature.com/articles/s41598-023-29419-w.
133. "Encyclopedia of Physical Science and Technology," http://www.sciencedirect.com:5070/referencework/9780122274107/encyclopedia-of-physical-science-and-technology.
134. J. E. Heebner, R. S. Bennink, R. W. Boyd, and R. A. Fisher, "Conversion of unpolarized light to polarized light with greater than 50% efficiency by photorefractive two-beam coupling," Opt. Lett., OL **25**(4), 257–259 (2000).
135. J. Fatome, S. Pitois, P. Morin, E. Assémat, D. Sugny, A. Picozzi, H. R. Jauslin, G. Millot, V. V. Kozlov, and S. Wabnitz, "A universal optical all-fiber omnipolarizer," Sci Rep **2**(1), 938 (2012).
136. M. J. Wester, D. J. Schodt, H. Mazloom-Farsibaf, M. Fazel, S. Pallikkuth, and K. A. Lidke, "Robust, fiducial-free drift correction for super-resolution imaging," Sci Rep **11**(1), 23672 (2021).
137. "matlab-instrument-control," (2023).
138. A. J. Smith, J. R. Pfeiffer, J. Zhang, A. M. Martinez, G. M. Griffiths, and B. S. Wilson, "Microtubule-Dependent Transport of Secretory Vesicles in RBL-2H3 Cells," Traffic **4**(5), 302–312 (2003).
139. R. P. Siraganian, R. O. de Castro, E. A. Barbu, and J. Zhang, "Mast cell signaling: The role of protein tyrosine kinase Syk, its activation and screening methods for new pathway participants," FEBS Letters **584**(24), 4933–4940 (2010).
140. N. L. Andrews, J. R. Pfeiffer, A. M. Martinez, D. M. Haaland, R. W. Davis, T. Kawakami, J. M. Oliver, B. S. Wilson, and D. S. Lidke, "Small, Mobile FcεRI Receptor Aggregates Are Signaling Competent," Immunity **31**(3), 469–479 (2009).
141. "Mechanisms of Granule Membrane Recapture following Exocytosis in Intact Mast Cells - ScienceDirect," https://www.sciencedirect.com/science/article/pii/S0021925820456005?via%3Dihub.
142. P. Roudot, W. R. Legant, Q. Zou, K. M. Dean, T. Isogai, E. S. Welf, A. F. David, D. W. Gerlich, R. Fiolka, E. Betzig, and G. Danuser, "u-track 3D: measuring and interrogating dense particle dynamics in three dimensions," 2020.11.30.404814 (2022).

143. A. Dupont, M. Gorelashvili, V. Schüller, F. Wehnekamp, D. Arcizet, Y. Katayama, D. C. Lamb, and D. Heinrich, "Three-dimensional single-particle tracking in live cells: news from the third dimension," New J. Phys. **15**(7), 075008 (2013).
144. X. Michalet, "Mean square displacement analysis of single-particle trajectories with localization error: Brownian motion in an isotropic medium," Phys. Rev. E **82**(4), 041914 (2010).
145. P. Rupprecht, A. Prendergast, C. Wyart, and R. W. Friedrich, "Remote z-scanning with a macroscopic voice coil motor for fast 3D multiphoton laser scanning microscopy," Biomed. Opt. Express, BOE **7**(5), 1656–1671 (2016).
146. M. B. Bouchard, V. Voleti, C. S. Mendes, C. Lacefield, W. B. Grueber, R. S. Mann, R. M. Bruno, and E. M. C. Hillman, "Swept confocally-aligned planar excitation (SCAPE) microscopy for high-speed volumetric imaging of behaving organisms," Nature Photon **9**(2), 113–119 (2015).
147. B. Yang, M. Lange, A. Millett-Sikking, X. Zhao, J. Bragantini, S. VijayKumar, M. Kamb, R. Gómez-Sjöberg, A. C. Solak, W. Wang, H. Kobayashi, M. N. McCarroll, L. W. Whitehead, R. P. Fiolka, T. B. Kornberg, A. G. York, and L. A. Royer, "DaXi—high-resolution, large imaging volume and multi-view single-objective light-sheet microscopy," Nat Methods **19**(4), 461–469 (2022).
148. E. Sapoznik, B.-J. Chang, J. Huh, R. J. Ju, E. V. Azarova, T. Pohlkamp, E. S. Welf, D. Broadbent, A. F. Carisey, S. J. Stehbens, K.-M. Lee, A. Marín, A. B. Hanker, J. C. Schmidt, C. L. Arteaga, B. Yang, Y. Kobayashi, P. R. Tata, R. Kruithoff, K. Doubrovinski, D. P. Shepherd, A. Millett-Sikking, A. G. York, K. M. Dean, and R. P. Fiolka, "A versatile oblique plane microscope for large-scale and high-resolution imaging of subcellular dynamics," eLife **9**, e57681 (2020).
149. B. Chen, B.-J. Chang, P. Roudot, F. Zhou, E. Sapoznik, M. Marlar-Pavey, J. B. Hayes, P. T. Brown, C.-W. Zeng, T. Lambert, J. R. Friedman, C.-L. Zhang, D. T. Burnette, D. P. Shepherd, K. M. Dean, and R. P. Fiolka, "Resolution doubling in light-sheet microscopy via oblique plane structured illumination," Nat Methods **19**(11), 1419–1426 (2022).
150. H. Sparks, L. Dent, C. Bakal, A. Behrens, G. Salbreux, and C. Dunsby, "Dual-view oblique plane microscopy (dOPM)," Biomed. Opt. Express, BOE **11**(12), 7204–7220 (2020).
151. R. C. Jones, "A New Calculus for the Treatment of Optical SystemsI. Description and Discussion of the Calculus," J. Opt. Soc. Am., JOSA **31**(7), 488–493 (1941).
152. "Generalized formulation and symmetry properties of reciprocal nonabsorbing polarization devices: application to liquid-crystal displays," https://opg.optica.org/josaa/fulltext.cfm?uri=josaa-17-11-2074&id=61922.
153. F. Gori, M. Santarsiero, S. Vicalvi, R. Borghi, and G. Guattari, "Beam coherence-polarization matrix," Pure Appl. Opt. **7**(5), 941 (1998).
154. F. T. Liu, J. W. Bohn, E. L. Ferry, H. Yamamoto, C. A. Molinaro, L. A. Sherman, N. R. Klinman, and D. H. Katz, "Monoclonal dinitrophenyl-specific murine IgE antibody: preparation, isolation, and characterization.," The Journal of Immunology **124**(6), 2728–2737 (1980).